Master's thesis

2019

Yi Zhang

Master's thesis

NTNU
Norwegian University of
Science and Technology
Faculty of Engineering
Department of Geoscience and Petroleum

NTNU
Norwegian University of
Science and Technology

Yi Zhang

Seismic signatures of fluid substitution in fractured media

August 2019

NTNU
Norwegian University of
Science and Technology

NTNU
Norwegian University of
Science and Technology

Seismic signatures of fluid substitution in fractured media

Yi Zhang

Erasmus+ exchange
Submission date: August 2019
Supervisor: Alexey Stovas
Co-supervisor: Florian Wellmann

Norwegian University of Science and Technology
Department of Geoscience and Petroleum

Abstract

Seismic response to the fluid substitution of oil with water and CO_2 in a reservoir is analysed. A model consisting of horizontal layers based on the upscaling of well log data is studied. An interval of the model is selected as the reservoir background and then it is horizontally cracked. The model of alternating solid and fluid layers is employed. And the method of propagator matrix is applied to derive the slowness surfaces.

It has been found that there are 3 propagating modes in the horizontally cracked reservoir with fluid saturation, namely fast-P-, slow-P- and S-wave. Under seismic frequency (0-100 Hz), only fast-P-wave is weakly dispersive. The travel time analysis suggests that the overall P/fast-P-wave travel time is more sensitive to fluid substitution compared to that of S/slow-P-wave. And it is possible to identify fluid substitution from oil to CO_2 through P/fast-P travel time when the fracture relative thickness $\phi = 0.001$. Changing the period of the alternating layers H from 1 m to 5 m has no significant impact on the travel time. And it is almost impossible to detect fluid substitution through the travel time with such a low $\phi = 0.0001$. Gradual replacement from oil to water results in an apparent 'linear change' to the P/fast-P travel time as a function of oil saturation.

To obtain P-fast-P-wave reflectivity from overburden to the reservoir, the reservoir is regarded as an effective VTI layer. For $\phi = 0.001$, the reflectivity varies much from oil to CO_2 saturation and the reflectivity change from oil to water is noticeable. H has only a tiny impact on the reflectivity. For lower $\phi = 0.0001$ only the substitution from oil to CO_2 is visible on $R_0 - R_2$ cross plot. The mixed-phase saturation for oil replaced by CO_2 behaves like a linear effect to $R_0 - R_2$ as a function of oil saturation.

The seismic modelling of the acoustic wave equation by frequency-domain finite-difference method for the model with $\phi = 0.0001$ yields the synthetic seismograms. And the result is consistent with the phenomenon mentioned above. The simulation for $\phi = 0.001$ is suffered from high noise, thus, not displayed.

For comparison to the theory for porous media, Biot-Squirt poroelastic mechanism is also applied to the model background to make the reservoir background porous. The reservoir background with porosity ϕ = 0.001 is studied as an example. The result indicates that there is only a moderate reflectivity variation for the fluid substitution from oil to water/CO_2. The travel time is almost the same with oil, water and CO_2 saturation.

Keywords: Fluid substitution, cracked reservoir, propagator matrix, travel time, reflectivity, seismic modelling, acoustic wave equation

Preface

This thesis mainly involves elastoacoustic wave propagation in alternating solid and fluid layers. It was written during the author's Erasmus exchange at NTNU. The author would like to thank Prof. Alexey Stovas at NTNU and Prof. Florian Wellmann at the home university RWTH Aachen for their support to this thesis.

Contents

List of figures

List of tables

1. Introduction

The fluid substitution from oil to water or CO_2 always happens in reservoir stimulation. The analysis of fluid substitution is an important part to assess the reservoir stimulation in cracked or porous reservoirs. And this is always related to 4D or time-lapse seismics. However, the wave propagation in a fractured or porous media is much more complicated than rocks without any voids.

As proposed by Schoenberg and Sayers (1995), 'the effective compliance tensor of the fractured rock (can be written) as the sum of the compliance tensor of the unfractured background rock and the compliance tensors for each set of parallel fractures or aligned fractures'. And there are a lot of studies about fluid substitution based on compliance matrix (Schoenberg & Douma, 1988; Schoenberg & Muirt, 1989). For instance, Zhou, Wang, and Feng (2014) simulated elastic wave propagation in TTI media (VTI media containing tilt fractures) based on Hudson theory, Bond transform and Backus-weighted-average. However, this method is restricted to dry fractures. To extend this, Gassmann's equation (Gassmann, 1951) is a way to saturate the dry media. Sil, Sen, and Gurevich (2011) analysed porous and horizontal transversely isotropic (HTI) media based on Gassmann's anisotropic fluid substitution equation. In this kind of operation, one background media is firstly inserted vertically aligned fractures with compliance matrix, which is still dry fracture system. And then Gassmann's theory is used to convert dry fractured stiffness to fluid-saturated stiffness. This method is easy to implement, however, it fails to explain the high seismic dispersion under high frequency in such a media.

Dvorkin and Nur (1993) proposed Biot-squirt flow mechanism to simulate the poroelasticity in a porous media. The VTI poroelastic wave equation with BISQ theory was originally proposed by Parra (1997). And he combined Biot and squirt mechanisms to describe 2D VTI porous media. This theory considers the fluid flow parallel and perpendicular to P-wave propagation and it succeeds to reveal the high attenuation and dispersion in porous media. It contains 3 wave modes: fast-P-, slow-P- and S-wave. D. Yang and Zhang (2002) then extended the Biot-Squirt poroelastic wave equation to include 2D PTL (periodic thin layers) and EDA (extensive dilatancy anisotropy), which is a porous media containing vertical aligned fractures.

Another genre of the study on fractured media is the linear slip theory applied to alternating solid and fluid layers (Schoenberg, 1984), which is called an elastoacoustic media. This theory assumes the horizontal displacement does not need to be continuous for the interface between solid and fluid and the shear stress vanishes in fluid. And he uses the method of propagator matrix (Gilbert & Backus, 1966) to investigate the wave propagation in alternating solid and fluid layers. There are 2 modes in his study, one fast-P-mode and one slow-P-mode under long-wavelength approximation.

In this article, the author mainly uses the model of alternating solid and fluid layers to perform some simulations to see how fluid substitution affects the travel time and reflectivity based on a case study with well log data. This includes both analytical method and seismic modelling based on frequency-domain finite difference method, which is inspired by Masson, Pride, and Nihei (2006), Hongjuan and Guangming (2012), Jamali Hondori, Mikada, Goto, and Takekawa (2013) and Souza et al. (2013).

We start in Chapter 2 by introducing vertical transverse isotropy (VTI) and its related properties. Chapter 3 gives the derivation from the basic laws (equation of motion and generalized Hooke's law) to propagator matrix and then the phase velocity can be calculated from the propagator matrix. Slightly different from the original work by Schoenberg (1984), the author finds 3 modes, fast-P, slow-P and S, which corresponds to Biot theory. And this is identical to the work by Stovas and Roganov (2017). But they use different notations on the 3 waves, P-wave, fast-S-wave and slow-S-wave.

In Chapter 4, a set of well log data is provided. It is firstly divided into 4 Blocks and Backus averaging is applied to obtain the effective parameters of each block. Then Block 3 is set isotropic and selected as the background as our reservoir. Based on the reservoir background, the following sections illustrate the model structure and different input parameters to the reservoir to be used later.

Chapter 5 analyzes the travel time behaviour for different models for both single reservoir and the reservoir with overburden included based on the slowness formula from Chapter 3, including the single phase saturated and mixed phase saturated reservoir. Chapter 6 uses VTI slowness equation to approximate Thomsen parameter δ , with which the reflectivity between the reservoir and the overburden can be computed. The reflectivity under different saturations is studied.

The finite-difference method is used in Chapter 7 to simulate the wave propagation in our models, where the acoustic VTI wave equation and the acoustic wave equation for alternating solid and fluid layers are combined.

In order to compare the difference of linear slip theory and BISQ theory, the author performed both analytical and numerical simulation for an example model with BISQ theory in Chapter 8.

2. Anisotropy

This chapter gives some fundamentals of VTI media, including the definition, stiffness and Thomsen parameters.

2.1. VTI media

The non-reservoir layers in this study will be regarded as VTI media. So, it is necessary to illustrate the properties of VTI media.

Isotropic homogenous media means elastic velocities are the same along with all possible directions. However, it is not always the case for subsurface rocks as their vertical stress is much larger than the horizontal ones. As a result, the rock materials in the vertical direction z is usually more compacted, i.e., the rock is harder in the vertical direction compared to the horizontal direction. Thus, P-wave travels faster vertically and slower horizontally. This is how the seismic anisotropy comes to rocks.

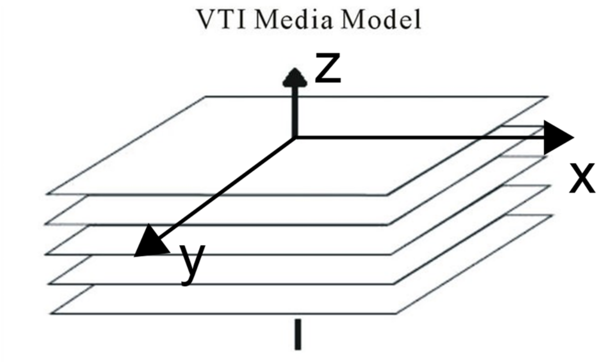

Figure 2-1. A sketch of VTI media (Oh & Brunskog, 2014).

Let us assume that one 3D material has property along with 3 orthogonal directions (x, y, z) with z being the vertical direction. For a VTI media (Figure 2-1), all the elastic properties in the x-y plane do not vary with the azimuth angle while they change with z.

Now consider the stress-strain relations for a cube in Figure 2-2 (Later, the direction 1 is equivalent to x, 2 to y and 3 to z).

According to generalized Hook's law in Voigt notation, stress can be expressed as a function of a linear combination of strains:

$$\boldsymbol{\sigma} = \mathbf{C}\boldsymbol{\varepsilon} \tag{2.1}$$

$$\mathbf{C} = \begin{pmatrix} C_{11} & C_{12} & C_{13} & C_{14} & C_{15} & C_{16} \\ C_{21} & C_{22} & C_{23} & C_{24} & C_{25} & C_{26} \\ C_{31} & C_{32} & C_{33} & C_{34} & C_{35} & C_{36} \\ C_{41} & C_{42} & C_{43} & C_{44} & C_{45} & C_{46} \\ C_{51} & C_{52} & C_{53} & C_{54} & C_{55} & C_{56} \\ C_{61} & C_{62} & C_{63} & C_{64} & C_{65} & C_{66} \end{pmatrix} \tag{2.2}$$

$$\boldsymbol{\varepsilon} = \begin{pmatrix} \varepsilon_{11} & \varepsilon_{22} & \varepsilon_{33} & \varepsilon_{23} & \varepsilon_{13} & \varepsilon_{12} \end{pmatrix}^T \tag{2.3}$$

where $\mathbf{C}$ is namely the stiffness matrix. And $\mathbf{C}$ is a symmetric matrix.

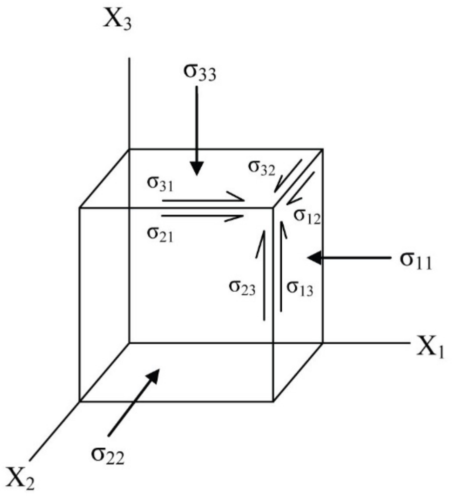

Figure 2-2. Stress on a cube (Burnley, 2019).

For isotropic media (Thomsen, 2002), the stiffness is given by

$$\mathbf{C} = \begin{pmatrix} M & \lambda & \lambda & & & \\ & M & \lambda & & & \\ & & M & & & \\ & & & G & & \\ & & & & G & \\ & & & & & G \end{pmatrix} \tag{2.4}$$

$$\lambda = M - 2G$$

where M is the P-wave modulus and G is the shear wave modulus.

For VTI media, there are 5 independent stiffness parameters,

$$\mathbf{C}=\begin{pmatrix} C_{11} & C_{11}-2C_{66} & C_{13} & & & \\ & C_{11} & C_{13} & & & \\ & & C_{33} & & & \\ & & & C_{44} & & \\ & & & & C_{44} & \\ & & & & & C_{66} \end{pmatrix} \tag{2.5}$$

and it is clear that an isotropic media is a special case of VTI.

2.2. Thomsen parameters

Proposed by Thomsen (1986), the Thomsen parameters now have become the most popular stencil to describe the anisotropy of VTI.

In VTI media, there are 5 independent elastic parameters, which can be described either by (2.5) or 3 Thomsen parameters with v_{p0} and v_{s0}, which is

$$\begin{gathered} v_{p0}=\left(\frac{C_{33}}{\rho}\right)^{\frac{1}{2}} \\ v_{s0}=\left(\frac{C_{44}}{\rho}\right)^{\frac{1}{2}} \\ \epsilon=\frac{C_{11}-C_{33}}{2C_{33}} \\ \delta=\frac{\left(C_{13}-C_{44}\right)^2-\left(C_{33}-C_{44}\right)^2}{2C_{33}\left(C_{33}-C_{44}\right)} \\ \gamma=\frac{C_{66}-C_{44}}{2C_{44}} \end{gathered} \tag{2.6}$$

3. Waves in alternating solid and fluid layers

This chapter depicts a rock physics model of alternating solid and fluid layers and its related elastic properties.

The reservoir in our study is considered as an isotropic background plus horizontally layered fractures filled with fluid and the thickness of each solid and fluid layers is the same (Figure 3-1). This model and its associated elastic theory were proposed by Schoenberg (1984). Inspired by Kennett (2009) and Gilbert and Backus (1966), the author repeated the derivation of the kinematic properties of the elastic wave in this model.

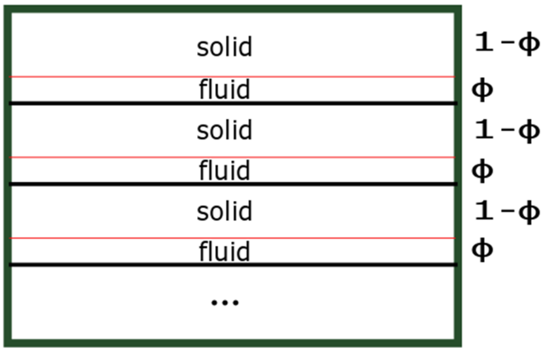

Figure 3-1. A sketch of the reservoir consisting of alternating solid and fluid layers. ϕ is the fracture relative thickness, which is the proportion of the thickness of the fracture relative to the whole thickness.

3.1. Displacement and stress field

In this section, the author derived the displacement and stress field for the alternating isotropic solid and ideal fluid.

Firstly, let us define slowness, the horizontal slowness p and vertical slowness q:

$$p = \frac{sin\theta}{v}$$
$$q = \frac{cos\theta}{v} \tag{3.1}$$

where v is the phase velocity and θ is the phase angle relative to the z-axis.

The symmetric engineering strain $\boldsymbol{\varepsilon}$ can be formulated as a function of displacements:

$$\boldsymbol{\varepsilon}=\begin{pmatrix} \frac{\partial u_x}{\partial x} & \frac{1}{2}\left(\frac{\partial u_x}{\partial y}+\frac{\partial u_y}{\partial x}\right) & \frac{1}{2}\left(\frac{\partial u_x}{\partial z}+\frac{\partial u_z}{\partial x}\right) \\ & \frac{\partial u_y}{\partial y} & \frac{1}{2}\left(\frac{\partial u_y}{\partial z}+\frac{\partial u_z}{\partial y}\right) \\ & & \frac{\partial u_z}{\partial z} \end{pmatrix} \tag{3.2}$$

where $\mathbf{u}$ is the displacement.

The source-free equation of motion is given by

$$\rho\frac{\partial^2 u_i}{\partial t^2}=\frac{\partial \sigma_{ij}}{\partial x_j} \tag{3.3}$$

Combining generalized Hook's law ((2.1), (2.5), (3.2) and (3.3)) gives the system of equations describing the displacement and stress field in a solid VTI material:

$$\begin{aligned} \rho\frac{\partial^2 u_x}{\partial t^2}&=\frac{\partial \sigma_{11}}{\partial x}+\frac{\partial \sigma_{33}}{\partial z} \\ \rho\frac{\partial^2 u_z}{\partial t^2}&=\frac{\partial \sigma_{13}}{\partial x}+\frac{\partial \sigma_{33}}{\partial z} \\ \sigma_{11}&=C_{11}\frac{\partial u_x}{\partial x}+C_{13}\frac{\partial u_z}{\partial z} \\ \sigma_{13}&=C_{44}\left(\frac{\partial u_x}{\partial z}+\frac{\partial u_z}{\partial x}\right) \\ \sigma_{33}&=C_{13}\frac{\partial u_x}{\partial x}+C_{33}\frac{\partial u_z}{\partial z} \end{aligned} \tag{3.4}$$

Now, consider Fourier transform for $\mathbf{u}$ and $\boldsymbol{\sigma}$ in x and z dimension, which is

$$\begin{aligned} \mathbf{u}(x,z,t)&\rightarrow\mathbf{U}(k_x,z,\omega) \\ \boldsymbol{\sigma}(x,z,t)&\rightarrow\boldsymbol{\sigma}(k_x,z,\omega) \end{aligned} \tag{3.5}$$

where k_x is the wavenumber in the x-direction, which equals to ωp; ω is the angular frequency; $\mathbf{U}(k_x,z,t)$ and $\boldsymbol{\sigma}(k_x,z,t)$ is displacement and stress in (k_x,z,t) domain respectively.

Also, the derivative of a function in the time and spatial domain can be transformed as below in the frequency and wavenumber domain, i.e.,

$$\begin{aligned}\frac{\partial}{\partial x} &\to ik_x \\ \frac{\partial}{\partial t} &\to -i\omega\end{aligned} \tag{3.6}$$

Substitute (3.6) into (3.4) and write the system of equations in a matrix form, and then eliminate σ_{11} to obtain

$$\begin{aligned}\frac{\partial}{\partial z}\begin{pmatrix}U_x\\U_z\\\sigma_{13}\\\sigma_{33}\end{pmatrix} &= \begin{pmatrix} 0 & -ik_x & \frac{1}{C_{44}} & 0 \\ -\frac{ik_xC_{13}}{C_{33}} & 0 & 0 & \frac{1}{C_{33}} \\ k_x^2C_{11}-\frac{k_x^2C_{13}^2}{C_{33}}-\rho\omega^2 & 0 & 0 & -\frac{ik_xC_{13}}{C_{33}} \\ 0 & -\rho\omega^2 & -ik_x & 0\end{pmatrix}\begin{pmatrix}U_x\\U_z\\\sigma_{13}\\\sigma_{33}\end{pmatrix} \\ &= \begin{pmatrix} 0 & -ik_x & \frac{1}{\rho v_s^2} & 0 \\ -\frac{ik_x(v_p^2-2v_s^2)}{v_p^2} & 0 & 0 & \frac{1}{\rho v_p^2} \\ \rho k_x^2v_p^2-\frac{k_x^2\rho(v_p^2-2v_s^2)^2}{v_p^2}-\rho\omega^2 & 0 & 0 & -\frac{ik_x(v_p^2-2v_s^2)}{v_p^2} \\ 0 & -\rho\omega^2 & -ik_x & 0\end{pmatrix}\begin{pmatrix}U_x\\U_z\\\sigma_{13}\\\sigma_{33}\end{pmatrix}\end{aligned} \tag{3.7}$$

where C_{ij} is the stiffness of solid. For isotropic media, C_{ij} is degenerated to C_{33} and C_{44}, which can be related to P-wave velocity v_p and v_s of the solid according to (2.6).

(3.7) can be written in the form

$$\frac{\partial}{\partial z}\mathbf{b_s} = \mathbf{A_s b_s} \tag{3.8}$$

(3.7) is not able to handle ideal fluid as C_{44} in fluid vanishes thus $\frac{1}{C_{44}}$ approaches infinity.

Again from (3.4) for the fluid case and eliminate U_x, one can obtain

$$\begin{aligned}&\frac{\partial}{\partial z}\begin{pmatrix}U_z\\ \sigma_{33}\end{pmatrix}\\ &=\begin{pmatrix}0 & \dfrac{k_x^2C_{13f}^2}{C_{33f}\left(k_x^2C_{11f}C_{33f}-k_x^2C_{13f}^2-\rho_f\omega^2C_{33f}\right)}+\dfrac{1}{C_{33f}}\\ -\rho_f\omega^2 & 0\end{pmatrix}\begin{pmatrix}U_z\\ \sigma_{33}\end{pmatrix}\\ &=\begin{pmatrix}0 & -\dfrac{k_x^2}{\rho_f\omega^2}+\dfrac{1}{\rho_f v_{pf}^2}\\ -\rho_f\omega^2 & 0\end{pmatrix}\begin{pmatrix}U_z\\ \sigma_{33}\end{pmatrix}\end{aligned} \tag{3.9}$$

where C_{ijf} is the stiffness of fluid. For fluid, C_{ij} can be reduced to only C_{33}, which is $\rho_f v_{pf}^2$ based on the first equation of (2.6).

(3.9) can be written as

$$\frac{\partial}{\partial z}\mathbf{b_f} = \mathbf{A_f}\mathbf{b_f} \tag{3.10}$$

It is clear that both (3.8) and (3.10) are ordinary differential equations and can be solved with regard to so-called propagator matrix.

3.2. Propagator matrix

According to Kennett (2009), for a homogeneous media, the propagator matrices link the displacement and stress field from one location to another:

$$\begin{aligned}\mathbf{b_s}(z)&=\mathbf{P_s}(z,z_0)\mathbf{b_s}(z_0)\\ \mathbf{P_s}(z,z_0)&=exp\left((z-z_0)\mathbf{A_s}\right)\\ \mathbf{b_f}(z)&=\mathbf{P_f}(z,z_0)\mathbf{b_f}(z_0)\\ \mathbf{P_f}(z,z_0)&=exp\left((z-z_0)\mathbf{A_f}\right)\end{aligned} \tag{3.11}$$

$\mathbf{P_s}$ and $\mathbf{P_f}$ are named propagator matrices, later on, namely $\mathbf{P}$ for both cases, and the corresponding letters without subscript indicate the general case for both solid and fluid. For instance, as long as the wavefield vector $\mathbf{b}$ at one location z_0 is known, then $\mathbf{P}$ can easily give the solution of wavefield at the location z.

The expression of $\mathbf{P}$ is complicated. Here, we consider the decomposition of $\mathbf{A}$ into diagonal matrix $\mathbf{\Lambda}$ of eigenvalues and matrix $\mathbf{D}$ whose columns are the corresponding right eigenvectors so that

$$\mathbf{AD} = \mathbf{D\Lambda} \tag{3.12}$$

And then $\mathbf{P}$ can be related to $\mathbf{\Lambda}$ and $\mathbf{D}$ in such a way

$$\mathbf{P}(z, z_0) = exp((z - z_0)\mathbf{A}) = \mathbf{D}exp((z - z_0)\mathbf{\Lambda})\mathbf{D}^{-1} \tag{3.13}$$

where $\mathbf{\Lambda}$ and $\mathbf{D}$ are given below:

$$\mathbf{\Lambda_s} = \begin{pmatrix} \sigma_1 & 0 & 0 & 0 \\ 0 & \sigma_2 & 0 & 0 \\ 0 & 0 & -\sigma_1 & 0 \\ 0 & 0 & 0 & -\sigma_2 \end{pmatrix}$$

$$\sigma_1 = \frac{\omega\sqrt{(pv_p - 1)(pv_p + 1)}}{v_p}$$

$$\sigma_2 = \frac{\omega\sqrt{(pv_s - 1)(pv_s + 1)}}{v_s}$$

$$\mathbf{D_s} = \left(\begin{matrix} \dfrac{pi}{\omega\rho(2p^2v_s^2 - 1)} & \dfrac{i}{2\omega p\rho v_s^2} \\ \dfrac{\sqrt{(pv_p - 1)(pv_p + 1)}}{\omega\rho v_p(2p^2v_s^2 - 1)} & \dfrac{\sqrt{(pv_s - 1)(pv_s + 1)}}{2\omega\rho v_s(2p^2v_s^2 - 1)} \\ \dfrac{2\omega pv_s^2\sqrt{(pv_p - 1)(pv_p + 1)}}{v_p(\omega i - 2\omega p^2v_s^2 i)} & \dfrac{\omega(2p^2v_s^2 - 1)\sqrt{(pv_s - 1)(pv_s + 1)}}{2v_s(\omega pi - \omega p^3v_s^2 i)} \\ 1 & 1 \end{matrix} \right. \tag{3.14}$$

$$\left. \begin{matrix} \dfrac{pi}{\omega\rho(2p^2v_s^2 - 1)} & \dfrac{i}{2\omega p\rho v_s^2} \\ -\dfrac{\sqrt{(pv_p - 1)(pv_p + 1)}}{\omega\rho v_p(2p^2v_s^2 - 1)} & -\dfrac{\sqrt{(pv_s - 1)(pv_s + 1)}}{2\omega\rho v_s(2p^2v_s^2 - 1)} \\ -\dfrac{2\omega pv_s^2\sqrt{(pv_p - 1)(pv_p + 1)}}{v_p(\omega i - 2\omega p^2v_s^2 i)} & -\dfrac{\omega(2p^2v_s^2 - 1)\sqrt{(pv_s - 1)(pv_s + 1)}}{2v_s(\omega pi - \omega p^3v_s^2 i)} \\ 1 & 1 \end{matrix} \right)$$

and

$$\mathbf{\Lambda_f} = \begin{pmatrix} \frac{\omega\sqrt{\left(p\mathrm{v}_{pf}-1\right)\left(p\mathrm{v}_{pf}+1\right)}}{\mathrm{v}_{pf}} & 0 \\ 0 & -\frac{\omega\sqrt{\left(p\mathrm{v}_{pf}-1\right)\left(p\mathrm{v}_{pf}+1\right)}}{\mathrm{v}_{pf}} \end{pmatrix} \tag{3.15}$$

$$\mathbf{D_f} = \begin{pmatrix} -\frac{\sqrt{\left(p\mathrm{v}_{pf}-1\right)\left(p\mathrm{v}_{pf}+1\right)}}{\omega\rho_f \mathrm{v}_{pf}} & \frac{\sqrt{\left(p\mathrm{v}_{pf}-1\right)\left(p\mathrm{v}_{pf}+1\right)}}{\omega\rho_f \mathrm{f}\,\mathrm{v}_{pf}} \\ 1 & 1 \end{pmatrix}$$

However, it is inhomogenous for the model in Figure 3-1. But it can be noticed that the model consists of 2 homogenous layers. So, by defining the boundary condition, it is possible to use one overall propagator matrix to describe the elastic wave propagation. And this method was proposed by Schoenberg (1984).

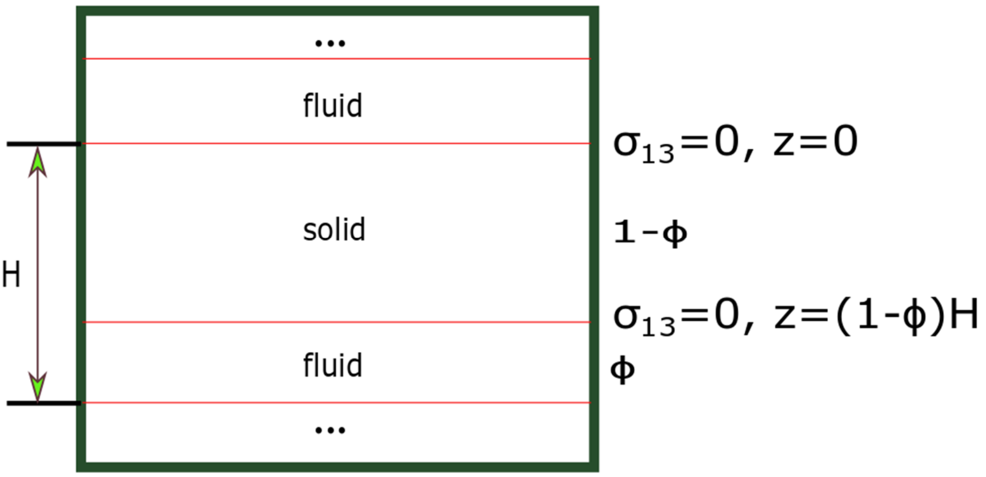

Figure 3-2. Boundary condition of a solid layer. The thickness of one period measures H.

Figure 3-2 sketches a solid layer bounded by 2 fluid layers. As fluid does not possess shear stress, σ_{13} must vanish at the boundaries $z=0$ and $z=\left(1-\phi\right)H$. As a result, in one solid layer,

$$\begin{pmatrix} U_x \\ U_z \\ 0 \\ \sigma_{33} \end{pmatrix}_{z=(1-\phi)H} = \mathbf{P_s}\left(0,\left(1-\phi\right)H\right)\begin{pmatrix} U_x \\ U_z \\ 0 \\ \sigma_{33} \end{pmatrix}_{z=0} \tag{3.16}$$

As U_x does not need to be continuous crossing the boundaries, we can eliminate the first and third equations in (3.16),

$$\begin{aligned}
&\begin{pmatrix} U_z \\ \sigma_{33} \end{pmatrix}_{z=(1-\phi)H} \\
&= \begin{pmatrix} \dfrac{P_{s2,1}P_{s3,2}}{P_{s3,1}} + P_{s2,2} & \dfrac{P_{s2,1}P_{s3,4}}{P_{s3,1}} + P_{s2,4} \\ \dfrac{P_{s4,1}P_{s3,2}}{P_{s3,1}} + P_{s4,2} & \dfrac{P_{s4,1}P_{s3,4}}{P_{s3,1}} + P_{s4,4} \end{pmatrix}_{(0,(1-\phi)H)} \begin{pmatrix} U_z \\ \sigma_{33} \end{pmatrix}_{z=0} \qquad (3.17) \\
&= \mathbf{Q_s} \begin{pmatrix} U_z \\ \sigma_{33} \end{pmatrix}_{z=0}
\end{aligned}$$

where $P_{si,j}$ indicates the element at i-th row and j-th column of $\mathbf{P_s}$.

Now, the propagator crossing one period H from solid to fluid can be expressed by

$$\mathbf{M}(H) = \mathbf{P_f}\left((1-\phi)H, H\right)\mathbf{Q_s} \qquad (3.18)$$

Based on Schoenberg (1984), $cos\left(\omega q\, H\right)$ equals to half of the trace of $\mathbf{M}$, i.e.,

$$\cos(\omega qH) = 0.5trace(\mathbf{M}) \qquad (3.19)$$

For propagation from fluid to solid, $\mathbf{M}$ is different to that from solid to fluid. However, $trace(\mathbf{M})$ remains the same and (3.19) is still valid.

Solve (3.19) for q and the formula for q is given in (11.1) in appendix. Here, $q(p)$ is dependent on v_p, v_s, ρ, v_{pf}, ρ_f, H, ϕ and ω, 8 parameters in total.

Even though the background solid is isotropic, (11.1) is complicated enough to express. When it comes to alternating VTI solid and fluid, then the propagator matrix becomes much more complicated to solve. In order to decrease the computation complexity, the background solid is constrained to isotropic background media.

3.3. Numerical test

(3.19) is checked if it can generate the same result with Stovas and Roganov (2017). And the test input parameters are given in Table 3-1. The result computed by (3.19) is shown in Figure 3-3. It is found that the result is identical to Stovas and Roganov (2017). Therefore, the derivation for the wave propagation in such a model given by Figure 3-1 is robust. There are 3 waves in Figure 3-1, based on the convention of Schoenberg

(1984), we name fast-P-, slow-P- and S-wave in the order of velocities from fast to slow. Please note that they are not exact P- or S-wave but qP- qS-wave as the wave in this media is a phenomenon of interference.

Table 3-1. Physical parameters for the test of (3.19).

v_p	$4000\,m/s$	ρ_f	$1000\ kg/m^3$
v_s	$2200\,m/s$	H	$1\,m$
ρ	$2700\ kg/m^3$	ϕ	0.001
v_{pf}	$1500\,m/s$	ω	$20\pi\ rad/s$

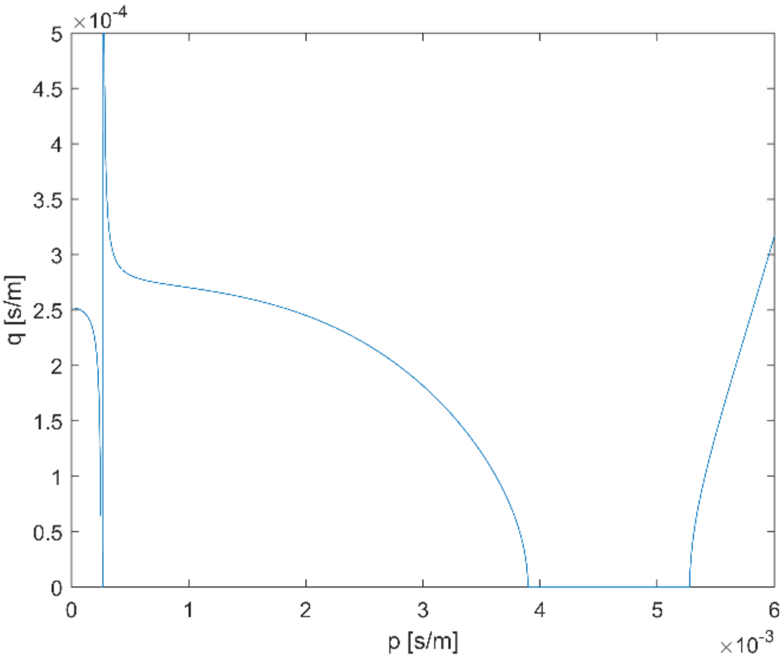

Figure 3-3. Test result for (3.19) with the physical parameters given in Table 3-1.

4. Model construction

This chapter explains the rock physics model to be used later.

4.1. Upscaling of well log data

This section displays the well log data and then applies upscaling to get 4 blocks, in which Block 3 is inferred reservoir background. After that, Block 3 is modified to isotropic in order to adopt (11.1).

The target of upscaling of well log data is to increase the scale which matches the magnitude of seismic wavelength (Kumar, 2013). For instance, the transmitter of sonic logs usually emits sound wave at a frequency of 20 - 40 kHz while seismic exploration usually employs a source with a frequency lower than 100 Hz. As a result, the subsurface details detected by well log are invisible in seismic data. Upscaling is a method to get an equivalent effective media for a selected interval from well log profile.

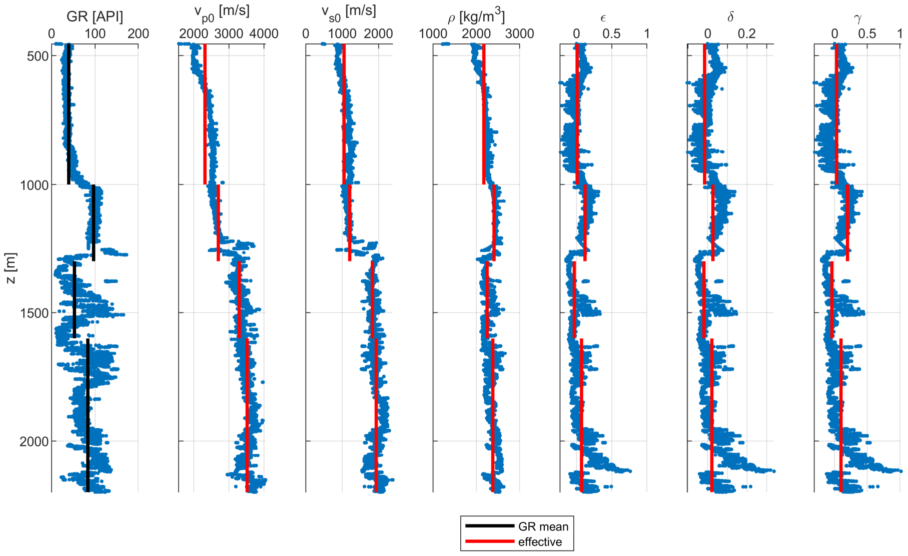

Figure 4-1. Modified well log data after noise removal and blocking. GR: Gamma-ray log. v_{p0}: vertical P-wave velocity. v_{s0}: vertical S-wave velocity. ρ: bulk density. ϵ, δ and γ are Thomsen anisotropy parameters of VTI media.

Due to some measurement errors, there exist some anomalies of the well log data. Therefore, those abnormal data (such as minus velocity or extraordinarily high anisotropy parameters) should be removed. The corrected and blocked well log panel is shown in Figure 4-1. The well log data is firstly divided into 4 blocks. There are 2 potential blocks, Block 1 and Block 3 that can be selected as the background of the reservoir since the GR of them which indicates the clay content is generally relatively smaller than the other blocks. And the author selected Block 3 as the reservoir background as it is buried under overburden sediment, which is always the case to our common knowledge.

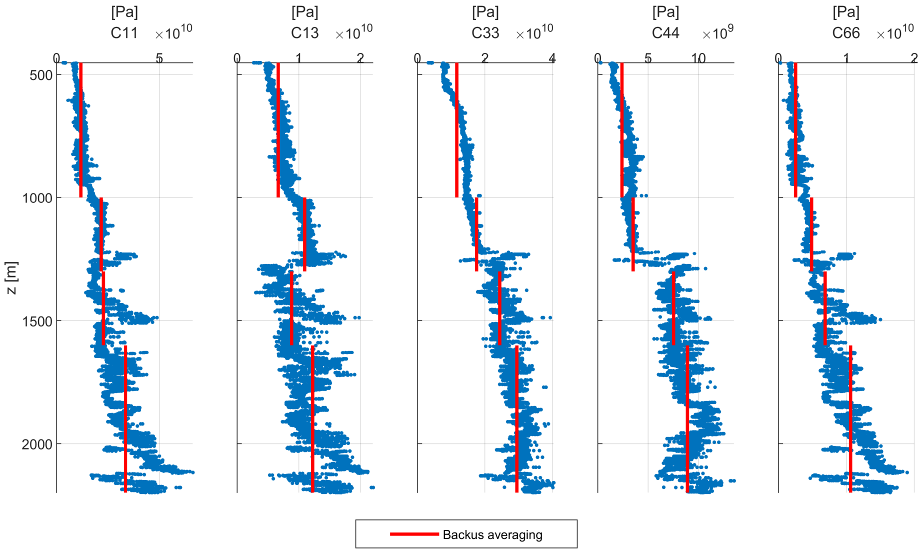

Figure 4-2. Stiffness profile from the modified well log data.

In addition, the stiffness profile can be easily obtained through (2.6) at each depth point. Backus averaging (Backus, 1962; Bos, Dalton, Slawinski, & Stanoev, 2016) is a convenient way to upscale the log data for VTI media:

$$
\begin{aligned}
\overline{C_{33}} &= \left\langle C_{33}^{-1} \right\rangle^{-1} \\
\overline{C_{44}} &= \left\langle C_{44}^{-1} \right\rangle^{-1} \\
\overline{C_{66}} &= \left\langle C_{66} \right\rangle \\
\overline{C_{13}} &= \left\langle \frac{C_{13}}{C_{33}} \right\rangle \left\langle C_{33}^{-1} \right\rangle^{-1} \\
\overline{C_{11}} &= \left\langle C_{11} - \frac{C_{13}^{2}}{C_{33}} \right\rangle + \left\langle \frac{C_{13}}{C_{33}} \right\rangle^{2} \left\langle C_{33}^{-1} \right\rangle^{-1}
\end{aligned}
\tag{4.1}
$$

where $\overline{C_{11}}$, $\overline{C_{33}}$, $\overline{C_{13}}$, $\overline{C_{33}}$, $\overline{C_{44}}$ and $\overline{C_{66}}$ are the effective stiffness parameters for the 4 blocks.

The original and upscaled stiffness are both given in Figure 4-2. Then v_{p0}, v_{s0} and the Thomsen parameters can be converted from effective C with (2.6) and those effective kinematic parameters are labelled with the red lines in Figure 4-1. The detailed information of the 4 blocks is listed in Table 11-1.

In order to employ (11.1) which is dedicated for isotropic background media, the reservoir Block 3 is, therefore, necessary to be modified to isotropic. Here, Block 3 is converted to isotropic media by simply set all Thomsen parameters to ‘0’. Then with v_{p0}, v_{s0} and ρ, the stiffness can be recovered for the isotropic Block 3 as below:

$$\mathbf{C}_3 = \begin{pmatrix} 2.4381 & 0.9316 & 0.9316 & 0 & 0 & 0 \\ & 0 & 2.4381 & 0.9316 & 0 & 0 \\ & & & 0.7532 & 0 & 0 \\ & & & & 0.7532 & 0 \\ & & & & & 0.7532 \end{pmatrix} \tag{4.2}$$

4.2. Model structure

As both alternating solid and fluid layers and VTI media are classified as polar anisotropy, it is enough to study the 2D property of the 3D model since all the phenomenon in the symmetry plane is the same. Thus, a 2D model with horizontal layers (4 blocks mentioned above) is considered. Figure 4-3 gives an overview of the model structure. As a result, the complex geology is out of the scope of this study.

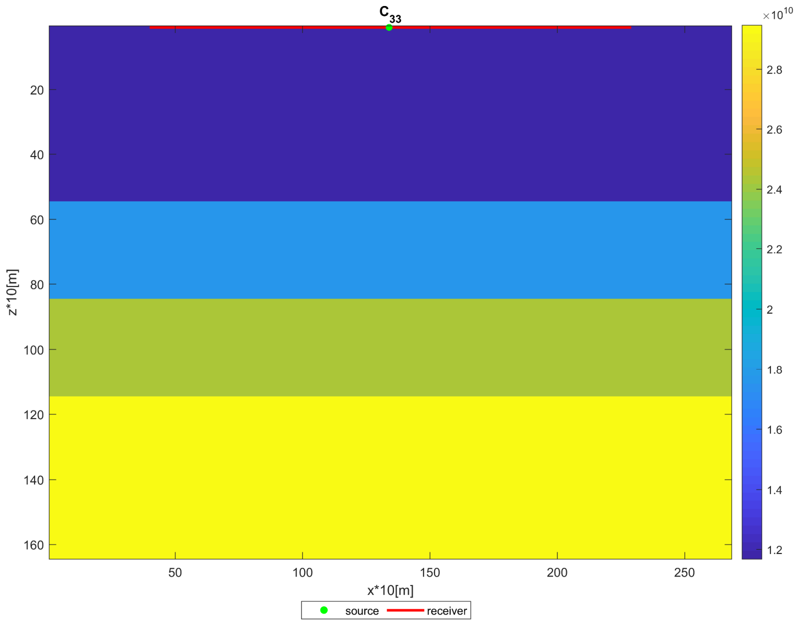

Figure 4-3. Elastic model (4 blocks) obtained from the upscaling of well log data. In this figure, C_{33} is displayed to indicate different blocks.

A source and some receivers are assumed to be placed on the top of Block 1. The later simulations will follow this structure.

4.3. Modification to Block 3

It is essential to point out that all the blocks now are still non-porous and non-cracked. The slowness surface of isotropic Block 3 is given in Figure 4-4. As long as isotropic Block 3 is inserted fractures or pores, it can have some voids to be a true reservoir. That is why Block 3 is previously named the background of the reservoir.

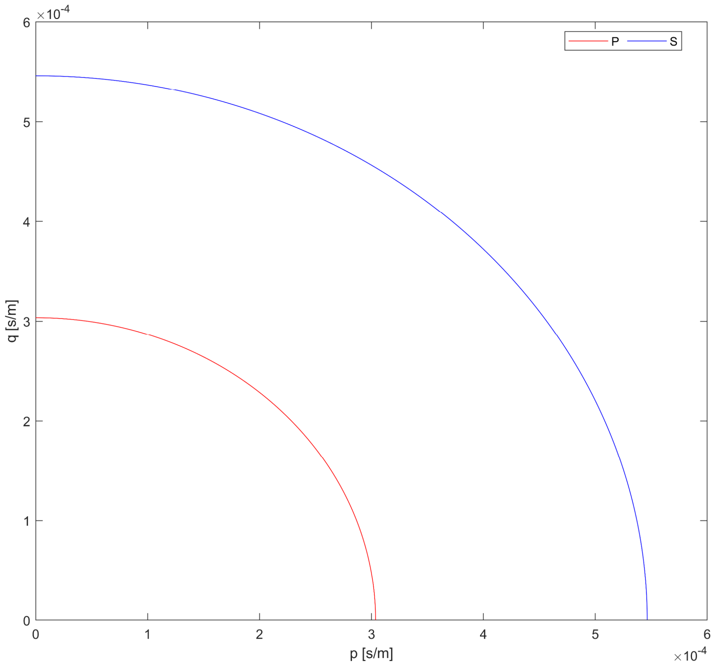

Figure 4-4. Slowness surface of isotropic Block 3. P- and S-wave slowness surfaces are labelled.

The modification of isotropic Block 3 to be a reservoir is covered in later chapters with different methods. For instance, alternating solid and fluid layers theory and BISQ are both methods to make Block 3 have voids in later chapters. As a result, the fluid properties can only affect the elastic behaviours of Block 3. And those specific behaviours from the fluid can propagate to the surface of Block 3 and then to the surface of Block 1 eventually.

As mentioned before, there are 8 independent parameters affecting the model consisting of alternating solid and fluid. In order to test the relationship between fluid substitution and the travel time change, 3 models of Block 3 are developed for tests (Table 4-1). Also, the fluid property is another input for simulation. Thus, here is given the fluid properties for oil, water and gas (Table 4-2).

Table 4-1. The 3 testing models for Block 3.

Model	$H\,[m]$	ϕ
1	1	0.001
2	1	0.0001
3	5	0.001

Table 4-2. Physical parameters of fluids.

Fluid	$v_f\ [m/s]$	$\rho_f\ \left[kg/m^3\right]$
Oil	1200	600
Water	1500	1000
CO_2	400	600

5. Travel time

This chapter utilizes the alternating solid and fluid layers theory as derived in Chapter 3 to compute the travel time. Firstly, the velocity dispersion is studied to check how much the seismic frequency affects the velocities in Block 3. And then the travel time as a function of offset is computed for both surfaces of Block 1 and Block 3. It is forecasted that the effect of fluid substitution on the travel time on the top of Block 1 is much smaller than that on the Block 3's surface. This is because there are 2 overburden layers lessen this influence.

5.1. Dispersion

In this section, the dispersion of vertical fast-P-wave, horizontal fast-P-wave, horizontal slow-P-wave and horizontal S-wave (phase velocity) are analyzed. The 3 models are tested separately.

5.1.1. Model 1

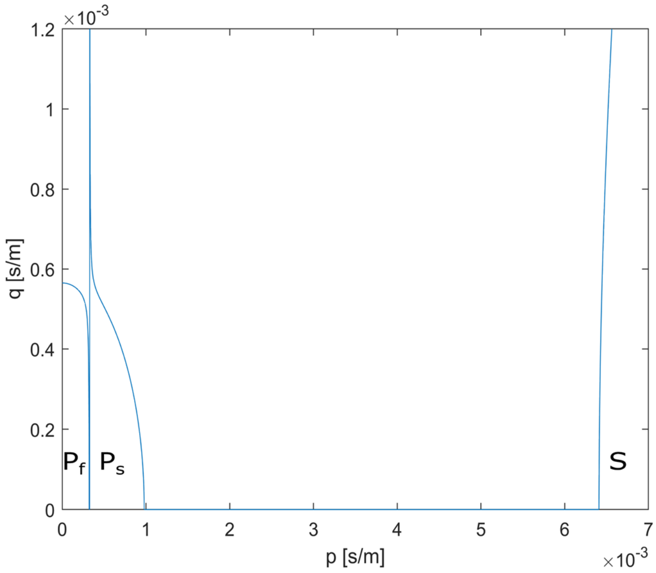

Figure 5-1. Slowness surface of oil-saturated Model 1 (5 Hz). P_f for fast-P-wave and P_s for slow-P-wave.

In this case, the fracture relative thickness ϕ is set 0.001 and the length of one solid/fluid period H is 1 m (Model 1). Let us consider oil-saturated Model 1 under 5 Hz for an example. (11.1) is used to calculate the slowness to get phase velocities (Figure 5-1). It can be noted that for vertical slow-P-wave, the slowness is infinity, which means the vertical velocity of slow-P-wave is '0'. And the same for vertical S-wave. That's why only vertical fast-P-wave, horizontal fast-P-wave, horizontal slow-

P-wave and horizontal S-wave are studied in this section. And those velocities as a function of seismic frequency are displayed in Figure 5-2.

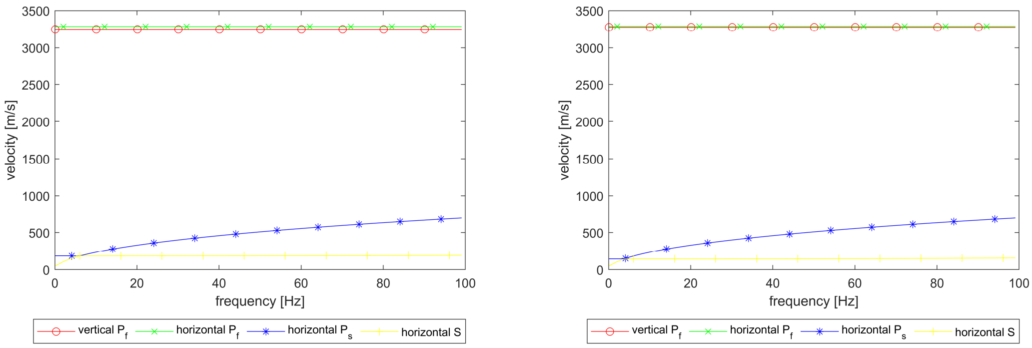

a) Oil saturated

b) Water saturated

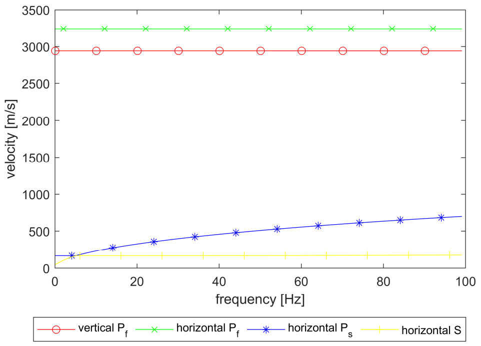

c) CO_2 saturated

Figure 5-2. Velocity dispersion of Model 1.

For the 3 cases, horizontal slow-P-wave and horizontal S-wave are apparently dispersive. There is a swap of their dispersion: Before a certain frequency, the horizontal S-wave is dispersive while horizontal slow-P-wave is not, but after it, they exchanged their property of dispersion. The others are weakly dispersive. Vertical and horizontal fast-P-waves are much faster than horizontal slow-P- and S-wave. The vertical and horizontal fast-P-wave of oil and CO_2 cases are almost the same. The fluid substitution from oil to gas results in a slight variation of vertical fast-P-wave (300 m/s slower in the CO_2 saturated case than the oil saturation). And the fluid substitution from oil to water leads to little change of vertical fast-P-wave.

5.1.2. Model 2

Now the fracture relative thickness ϕ of Block 3 is changed to 0.0001 to represent the media with a smaller void and the other parameters remain unchanged with regards to Model 1. Figure 5-3 gives an overview of the dispersion of Model 2.

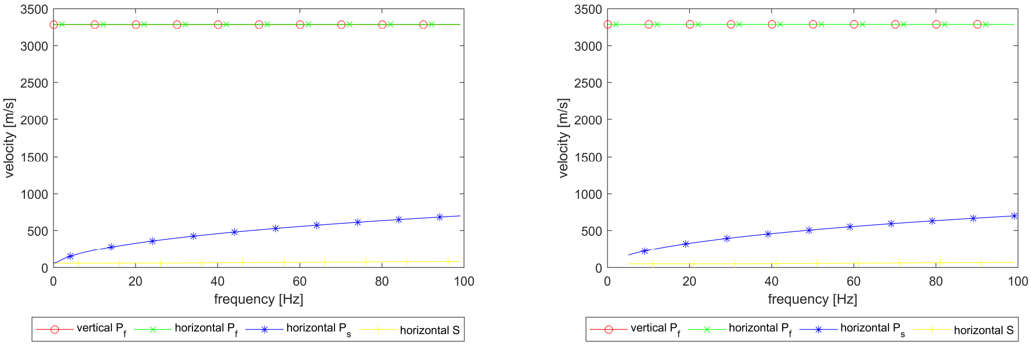

a) Oil saturated

b) Water saturated

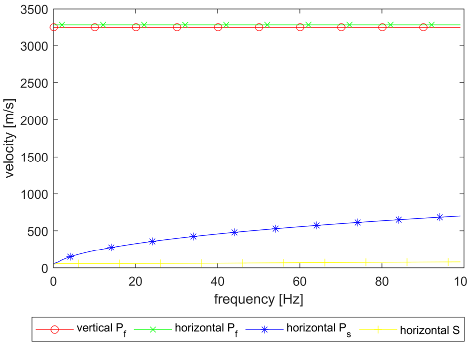

c) CO_2 saturated

Figure 5-3. Velocity dispersion of Model 2.

With smaller fracture relative thickness, the dispersion swap point between horizontal fast-P-wave and horizontal S wave is invisible. And the vertical and horizontal fast-P-wave velocities are very close in each fluid saturation.

5.1.3. Model 3

Here, the length of one period H of Block 3 is shifted from 1 m of Model 1 to 5 m to form Model 3.

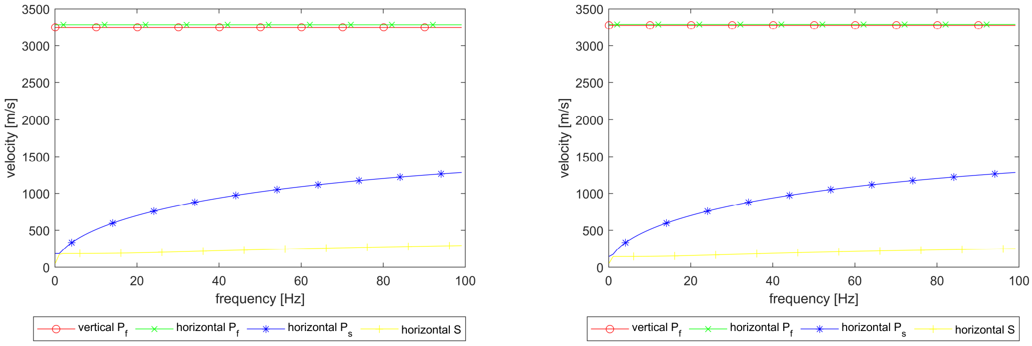

a) Oil saturated

b) Water saturated

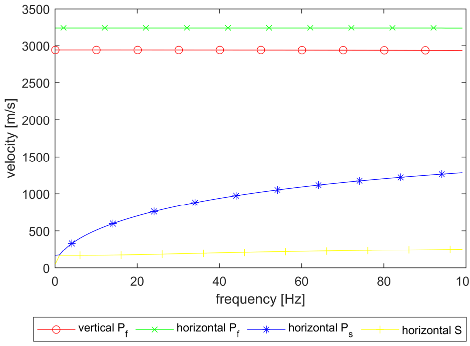

c) CO_2 saturated

Figure 5-4. Velocity dispersion of Model 3.

Figure 5-4 shows that all the features are similar to that of Model 1 except that the horizontal slow-P wave is slightly more faster at a higher frequency than that in Model 1.

5.2. Single phase fluid saturation

In this section, both single layer of Block 3 (Model 1) and Block 3 (Model 1) with overburden are analysed. And the cracked Block 3 is considered only filled with one single fluid. For Model 2 and Model 3, only the travel time of Block 3 with overburden is studied. When it comes to the overall travel time with overburden included, 2 scenarios are considered: P down in Block 1, P down in Block 2, fast-P down in Block3, and fast-P up in Block 3, P up in Block 2, P up in Block 1, and this is called P/fast-P case later; SV down in Block 1, SV down in Block 2, slow P down in Block 3, slow P up in Block 3, SV up in Block 2, SV up in Block 1, and this situation is named SV/slow-P.

5.2.1. Model 1

Single layer

Firstly, it is essential to illustrate how to calculate phase velocity, group velocity and travel time for cracked Block 3.

Let us take oil-saturated Model 1 under 5 Hz frequency as an example. The phase velocity as a function of phase angle is given

$$\frac{1}{v^2} = p^2 + q^2$$
$$\theta = arctan(\frac{p}{q}) \tag{5.1}$$

where θ is the phase angle.

An example of the phase velocity of oil-saturated Model 1 under 5 Hz frequency is shown in Figure 5-5.

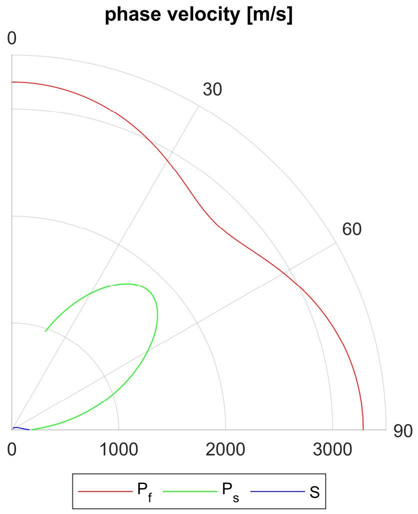

Figure 5-5. Polar plot of phase velocities as a function of angle (oil-saturated Model 1 under 5 Hz frequency).

Then group velocity can be calculated (Tsvankin, 2012),

$$V_x = vsin\theta + \frac{\partial v}{\partial \theta} cos\theta$$
$$V_z = vcos\theta - \frac{\partial v}{\partial \theta} sin\theta \tag{5.2}$$
$$\tan\psi = \frac{V_x}{V_z}$$

where V_x and V_z is the horizontal and vertical group velocity respectively and ψ is the group angle relative to the z-axis.

And finally, the travel time of a single block can be obtained

$$x = 2z\tan\psi$$
$$t = \frac{2z}{V\cos\psi} \tag{5.3}$$

where x is offset; z is the layer thickness and V is group velocity.

The reservoir group velocity and single layer two-way travel time are computed for fast P-, slow P- and S-wave (Figure 5-6 - Figure 5-11).

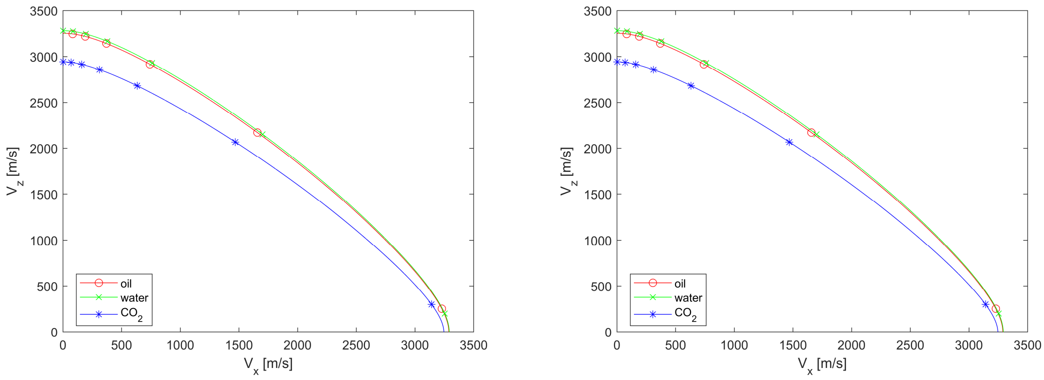

a) 5 Hz

b) 15 Hz

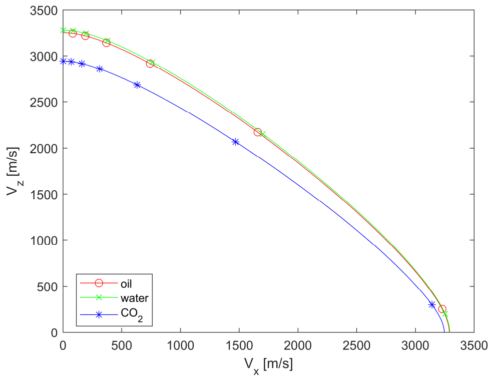

c) 30 Hz

Figure 5-6. Fast-P-wave Group velocity of Block 3 (Model 1).

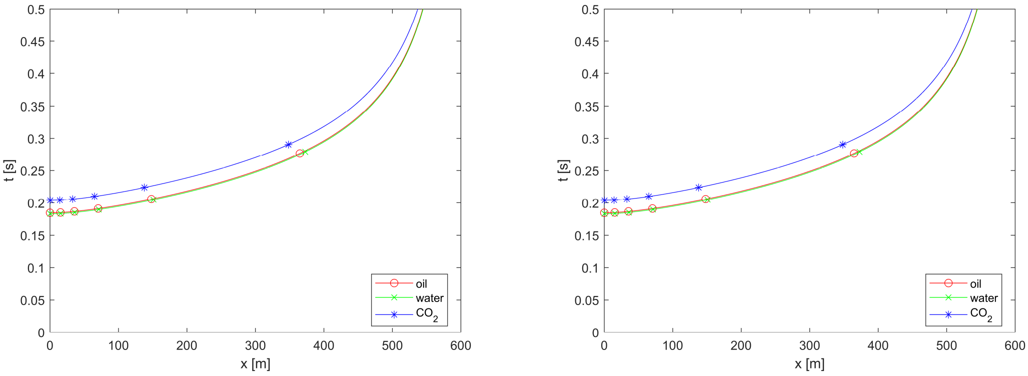

a) 5 Hz b) 15 Hz

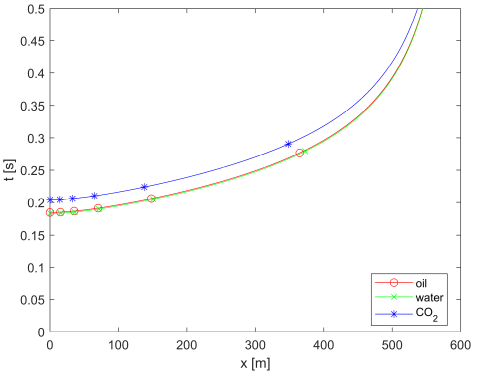

c) 30 Hz

Figure 5-7. Fast-P-wave Two-way travel time of Block 3 (Model 1).

Figure 5-6 shows that the fast-P-wave group velocity varies slightly from oil/water to CO_2 case, except that in the horizontal direction it is not that sensitive to fluid substitution. As a result, the travel time of fast-P-wave in Figure 5-7 changes a little from oil/water to CO_2 saturation (for vertical travel time, approximately 0.2 s more for CO_2 case compared to oil/water case). However, the difference for both group velocity and travel time between oil- and water-saturated cases in the reservoir is too small. Frequency alteration does not affect the fast-P-wave group velocity much.

It can be noticed that slow-P-wave does not travel vertically in group domain in Figure 5-8. Thus, on the travel time recordings (Figure 5-9), slow-P-wave signal emerges after a certain amount of offset. A piece of bad news comes here, that is both the group velocity and travel time of slow-P-wave are not promising to observe fluid substitution. There is only a noticeable difference between oil and water/CO_2 saturation in the travel time of slow-P wave under 5 Hz with larger offset (more than 200 m).

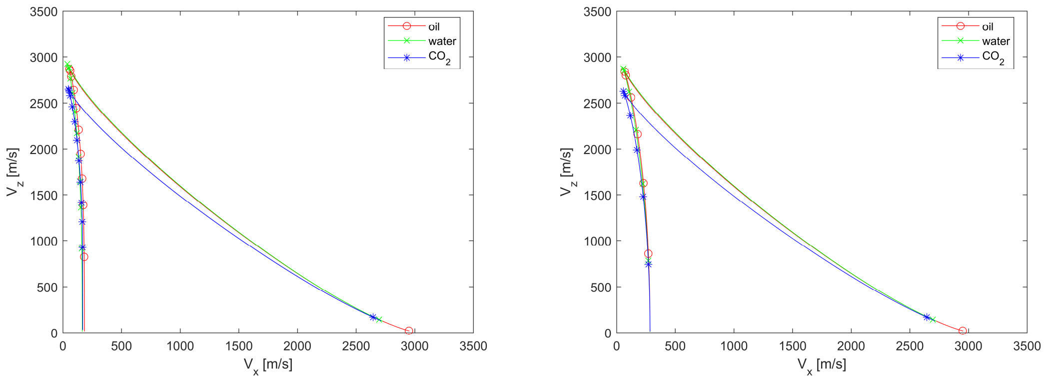

a) 5 Hz

b) 15 Hz

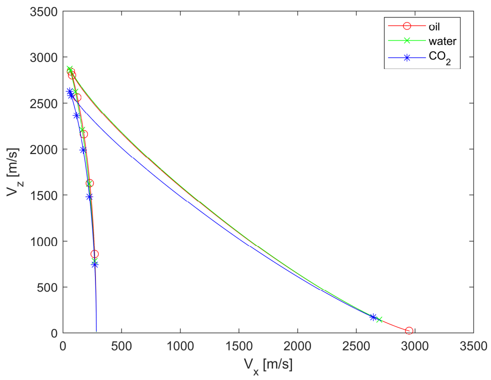

c) 30 Hz

Figure 5-8. Slow-P-wave Group velocity of Block 3 (Model 1).

Analogous to the group velocity of slow-P-wave, S-wave does not travel vertically (Figure 5-10). The S-wave group velocity is generally lower compared to fast- and slow-P-wave. One of the most characteristics is the strong dispersion. As a result, the travel time is very sensitive to seismic dominant frequency (Figure 5-11). For instance, S-wave group velocity decreases from 5 Hz to 15 Hz and 30 Hz. Therefore, the corresponding travel time declines with higher frequency. S-wave emerges with shortest offset with water saturation under 5 Hz seismic frequency. However, the travel time difference only becomes visible with more than 300 m offset. With higher frequency (15 Hz and 30 Hz), the emerging point of the offset can indicate different fluids. For instance, under 15 Hz seismic frequency, the travel time of oil-saturated case emerges at about 280 m offset, followed by 330 m offset of CO_2 and 340 m offset of water. However, the long offset appearance poses a disadvantage of S-wave exploration as long offset seismic data is not always available. As a result, S-wave is not taken into consideration later in the travel time analysis with overburden included.

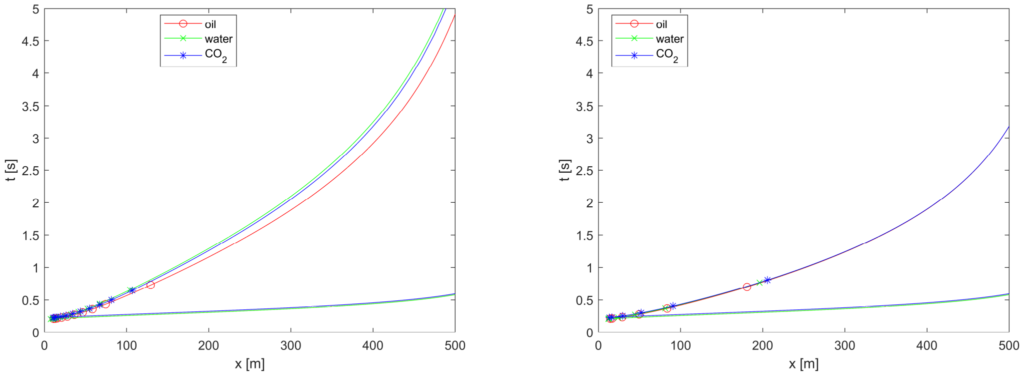

a) 5 Hz

b) 15 Hz

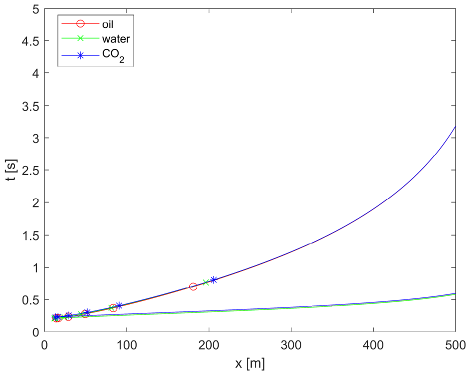

c) 30 Hz

Figure 5-9. Slow-P-wave two-way travel time of Block 3 (Model 1).

One interesting observation here is that, for the group domain of slow-P- and S-waves (Figure 5-8 and Figure 5-10), V_z of both is duplicated for a certain range of V_x. That is why the travel time is also duplicated for some offset (Figure 5-9 and Figure 5-11).

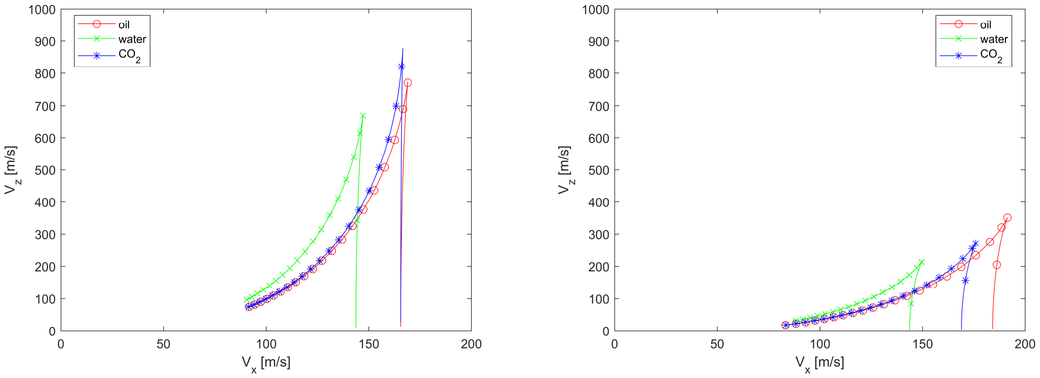

a) 5 Hz

b) 15 Hz

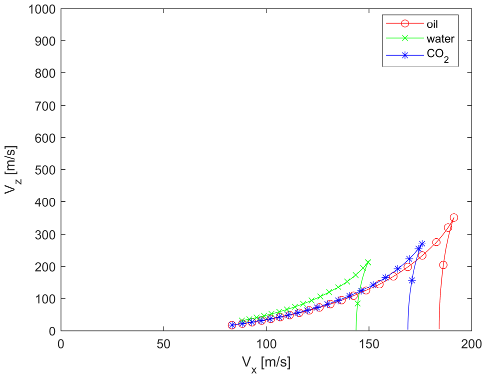

c) 30 Hz

Figure 5-10. S-wave Group velocity of Block 3 (Model 1).

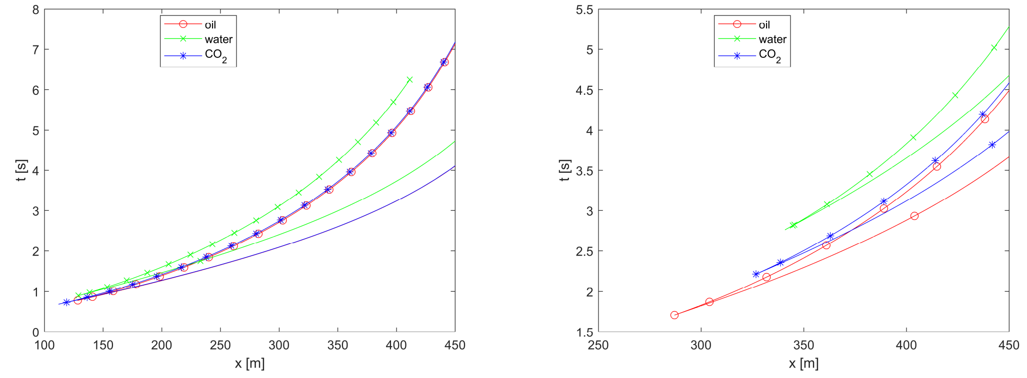

a) 5 Hz

b) 15 Hz

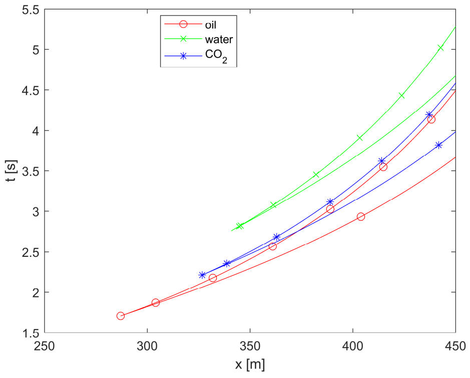

c) 30 Hz

Figure 5-11. S-wave Two-way travel time of Block 3 (Model 1).

Fast-P-wave in the effective model with overburden included

Now we study what happens to P/fast-P case if the overburden Blocks (Block 1 and 2) are included.

To calculate the travel time for a source located on the top of Block 1, the effective group velocity is supposed to be used. To do that, the effective phase velocity is required. Firstly, we calculate effective slowness of the 3 blocks (Block 1, Block 2 and cracked Block 3),

$$\hat{q} = \frac{\sum q_i z_i}{\sum z_i} \tag{5.4}$$

An example of the effective slowness, as well as the separate slowness of the 3 blocks, can be seen in Figure 5-12. Though P/fast-P- waves in the 3 blocks travel horizontally in each block, the effective phase velocity of them does not travel horizontally anymore.

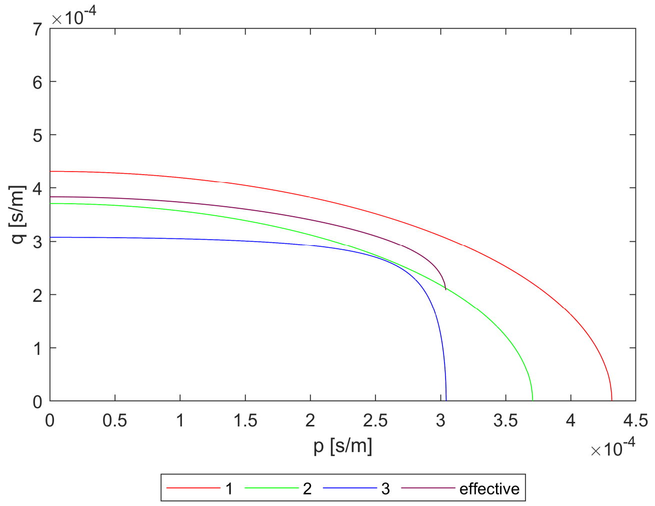

Figure 5-12. Slowness of 3 blocks and the effective slowness of P/fast-P-wave of Model 1 with overburden included (oil-saturated, 5 Hz).

And the effective phase velocity for Figure 5-12 is displayed in Figure 5-13.

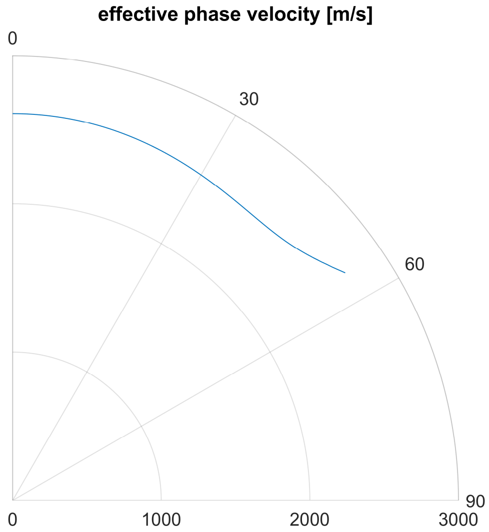

Figure 5-13. Polar plot of effective P/fast-P-wave phase velocity of the effective media consisting of Model 1 with overburden included (oil-saturated, 5 Hz).

Then (5.2) is used to compute effective group velocity from Figure 5-13. And the corresponding two-way travel time can be easily obtained through (5.3).

An overview of the effective P/fast-P-wave group velocity and two-way travel time is given in Figure 5-14 and Figure 5-15.

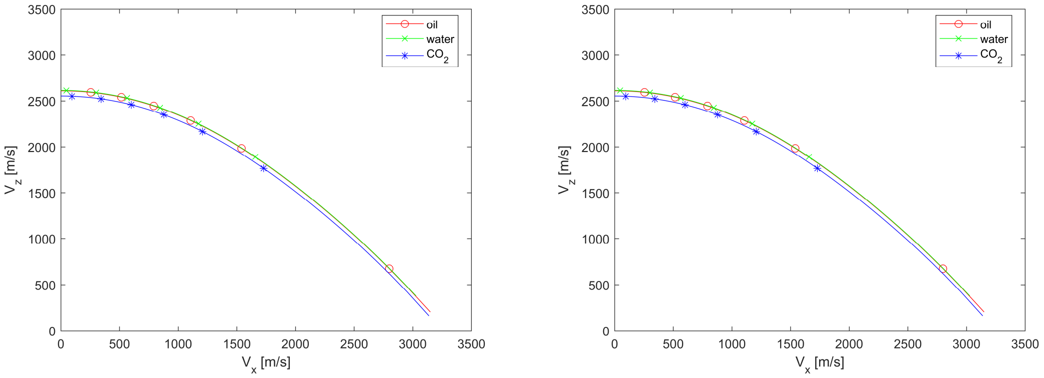

a) 5Hz   b) 15 Hz

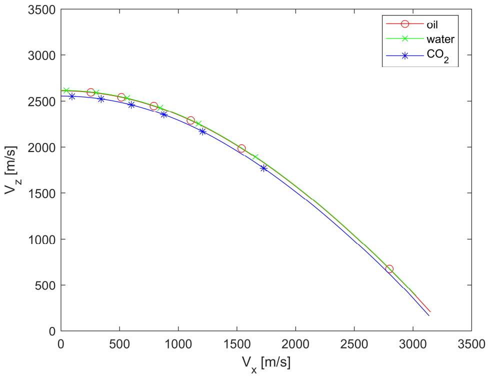

c) 30 Hz

Figure 5-14. Effective P/fast-P-wave group velocity of the effective media (Block 3: Model 1).

Now with overburden included, the difference of group velocity for the 3 fluid saturation cases is much smaller than the single layer case. Still, the oil and water cases are hard to be discriminated in the group velocity in the 3 frequencies (Figure 5-14). And a slight deviation (about 100 m/s for the vertical group velocity) of CO_2 case can be observed compared to oil/water saturation. In the travel time with overburden included, only the fluid substitution from oil/water to CO_2 leads to a visible difference, whose travel time has 0.02 s increase for the vertical travel time. And the travel time is not obviously affected by frequency variation.

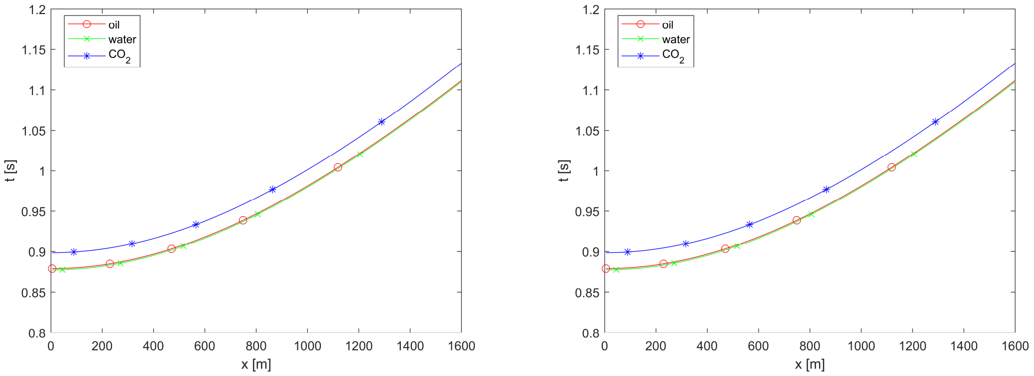

a) 5 Hz b) 15 Hz

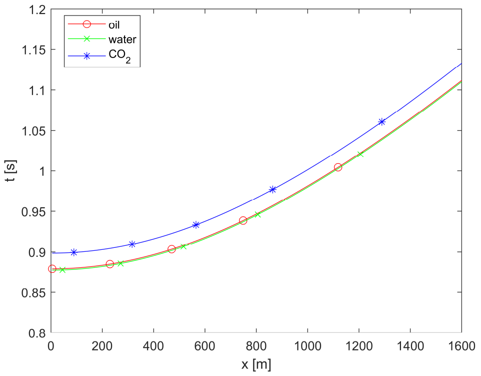

c) 30 Hz

Figure 5-15. Effective two-way travel time of P/fast-P-wave of the effective media (Block 3: Model 1).

SV/slow-P-wave in the effective model with overburden included

Figure 5-16 and Figure 5-17 shows the effective group velocity and travel time with overburden included of SV/slow-P case, respectively.

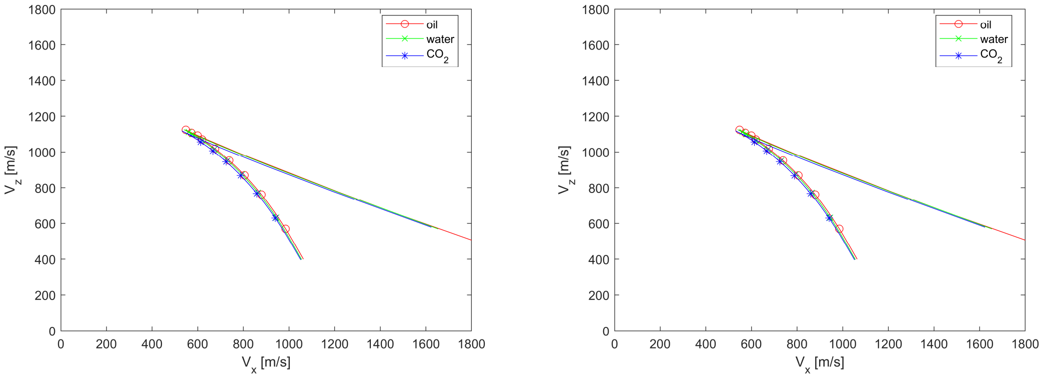

a) 5 Hz b) 15 Hz

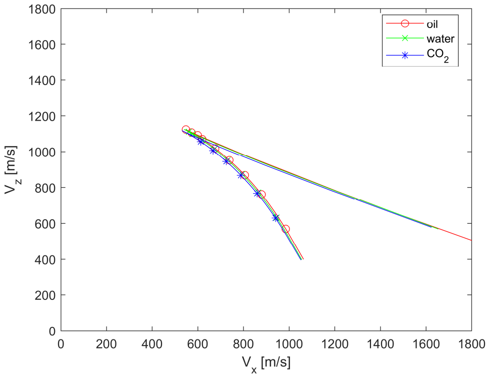

c) 30 Hz

Figure 5-16. Effective SV/slow-P-wave group velocity of the effective media (Block 3: Model 1).

It is not very easy to distinguish if it is the oil, water or CO_2 saturated case through travel time feature of SV/slow-P-wave as the 3 cases are too close in both effective group velocity and effective travel time, though the travel time of CO_2 case is a little longer than that of oil/water but this difference is too insignificant.

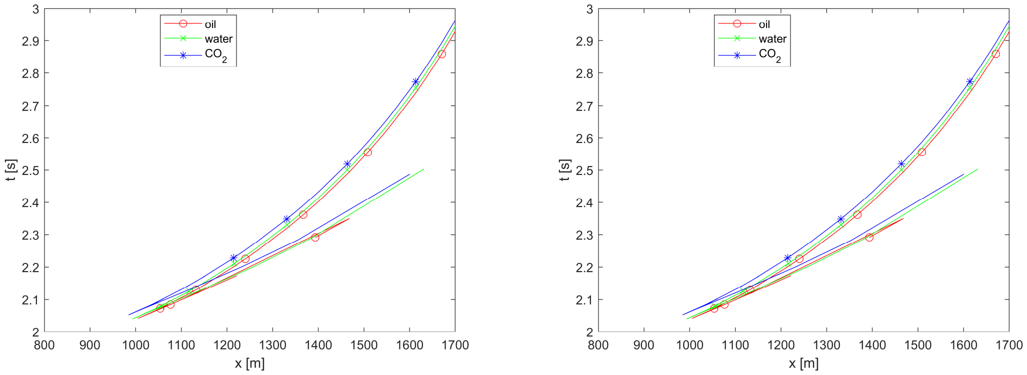

a) 5 Hz b) 15 Hz

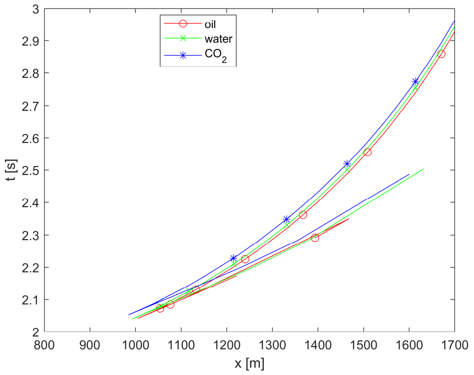

c) 30 Hz

Figure 5-17. Overall SV/slow-P-wave two-way travel time of of the effective media (Block 3: Model 1).

5.2.2. Model 2

In this section, only the effective travel time with overburden included for P/fast-P-wave and SV/slow-P-wave is shown (Figure 5-18 and Figure 5-19). And ϕ is shifted to 0.0001 to form Model 2 and the other parameters remain the same with Model 1.

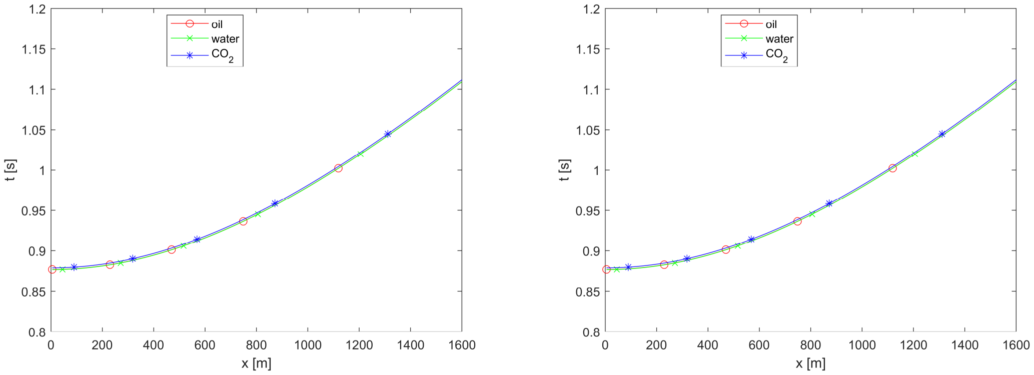

a) 5 Hz

b) 15 Hz

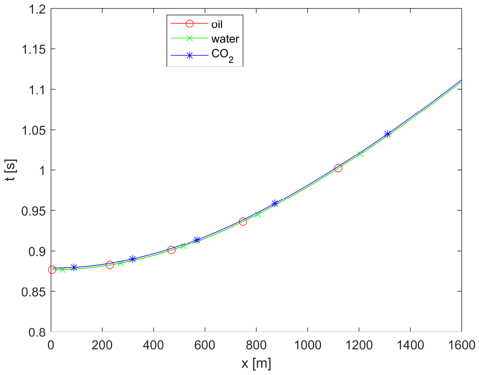

c) 30 Hz

Figure 5-18. Overall travel time of P/fast-P-wave of the effective media (Block 3: Model 2).

The outcome for this model is disappointing. The difference for the 3 fluid saturations is much smaller than that in Model 1, and now it is almost impossible to distinguish any fluid from the travel time of both P/fast-P-wave and SV/slow-P-wave under the 3 frequencies.

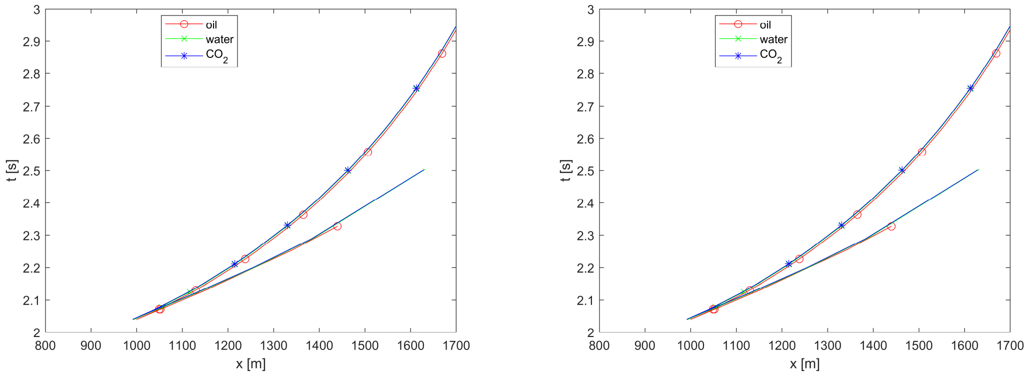

a) 5 Hz b) 15 Hz

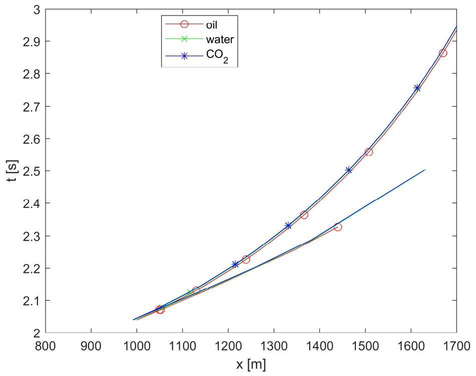

c) 30 Hz

Figure 5-19. Overall travel time of SV/slow-P-wave of the effective media (Block 3: Model 2).

5.2.3. Model 3

The period of one solid and one fluid layer H in model 3 is set 5 m and the other properties are the same with Model 1. Figure 5-20 and Figure 5-21 give the travel time of P/fast-P-wave and SV/slow-P-wave in the whole model. The travel time in this model is almost the same as that in Model 1. Only the substitution from oil/water to CO_2 can be discriminated by the travel time of P/fast-P-wave while the travel time of SV/slow-P-wave for oil/water and CO_2 cases is too similar to each other.

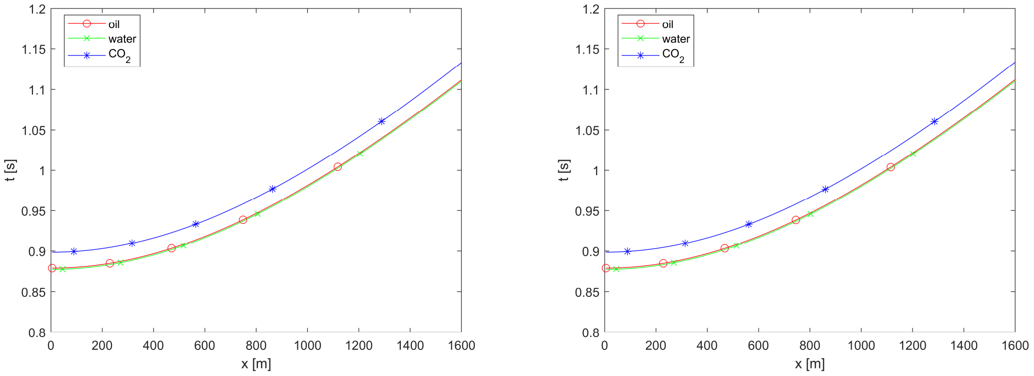

a) 5 Hz

b) 15 Hz

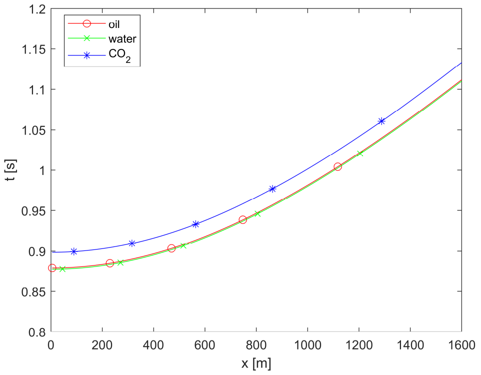

c) 30 Hz

Figure 5-20. Overall travel time of P/fast-P-wave of the effective media (Block 3: Model 3).

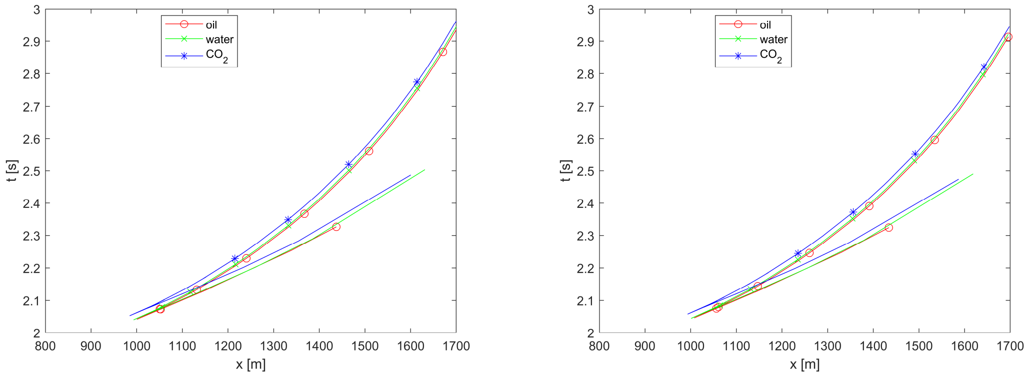

a) 5 Hz

b) 15 Hz

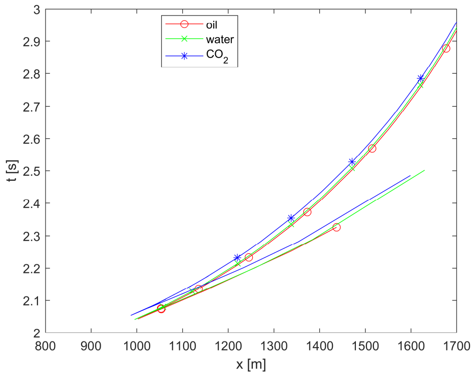

c) 30 Hz

Figure 5-21. Overall travel time of SV/slow-P-wave of the effective media (Block 3: Model 3).

5.3. Mixed phase case

Before, the study of fluid substitution is constrained to single phase saturation. In reality, this is not always the case and is taken over by mixed-saturation. As fast-P- and slow-P- wave is not very sensitive to the frequency in the seismic range, it is, therefore, enough to analyse the seismic response under a certain frequency. In this section, 5 Hz is applied. In addition, the fluid substitution from oil to water does not make so much difference in the travel time with overburden included, so only the substitution for P/fast-P-wave from oil to CO_2 is investigated. In addition, the travel time of SV/slow-P with overburden included is not displayed here as it is not very much affected by the fluid substitution from oil to CO_2 as mentioned before.

To calculate the travel time and reflectivity of the mixed phase saturation, the effective P-wave velocity for the mixed phase is required. Firstly, the effective bulk modulus of mixed oil-gas phase is given (Stovas & Landrø, 2004),

$$\frac{1}{K_f} = \frac{S_o}{K_o} + \frac{1-S_o}{K_g} \tag{5.5}$$

where K_f is the effective bulk modulus; K_o and K_g is the bulk modulus of oil and water respectively; S_o is the oil saturation. And the density ρ_f of the mixed phase is just the volume-weighted average. Then the P-wave velocity for the mixed fluid can be obtained with the fluid modulus K_f and density ρ_f. The slowness and P/fast-P-wave travel time with overburden included are shown in Figure 5-22 and Figure 5-23 for different saturation of oil for oil-CO$_2$ mixed phase system.

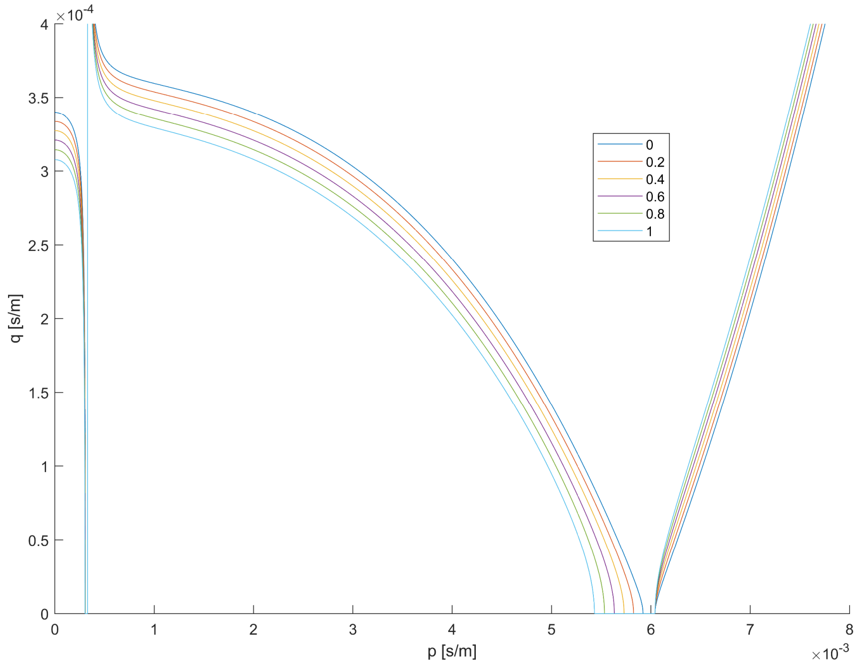

Figure 5-22. Slowness of cracked Block 3 (ϕ = 0.001) filled with oil-CO$_2$ mixed phase (5 Hz). The number in the legend indicates the oil saturation.

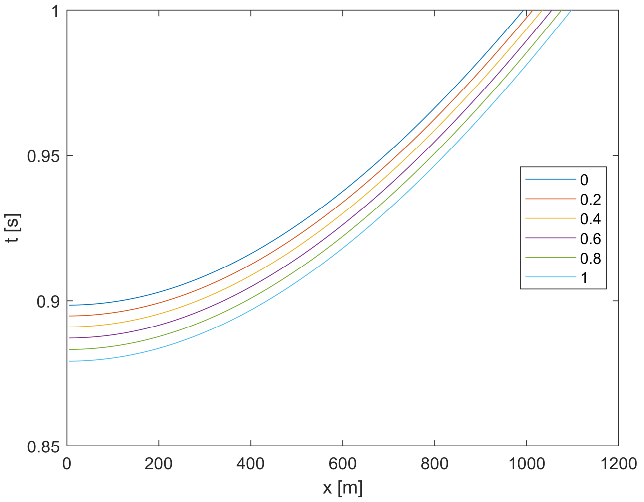

Figure 5-23. P/fast-P-wave travel time of cracked Block 3 ($\phi = 0.001$) filled with oil-CO_2 mixed phase with overburden included (5 Hz). The number in the legend is the oil saturation.

From Figure 5-22, it can be observed that as the oil saturates more, q of fast-P- and slow-P-wave is climbing for the same p, while that of S-wave drops.

The travel time of P/fast-P-wave with overburden included shows that it changes gradually to a longer time if the oil is replaced by CO_2. The difference of different saturation cases vary the most at the vertical travel time and then lessens with larger offset. However, the vertical travel time change is very small for every ‘0.2’ oil-saturation change.

6. Reflectivity

Amplitude versus angle (AVA) is an effective tool for fluid identification. In this chapter, P/fast-P (P/fast-P-wave incident and P/fast-P-wave reflection) reflectivity on the interface between Block 2 and Block 3 is studied.

Firstly, let us recall the 2-term acoustic approximation to the Zoeppritz equations

$$\begin{gathered}R_{pp}\left(\theta\right)\approx R_0+R_2 sin^2\left(\theta\right)\\ R_0=\frac{\Delta Z}{2\overline{Z}_{p0}}\\ R_2=\frac{1}{2}\left[\frac{\Delta v_{p0}}{\overline{v}_{p0}}-\left(\frac{2\overline{v}_{s0}}{\overline{v}_{p0}}\right)^2\frac{\Delta\mu_0}{\overline{\mu}_0}+\Delta\delta\right]\end{gathered}\qquad(6.1)$$

where Z_{p0} is the vertical acoustic impedance ρv_{p0}; μ_0 is the vertical shear modulus ρv_{s0}^2.

In case R_{pp} is plotted as a function of $sin^2\theta$, then R_0 and R_2 can be interpreted intercept and gradient respectively.

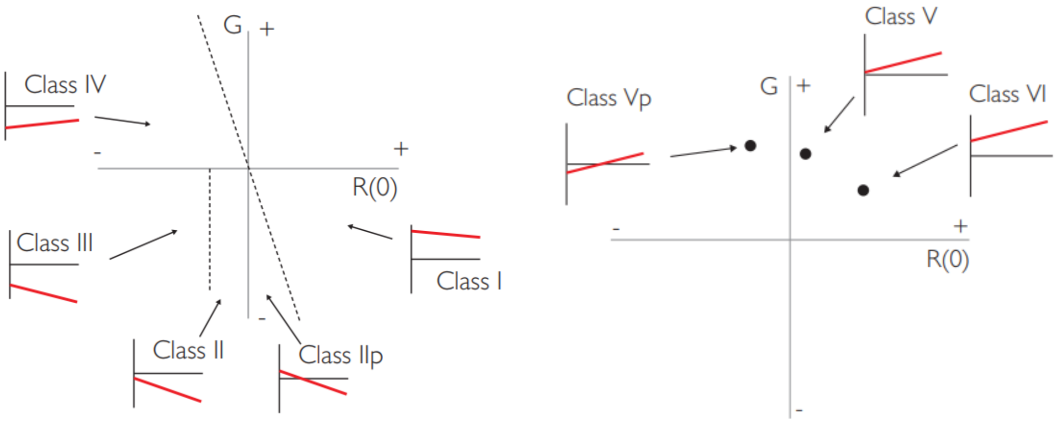

a) 5 common patterns of negative gradients

b) Additional AVO classes for responses with positive gradients (such as base of sands and hydrocarbon contacts)

Figure 6-1. AVO patterns (Simm & Bacon, 2014).

According to Simm and Bacon (2014), there are 6 patterns of AVO. And they stated that Positive AVO with a positive intercept is generally characteristic of modelled hydrocarbon contacts, while lithological changes with positive intercept usually have a negative gradient.

Firstly, the parameters of Block 2 are all known for (6.1) from the result of up-scaling of Section 4.1. Now, some approximations should be made to formulate the parameters in (6.1) for Block 3.

A model of alternating solid/fluid layers can be regarded as polar anisotropy, which is analogous to VTI media. Here, the reflectivity of VTI is applied to approximate the reflectivity between Block 2 (VTI) and cracked Block 3 (analogue VTI). To do so, the Thomsen parameter δ of cracked Block 3 is required, which is obtained by fitting the $q(p)$ of Block 3 with $q(p)$ of VTI media.

6.1. Taylor series of q(p) for VTI

Firstly, we show how to approximate Thomsen parameter δ for cracked Block 3.

Inserting the last 3 equations into the first 2 in (3.4) leads to the 2D elastic wave equation for VTI media,

$$\begin{aligned} \rho\frac{\partial^2 u_x}{\partial t^2} &= C_{11}\frac{\partial^2 u_x}{\partial x^2}+\left(C_{13}+C_{55}\right)\frac{\partial^2 u_z}{\partial x\partial z}+C_{55}\frac{\partial^2 u_x}{\partial z^2} \\ \rho\frac{\partial^2 u_z}{\partial t^2} &= C_{33}\frac{\partial^2 u_z}{\partial z^2}+\left(C_{13}+C_{55}\right)\frac{\partial^2 u_x}{\partial x\partial z}+C_{55}\frac{\partial^2 u_z}{\partial x^2} \end{aligned} \tag{6.2}$$

And then applying Fourier transform in both spatial and temporal domain yields Christoffel wave equation:

$$\begin{pmatrix} C_{11}k_x^2+C_{44}k_z^2-\rho\omega^2 & \left(C_{13}+C_{44}\right)k_xk_z \\ \left(C_{13}+C_{44}\right)k_xk_z & C_{44}kx^2+C_{33}k_z^2-\rho\omega^2 \end{pmatrix}\begin{pmatrix} U_x \\ U_z \end{pmatrix}=0 \tag{6.3}$$

As there is supposed to be a non-zero solution of $\begin{pmatrix} U_x \\ U_z \end{pmatrix}$, it is necessary to have

$$\det\begin{pmatrix} C_{11}k_x^2+C_{44}k_z^2-\rho\omega^2 & \left(C_{13}+C_{44}\right)k_xk_z \\ \left(C_{13}+C_{44}\right)k_xk_z & C_{44}kx^2+C_{33}k_z^2-\rho\omega^2 \end{pmatrix}=0 \tag{6.4}$$

Then the relation of q and p is formulated as below

$$
\begin{aligned}
q(p) = {} & \sqrt{2}C_{33}\rho + C_{44}\rho(-(C_{11}^2C_{33}^2p^4 - 2C_{11}C_{13}^2C_{33}p^4 \\
& -4C_{11}C_{13}C_{33}C_{44}p^4 - 2C_{11}C_{33}^2p^2\rho - 4C_{11}C_{33}C_{44}^2p^4 \\
& +2C_{11}C_{33}C_{44}p^2\rho + C_{13}^4p^4 + 4C_{13}^3C_{44}p^4 \\
& +2C_{13}^2C_{33}p^2\rho + 4C_{13}^2C_{44}^2p^4 + 2C_{13}^2C_{44}p^2\rho \\
& +4C_{13}C_{33}C_{44}p^2\rho - 2C_{33}C_{44}\rho^2 + C_{44}^2\rho^2)^{0.5} \\
& +C_{13}^2p^2 - C_{11}C_{33}p^2 + 2C_{13}C_{44}p^2)^{0.5}(2\sqrt{C_{33}C_{44}})
\end{aligned}
\tag{6.5}
$$

Substitute all stiffness to the combination of v_{p0}, v_{s0}, ρ and Thomsen parameters, apply Taylor expansion to $q(p)$ at $p=0$ and retain until 4th order to formulate a much simpler formula as below

$$
q \approx \frac{1}{v_{p0}} - \left(\delta + \frac{1}{2}\right) v_{p0} p^2 \tag{6.6}
$$

6.2. Fitting q(p) for cracked Block 3

(6.6) can be used to approximate pseudo δ of Block 3 by fitting $q(p)$. It should be noted that (6.6) is only an approximation to small phase angles or p. With larger p, the equation will lead to large errors. So, fitting can be only performed within small p. Figure 6-2 is an example to estimate δ of Block 3 using (6.6). And the same procedure is carried out for different fluids of cracked Block 3 for all the 3 models. It has been found that vertical fast-P-wave is weakly dispersive before. So, it is enough to analyze under a certain low frequency.

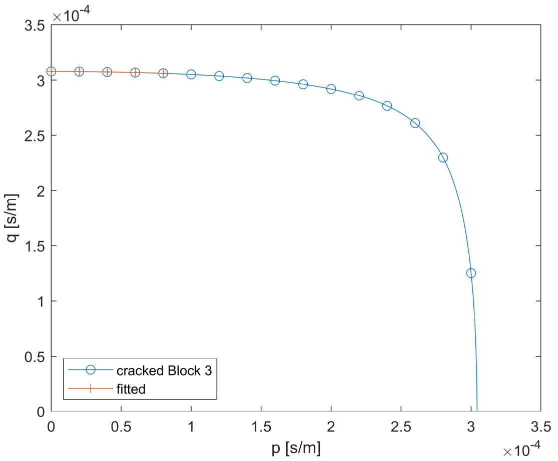

Figure 6-2. Fitting q(p) for fast-P-wave for cracked and oil saturated Block 3, 5Hz, Model 1. Fitting is operated on P-wave phase angle from 0 to $\frac{\pi}{12}$. Estimation results: $v_{p0} = 1773\mathrm{m/s}$; $\delta = -0.4217$, $r^2 = 0.9996$. r^2 is the coefficient of determination (ranging from ‘0’ to ‘1’, ‘1’ means perfect fitting).

δ computed from this method is effective δ if the cracked Block 3 is treated as a homogenous VTI media. They are summarized in Table 6-1.

Table 6-1. δ for cracked block 3 approximated from VTI equivalence.

Model	Saturation	δ	r^2
1	Oil	-0.4217	0.9996
	Water	-0.4225	0.9996
	CO_2	-0.4242	1.0000
2	Oil	-0.4233	0.9996
	Water	-0.4266	0.9996
	CO_2	-0.4090	1.0000
3	Oil	-0.4219	0.9994
	Water	-0.4227	0.9997
	CO_2	-0.4245	0.9977

6.3. Single phase case

Let us recall the P-fast-P reflectivity computation formula (6.1), which requires the input of v_{p0}, v_{s0}, ρ and δ for both up and down half-spaces.

v_{s0} is set 0 for cracked Block 3 as there is no vertical S-wave velocity at all. And due to the fluid effect, ρ is not the density of the matrix, but the effective density averaged from solid and fluid, which is computed by

$$\rho = \phi\rho_f + (1-\phi)\rho_s \tag{6.7}$$

where ρ_s is the solid density.

Now, all the parameters are ready for (6.1) and the P/fast-P-wave reflectivity of between the overburden and the 3 models (5 Hz) can be calculated (Figure 6-3).

Now, we can classify R_0 - R_2 pattern according to Figure 6-1 and they are listed in Table 6-2. As mentioned in Simm and Bacon (2014), ‘There is nothing about these responses that allow us to generalise about their significance’, which means those AVO patterns are restricted to our current model to identify fluids.

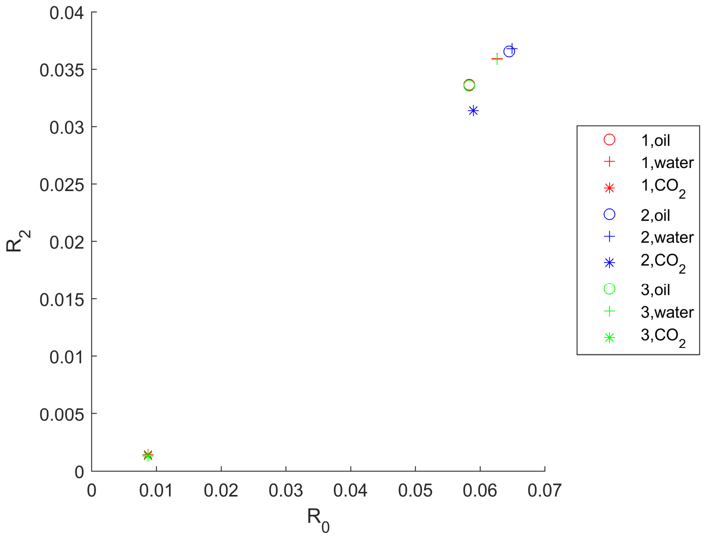

Figure 6-3. R_2 as a function of R_0 for a wave going from Block 2 to the interface between Block 2 and cracked Block 3. This is computed with seismic frequency 5 Hz. The red ‘O’ and the green ‘O’, the red ‘+’ and the red ‘+’ and the green ‘*’ and the green ‘*’ almost overlap, i.e. the cross plot of Model 1 and Model 3 is overlapped.

Table 6-2. AVO pattern classification of the 3 models with different fluid saturation.

Model	Saturation	AVO pattern
Model 1	Oil	VI
	Water	VI
	CO_2	V
Model 2	Oil	VI
	Water	VI
	CO_2	VI
Model 3	Oil	VI
	Water	VI
	CO_2	V

One interesting phenomenon in Figure 6-3 is that all events have positive intercept with a positive gradient, which is not very common in the seismic AVO analysis. It arises from the considerably high anisotropy of the cracked Block 3.

Another apparent observation is that Model 1 and Model 3 almost have the same behaviours. The reason is that through fitting q(p) of the cracked Block 3 with VTI theory, we are considering cracked Block 3 as an effective media, and this is a long-wavelength approximation. So, the difference of parameter H does not affect much to the result of reflectivity. Thus, Model 1 and Model 3 are equivalent in long-wavelength approximation and can be regarded as the same case.

As for the fluid substitution in Model 1 and Model 3, both R_0 and R_2 are slightly shifted to the higher values (both increase about 0.03) when the oil is replaced by water while they decline a lot (R_0 drops 0.05 and R_2 decreases 0.033 approximately) when the oil is substituted by CO_2.

For Model 2, the fluid effect is considerably smaller than Model 1 and Model 3 as the void is much less. There is no much difference for R_0 - R_2 for fluid changing from oil to water and only a small change (both R_0 and R_2 decrease 0.05) from oil to CO_2.

6.4. Mixed phase case

In the previous section, only the substitution from oil saturation to CO_2 saturation for Model 1 and Model 3 has a big difference in R_0 - R_2 crossplot. Thus, it is interesting to study the partially saturated case by both fluids and see how the gradual displacement from one fluid to another affects the reflectivity. As Model 1 and Model 3 have very similar reflectivity feature, it is reasonable to use the reflectivity response of Model 1 to represent Model 3. In this section, Model 1 is used and R_0 - R_2 cross plot is given in Figure 6-4.

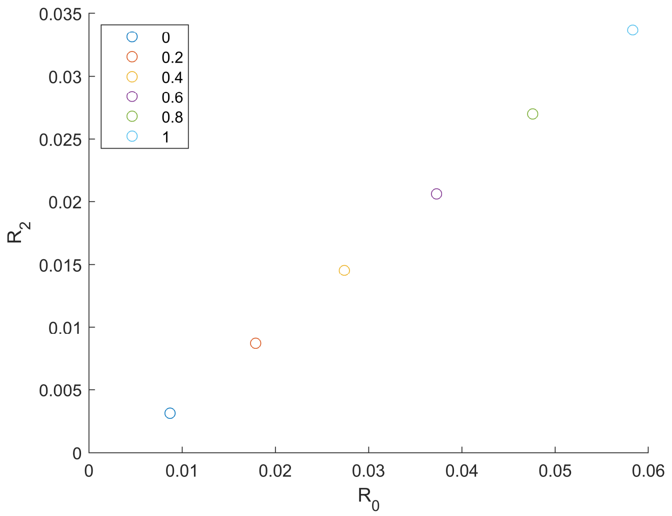

Figure 6-4. R_2 as a function of R_0 for a wave going from Block 2 to the interface of Block 2 and cracked Block 3 (Model 1, $\phi = 0.001$, H = 1 m). The value in the legend is the oil saturation for oil-CO_2 mixed phase system.

The reflectivity change is very like the linear change with the saturation variation. For every 0.2 oil saturation decreasing, R_0 drops about 0.01 and R_2 declines about 0.0064.

7. Numerical simulation

This chapter elaborates the procedure of using the finite-difference method in Matlab to simulate the wave propagation in the model constructed from the well log data, in which Block 3 is cracked. As a result, there are 2 types of media, VTI media without any void and fractured Block 3 filled with fluid.

As there is currently no unified wave equations to describe both of them, the author used the combination of 2 kinds of wave equations to simulate the wave in each of them, acoustic wave equation for alternating solid and fluid layers under long-wavelength approximation (Schoenberg, 1984) and acoustic wave equation for VTI media (Alkhalifah, 2000). And both of them can be solved by the finite-difference method. Here the finite-difference method in the frequency domain (x, z, ω) is applied. And the perfectly matched layer (PML) is employed to attenuate the energy going to the boundary to avoid unwanted reflection. The boundary condition is absorbing boundary condition (ABC).

7.1. Wave equation for VTI

Alkhalifah (2000) proposed an acoustic equation for VTI media in (x,z,t) domain consisting of 2 partial differential equations given below

$$\begin{gathered}\frac{\partial^2 P}{\partial t^2} = (1+2\eta)v^2\frac{\partial^2 P}{\partial x^2} + v_v^2\frac{\partial^2 P}{\partial z^2} - 2\eta v^2 v_v^2\frac{\partial^4 F}{\partial x^2 \partial z^2} \\ P = \frac{\partial^2 F}{\partial t^2}\end{gathered} \tag{7.1}$$

where $\eta = \frac{\epsilon - \delta}{1+2\delta}$ and v_v is the NMO velocity given as $v_v = v_{p0}\sqrt{1+2\delta}$.

(7.1) can compute the P-wave pressure field P. However, there are 2 fields in (7.1), P and F. Considering the computation burden, it is always better to simplify the system of equations. If we substitute F with P in (7.1), then only one field P left but the integral of P comes out.

Here is a better solution, which is to transform (7.1) into $P(x,z,\omega)$ analogous to (3.6). And (7.1) will be converted to a very simple form subject to P

$$-\omega^2 P = (1+2\eta)v^2\frac{\partial^2 P}{\partial x^2} + v_v^2\frac{\partial^2 P}{\partial z^2} + \frac{2\eta v^2 v_v^2}{\omega^2}\frac{\partial^4 P}{\partial x^2 \partial z^2} \tag{7.2}$$

7.2. Wave equation for alternating solid and fluid layers

Schoenberg (1984) formulated the slowness relation under long-wavelength condition ($\omega \to 0$):

$$\begin{gathered}(v_{pl}^{-2} - p^2)\left(\frac{q^2}{\langle\rho\rangle} + p^2\frac{1}{\langle\rho\rangle} - \langle\frac{1}{\rho v_p^2}\rangle\right) = p^2\phi(v_p^2 - p^2)\rho^{-1} \\ v_{pl} = 2(1-\frac{v_s^2}{v_p^2})^{0.5} v_s\end{gathered} \tag{7.3}$$

where v_p and v_s is the P- and S-wave velocity of the solid respectively; ρ is the solid density; the operator ‘ $\langle\rangle$ ’ means thickness-weighted average; v_{pl} is the long wavelength speed of the extensional wave.

Recall inverse Fourier transform,

$$\begin{gathered}ik_x = i\omega p = \frac{\partial}{\partial x} \\ ik_z = i\omega q = \frac{\partial}{\partial z}\end{gathered} \tag{7.4}$$

where the second and the third terms are in the frequency domain.

Apply theorem (7.4) to (7.3), and then multiply pressure $P(x,z,\omega)$ on both sides to form the non-dissipative acoustic wave equation in (x,z,ω)

$$\begin{aligned}&(-\omega^2 v_{pl}^{-2} - \frac{\partial^2}{\partial x^2})\left(\frac{1}{\langle\rho\rangle}\frac{\partial^2 P}{\partial z^2} + \frac{1}{\langle\rho\rangle}\frac{\partial^2 P}{\partial x^2} + \langle\frac{1}{\rho v_p^2}\rangle\omega^2 P\right) \\ &= \frac{\phi}{\rho}(-\frac{\omega^2}{v_p{}^2} - \frac{\partial^2}{\partial x^2})\frac{\partial^2 P}{\partial x^2}\end{aligned} \tag{7.5}$$

(7.5) is a 4th order partial differential equation can be applied to the cracked reservoir.

7.3. Results of wavefield

The detail of finite-difference implementation is listed in Appendix 11.3 and the source code is given in Appendix 11.6.

As (7.5) is under long-wavelength approximation, the wavelength is assumed much larger than H. Thus, there is no H input in (7.5) and Model 1 and Model 3 in Table 4-1 are considered to have the same wave behaviour. The 3 models in Table 4-1 are tested but only Model 2 yields an ingressive result with a moderate signal to noise ratio. As a result, only the result of Model 2 is shown in this section.

There are 2 cases to be simulated, the first one is that the source is placed in Block 2 very close to the top of the cracked Block 3 to see the propagation of fast P- and slow P- wave and the transmission from P-wave in Block 2 to the 2 waves in Block 3; the second one is Figure 4-3, our whole model.

7.3.1. Wavefield in cracked Block 3

Firstly, we place the 20 Hz dominant frequency source 20 m above the interface between Block 2 and Block 3. With all the information above, the finite-difference method is executed. Some examples of the wavefield in the frequency domain for oil-saturated Block 3 are given in Figure 7-1.

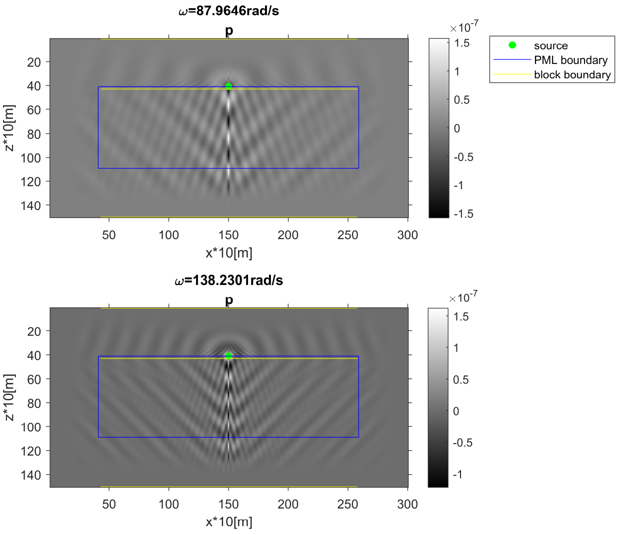

Figure 7-1. Wavefield in frequency domain of cracked Block 3 (oil saturated, $\phi = 0.0001$) where the source is located 20 m above the top of Block 3. Block 2 and Block 3 is bounded by the yellow line.

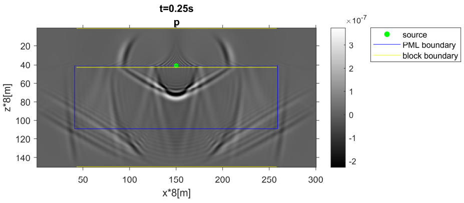

a) Cracked Block 3: $\phi = 0.1$, oil-saturated. The source is 20 m above the interface

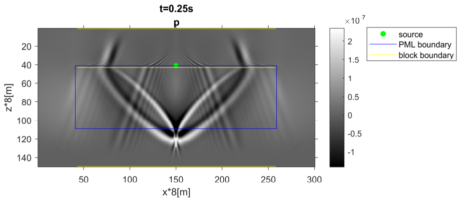

b) Cracked Block 3: $\phi = 0.0001$, oil-saturated. The source is 20 m above the interface

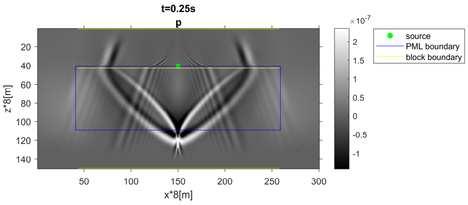

c) Cracked Block 3: $\phi = 0.0001$, gas-saturated. The source is 20 m above the interface

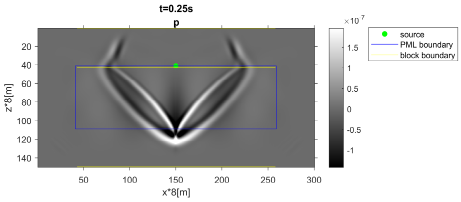

d) Cracked Block 3: $\phi = 0.0001$, oil-saturated. Block 2 is set isotropic on purpose to avoid S-wave artefact. The source is 20 m above the interface

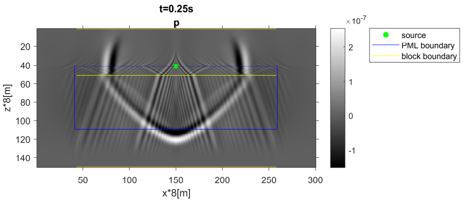

e) Cracked Block 3: $\phi = 0.0001$, oil-saturated. The source is 100 m above the interface

Figure 7-2. Snapshots of wavefield in time domain. The source is placed in Block 2. And Block 2 and Block 3 are bounded by the yellow line.

And then the inverse Fourier transform is used to transfer the field back to the time domain in Figure 7-2 a), which includes some extra test for different input. It is the S-wave artefact in Block 2 that raises a lot of noise in the time domain. But the signal can still be seen clearly.

Now, some other scenarios are tested as shown in Figure 7-2. As predicted by Schoenberg (1984), two waves, the fast-P-wave and slow-P-wave can be observed in Figure 7-2 a), b), c) and d). The wavefield here does not contain the S-wave as this is acoustic wave equation but there is some S-wave artefact when the media is anisotropic.

Figure 7-2 a) gives an example of higher crack relative thickness ϕ, and the complete shape of slow-P-wave can be observed. However, when the relative thickness of the fracture becomes much smaller, the inner part of slow-P-wave becomes much weaker in Figure 7-2 b) and c). It is necessary to emphasise that the slow-P-wave in the 2 figures could be easily misunderstood as S-wave artefacts like the S-wave artefact in acoustic VTI media. But it is not the S-wave artefact as the incomplete wavefront in Figure 7-2 b) and c) conforms to the slow-P-wave group velocity.

The wavefronts in Figure 7-2 b) and c) are very similar to each other (the velocities are so close). This supports what we concluded in section 5.1.2: There is no obvious change of travel time when the fluid in cracked Block 3 (Model 2) alters from oil to CO_2.

Another finding is that if we set Block 2 isotropic (Figure 7-2 d)), then there is no S-wave artefact in Block 2 so that it does not propagate to cracked Block 3. In this case, the noise is much less than the anisotropic case of Block 2 (e.g., Figure 7-2 b)).

Then, we try to place the source farther away from the interface of Block 2 and Block 3 (Figure 7-2 e)). The distance between the source and the interface is set 100 m. The slow-P-wave is invisible. The explanation for this is that the transmission from P-wave in Block 2 to slow-P-wave in Block 3 is very small. When the source is very close to the interface, the energy going to Block 3 is strong enough to make slow-P-wave visible. When the source is farther, then the input energy to transmit slow-P-wave in Block 3 is much weaker due to the geometric spreading.

7.3.2. Wavefield in the whole model

In this subsection, the cracked Block 3 with $\phi = 0.0001$ with overburden and underburden included is simulated. An example of snapshot is given in Figure 7-3.

A moderate degree of noise can be seen in the wavefield plot. But it is still possible to identify the signal. The whole wavefield only contains acoustic wave and S-wave is out of the scope of this simulation. There is a line of receivers placed on the top of Block 1, which generates the recordings in Figure 7-4. To compare the consequence of fluid substitution, the difference of the recordings is followed.

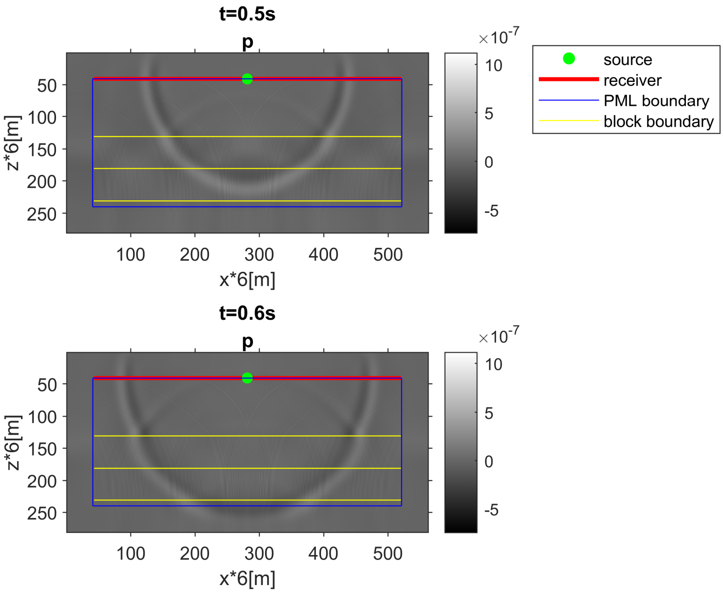

Figure 7-3. Snapshot of the wavefield in time domain of the whole model with cracked Block 3 (ϕ = 0.0001), oil-saturated.

In Figure 7-3, the slow-P-wave in cracked Block 3 is invisible so that in the seismograms, there is no reflection related to slow-P-wave. In the synthetic seismograms (Figure 7-4, a), b) and c)), 3 reflection events appear, PP1, PP2 and PP3. In Figure 7-4 d), the difference between the oil- and water-saturated cases are shown. The difference of PP3 emerges as there is a time shift in the oil and water saturation for PP3 event. However, the difference is very small and the noise is comparable to the intensity of the signals The difference of reflectivity of PP2 is too weak to be seen on the difference. When it comes to the difference between CO_2 and oil saturation (Figure 7-4 e)), the signal of PP2 difference is stronger to be visible. And the difference of PP3 is also more obvious. Thus, in our simulation, the fluid substitution from oil to CO_2 is more possible to be detected by seismics than that from oil to water for Model 2 with overburden and underburden included.

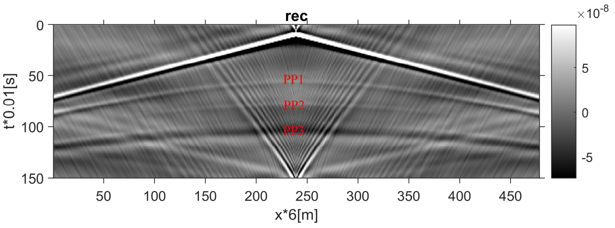

a) Oil saturated

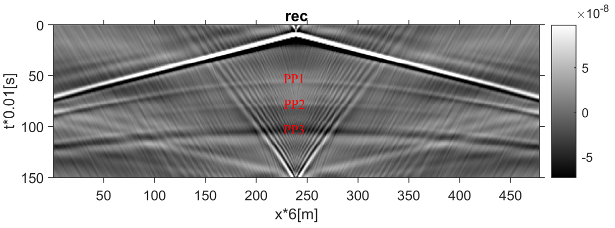

b) Water saturated

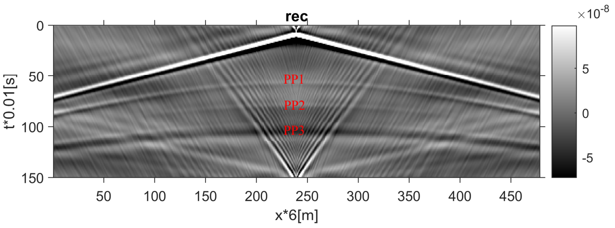

c) CO_2 saturated

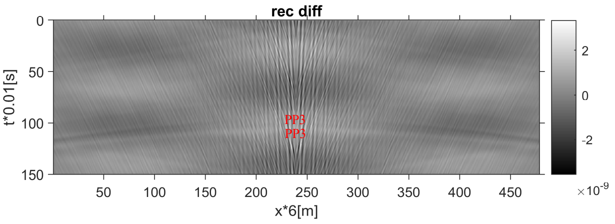

d) difference between water and oil saturation

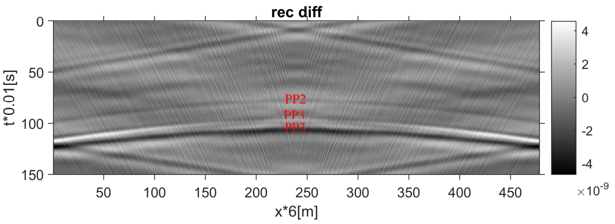

e) difference between CO_2 and oil saturation

Figure 7-4. Synthetic seismograms of the whole model with cracked Block 3 (Model 2, $\phi = 0.0001$) and the difference among them. Labels on the reflections have the meaning, for instance, PP1 for P-down-P-up from the first interface.

8. BISQ theory

In order to compare with porous media modified from Block 3 background, this chapter gives both analytical calculation and numerical simulation based on Biot-squirt (BISQ) mechanism.

BISQ is a mature theory to describe fluid-filled porous media. As mentioned by D. Yang and Zhang (2002), Biot theory is describing through macroscopic rock properties, and the corresponding Biot flow is the flow parallel to the P-wave propagation. Squirt flow is based on the microscopic scale, which is the flow perpendicular to the P-wave propagation. The poroelastic wave equation by D. Yang and Zhang (2002) can describe vertically aligned fractures with horizontally layered media. But it is a system of 5 equations for the 3D case, which makes it highly computationally demanding. Here, a simpler poroelastic wave equation by Parra (1997) is employed, which is a system of 3 equations for 2D VTI background. Though the fracture is not included in Parra's theory, it gives us a fundamental understanding of the difference between Schoenberg (1984) and Biot (Cheng, 2016). In this theory, there are 3 waves travelling in a 2D media (SH-wave is not included), fast-P- and slow-P- propagating in both solid and fluid, SV-wave (later named S-wave) only existing in solid.

This chapter again uses modified isotropic Block 3 as the background. And the porosity for the porous media ϕ is set 0.001.

The wave equation in frequency domain including Biot theory and squirt flow mechanism for VTI media is given by,

$$\begin{gathered}
\left(C_{11}\frac{\partial^2}{\partial x^2}+C_{44}\frac{\partial^2}{\partial z^2}+\omega^2\hat{\rho}_1\right)u_x+(C_{13}+C_{44})\frac{\partial^2 u_z}{\partial x\partial z}-\hat{\alpha}_1\frac{\partial p}{\partial x}=S_x \\
(C_{13}+C_{44})\frac{\partial^2 u_x}{\partial x\partial z}+\left(C_{44}\frac{\partial^2}{\partial x^2}+C_{33}\frac{\partial^2}{\partial z^2}+\omega^2\hat{\rho}_3\right)u_z-\hat{\alpha}_3\frac{\partial p}{\partial x}=S_z \\
-s_3\hat{\alpha}_1\frac{\partial u_x}{\partial x}-s_1\hat{\alpha}_3\frac{\partial u_z}{\partial z}+\left(s_3\theta_1\frac{\partial^2}{\partial x^2}+s_1\theta_3\frac{\partial^2}{\partial z^2}-\beta\right)p=0
\end{gathered}\tag{8.1}$$

and

$$\begin{gathered}
\hat{\alpha}_l = \alpha_l + \omega^2 \rho_f \theta_l \qquad \rho_l = \rho + \omega^2 \rho_f^2 \theta_l \\
\rho = \rho_s(1-\phi) + \phi\rho_f \qquad \theta_l = -\frac{K_l(\omega)}{i\omega} \\
K_l(\omega) = \frac{i\phi}{\omega\rho_f}\left(\frac{\rho_a/\rho_f+\phi}{\phi} + \frac{i\eta_f\phi}{k_l\rho_f\omega}\right)^{-1} \\
\beta = \frac{\phi}{K_f} + \frac{1-\phi}{K_s} - \frac{2(C_{11}+C_{12}+2C_{13})+C_{33}}{9K_s^2} \\
l = 1, 3
\end{gathered} \tag{8.2}$$

where K_f is the fluid bulk modulus; K_s is the grain bulk modulus; η_f is the viscosity of the fluid; ρ_a is the density caused by fluid (Biot, 1956); k is the intrinsic permeability; ρ_s is the grain density; S_x and S_z is the x- and z- component source respectively; p is the pore fluid pressure.

8.1. Dispersion

Here, we study the dispersion of Block 3 saturated by oil and water. Before that, it is necessary to get the formula for phase velocity.

Applying Fourier transform in x- and z- dimensions to the source-free version of (8.1) to get the Christoffel wave equation

$$\begin{pmatrix}
\omega^2\hat{\rho}_1 - C_{11}k_x^2 - C_{44}k_z^2 & -(C_{13}+C_{44})k_xk_z & -i\hat{\alpha}_1k_x \\
-(C_{13}+C_{44})k_xk_z & \omega^2\hat{\rho}_3 - C_{44}k_x^2 - C_{33}k_z^2 & -i\hat{\alpha}_3k_z \\
is_3\hat{\alpha}_1k_x & is_1\hat{\alpha}_3k_z & s_3\theta_1k_x^2 + s_1\theta_3k_z^2 + \beta
\end{pmatrix}
\begin{pmatrix} U_x \\ U_z \\ P \end{pmatrix} = 0 \tag{8.3}$$

The determinant of the first term must be zero as there is a non-zero solution of the second term in (8.3),

$$\det\begin{pmatrix}
\omega^2\widehat{\rho_1} - C_{11}k_x^2 - C_{44}k_z^2 & -(C_{13}+C_{44})k_xk_z & -i\hat{\alpha}_1k_x \\
-(C_{13}+C_{44})k_xk_z & \omega^2\hat{\rho}_3 - C_{44}k_x^2 - C_{33}k_z^2 & -i\hat{\alpha}_3k_z \\
is_3\widehat{\alpha_1}k_x & is_1\hat{\alpha}_3k_z & s_3\theta_1k_x^2 + s_1\theta_3k_z^2 + \beta
\end{pmatrix} = 0 \tag{8.4}$$

Convert k_x and k_z to the combination of v and the incident angle to z-axis θ to form the Christoffel wave equation given in (11.16) in appendix. Then the velocity as a function of incident angle can be computed. (11.16) normally has 3 different absolute velocity solutions, corresponding fast-P-, slow-P- and S-wave.

With the solution k of (11.16), the phase velocity and the attenuation $\frac{1}{Q}$ can be given,

$$\begin{aligned} v &= \frac{\omega}{Real(k)} \\ \frac{1}{Q} &= \frac{2Imag(k)}{Real(k)} \end{aligned} \tag{8.5}$$

To utilize the above theory to isotropic Block 3, some additional parameters for Block 3 are required. The extra physical parameters of Block 3 are given in (Table 8-1).

Table 8-1. Extra parameters of Block 3 for BISQ input. Note: 1-axis is the horizontal axis and 3-axis is the vertical one.

Letter	Value	Description
K_s	$38*10^9\ Pa$	Solid bulk modulus
ρ_s	$2650\ kg/m^3$	Solid density
K_o	$8.64*10^8 Pa$	Oil modulus
η_o	$10^{-1}\ Pa \cdot s$	Oil viscosity
K_w	$2.25*10^9\ Pa$	Water modulus
η_w	$10^{-3}\ Pa \cdot s$	Water viscosity
K_g	$9.6*10^7\ Pa$	CO_2 bulk modulus
η_g	$10^{-5}\ Pa \cdot s$	CO_2 viscosity
k_3	$10^{-15}\ m^2$	Intrinsic permeability along 1-axis
k_3	$10^{-15}\ m^2$	Intrinsic permeability along 3-axis
R_1	$10^{-3}\ m$	Average squirt flow length along 1-axis
R_3	$10^{-3}\ m$	Average squirt flow length along 3-axis
ρ_a	$550\ kg/m^3$	Additional density caused by fluid
ϕ	0.001	Porosity

As the background is isotropic, the effective media is also isotropic after the introducing of the pores. Figure 8-1 is an example of phase velocity and attenuation of oil-saturated Block 3 to show the isotropy of phase velocity and attenuation. So, it is reasonable only to analyze the dispersion vertical wave velocity.

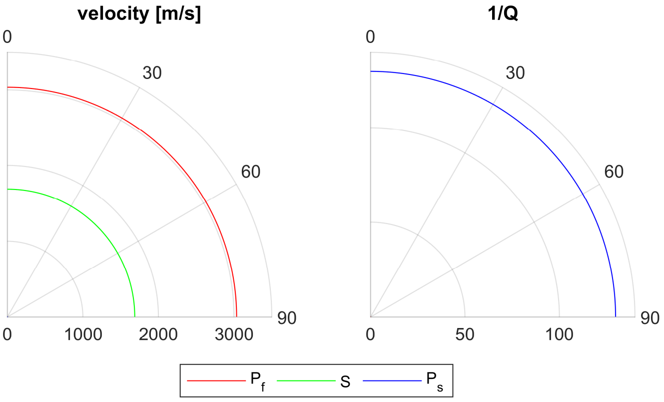

Figure 8-1. Polar plot of phase velocity (left) and attenuation (right) for oil-saturated Block 3 (BISQ theory). P_f for fast-P-wave, S for S-wave and P_s for slow-P-wave. The phase velocity of P_s is too small to be visible.

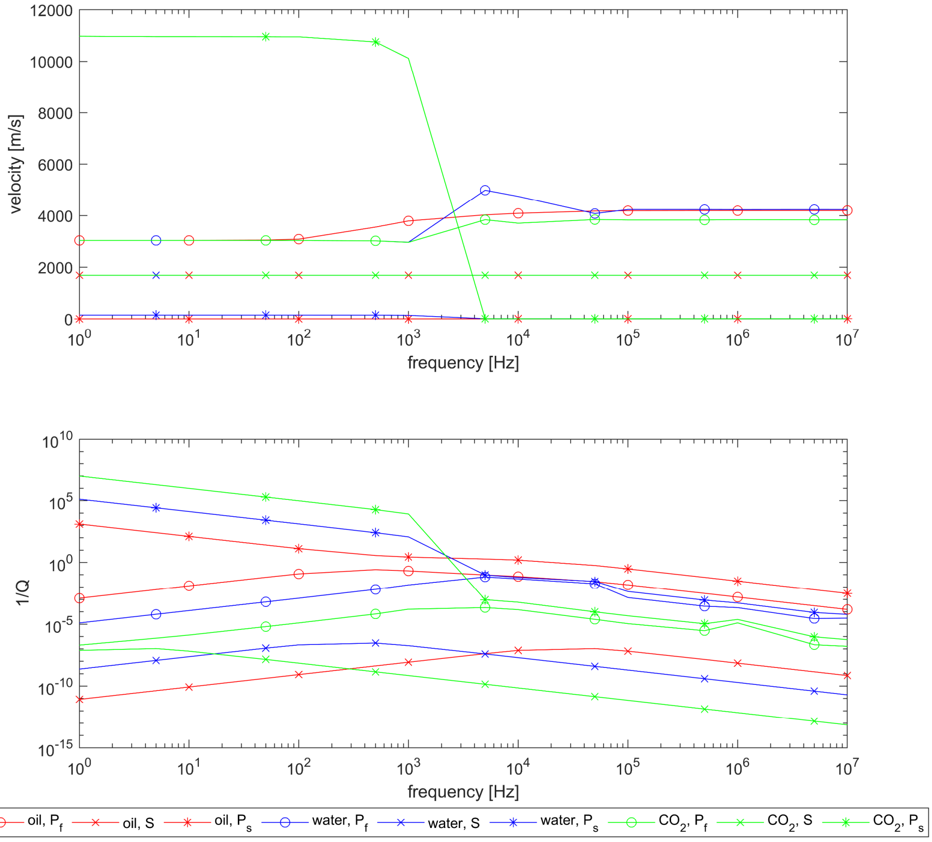

Figure 8-2. Dispersion of oil-, water- and CO2- saturated Block 3 ($\phi = 0.001$, BISQ).

Figure 8-2 gives an overview of the dispersion of the 3 waves with porous Block 3 saturated with 3 different fluids.

Fast-P- and S-wave is weakly dispersive compared to slow-P-wave. And this dispersion is neglectable in the seismic frequency range. Thus, the dispersion of those waves is out of our interest in this study.

It can be noticed that for CO_2 saturation, the velocity of slow-P-wave has a huge velocity with high attenuation under low frequency and the velocity declines rapidly when the frequency reaches to 10^3 Hz. As can be seen from the attenuation magnitude, slow-P-wave is not predicted to be seen on the seismic scale. However, this wave may be observed in Rock physics experiment under high frequency in small scales.

In low-frequency range, fast-P- and S-wave velocities are not much affected by the fluid substitution. As a result, travel time analysis is not an effective tool for us to identify fluid. This is a piece of frustrating news. However, we can still try to explore the reflectivity at the top and bottom of Block 3. This can be seen in seismic simulation as followed.

8.2. Numerical simulation

To implement seismic simulation, some preparation work is needed, i.e., the finite-difference stencil formulation. The finite-difference method in the frequency domain is applied to the poroelastic media (similar to the approach by Q. Yang and Mao (2017)). 11.5 in the appendix gives the process of the finite-difference method. And the corresponding Matlab code is available in 11.6.

As found in Section 8.1, the dispersion for fast-P- and S-wave in seismic frequency (lower than 100 Hz) is weak. As a result, it is sufficient to simulate with a source with a specific dominant frequency. And the source is set z-directional so that the source in x-component is ‘0’. Here, a Ricker wavelet with 10 Hz dominant frequency is selected.

8.2.1. Test for the single reservoir

Firstly, an example is given for the wave propagation in homogenous Block 3 saturated with oil (Figure 8-3). And the corresponding wavefield in time domain is shown in Figure 8-4. In this wavefield, only fast P- and S- wave can be observed. Slow-P-wave vanishes due to the strong attenuation as what is computed in Section 8.1. The wave in the pore pressure field is fast-P-wave, corresponding the fastest wave in solid displacements.

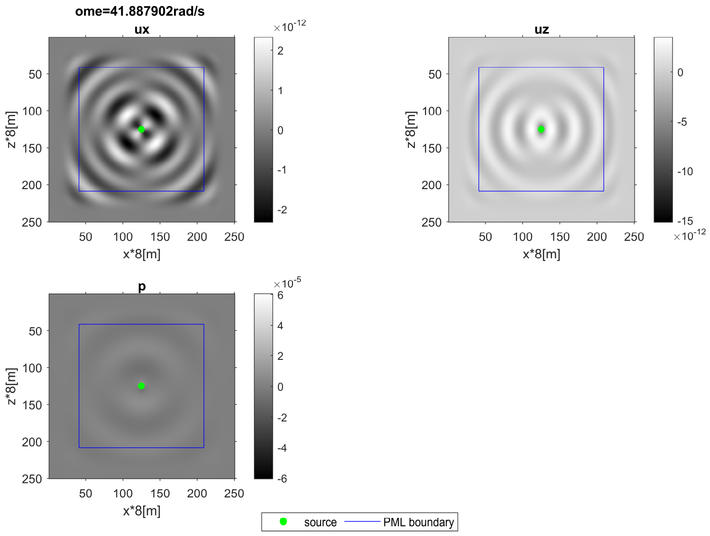

a) $\omega \approx 41.89$ rad/s

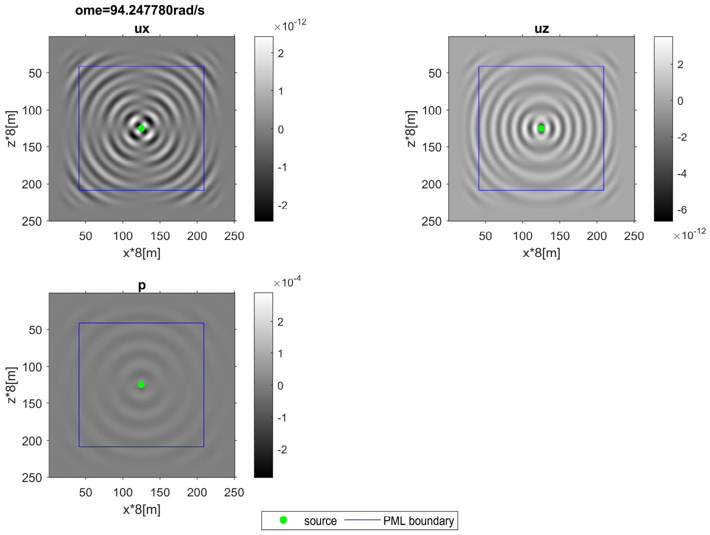

b) $\omega \approx 94.25$ rad/s

Figure 8-3. Wavefield in frequency domain for oil-saturated Block 3 computed with BISQ theory. x-component u_x and z- component u_z and pore pressure p are all displayed, and so on for later figures.

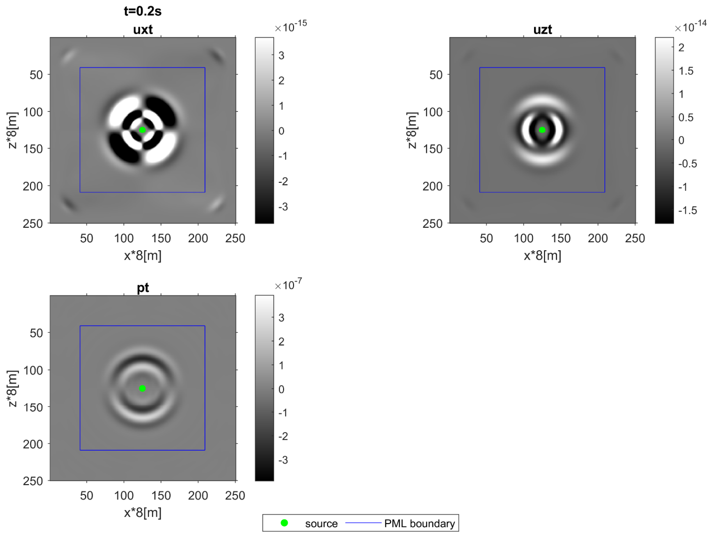

a) t = 0.2 s

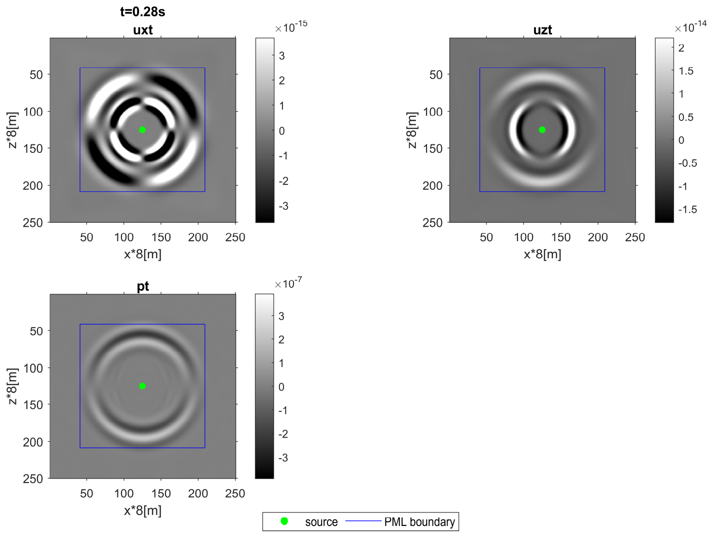

b) t = 0.28 s

Figure 8-4. Wavefield in time domain for oil-saturated Block 3 computed with BISQ.

8.2.2. Results for the whole model

After the testing, the whole model constructed from well log data is then simulated by BISQ theory with porous Block 3 oil-saturated, water-saturated and CO_2-saturated. The blocks other than Block 3 are VTI and can be also simulated with (8.1) by setting the pore effect ‘0’, then (8.1) is identical to VTI wave equation. Table 8-1 gives the input parameters for the simulation. Some other parameters that are not listed in the table are the same as that in previous chapters. There is a line of seismometer located on the top of Block 1. In the end, the recordings of the 3 cases are compared.

One example of time domain wavefield for the whole model with porous Block 3 oil-saturated is shown in Figure 8-5.

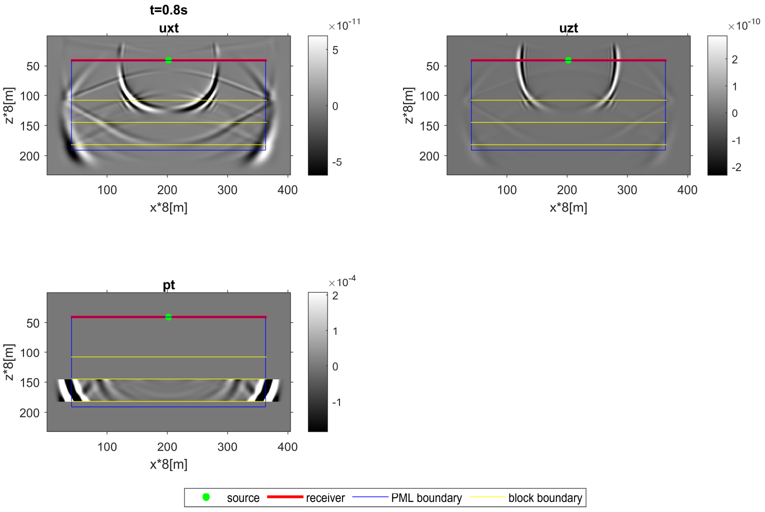

a) t = 0.8 s

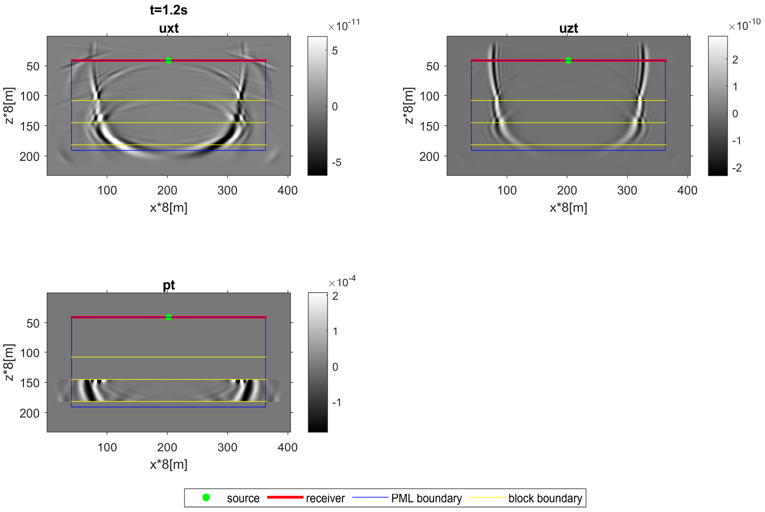

b) t = 1.2 s

Figure 8-5. Wavefield in time domain for the whole model computed with BISQ. Porous Block 3 ($\phi = 0.001$) is oil saturated.

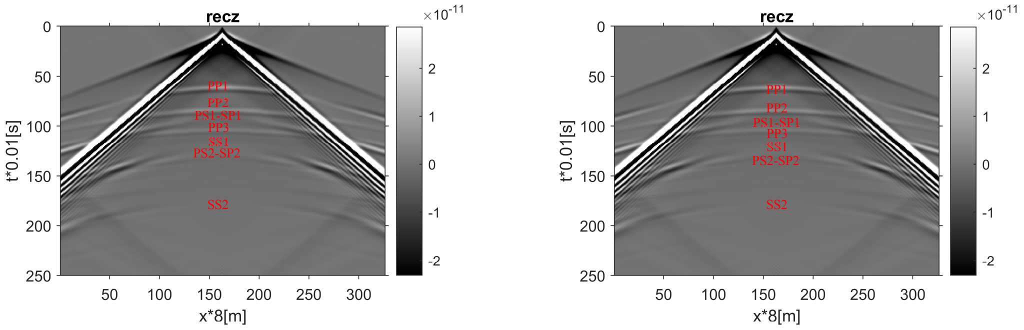

a) Oil

b) Water

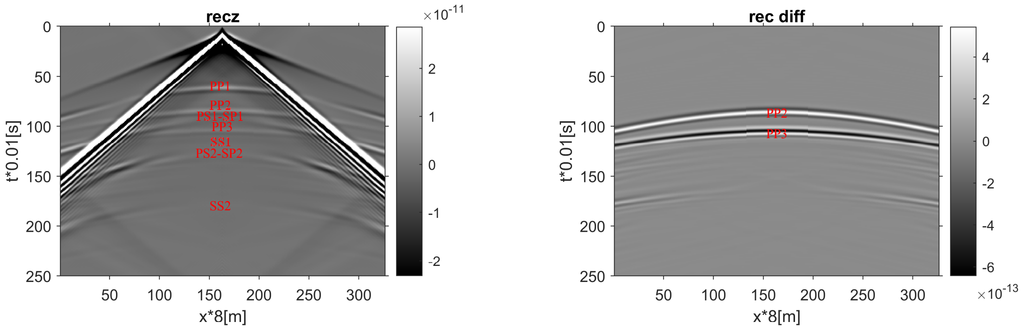

c) CO$_2$

d) Difference between water and oil saturation

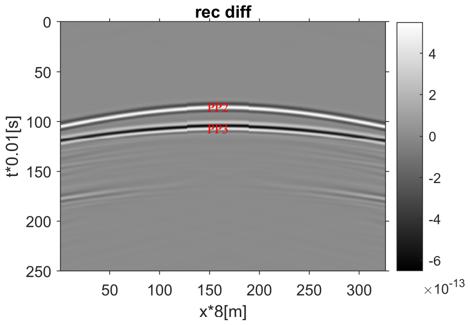

e) Difference between CO$_2$ and oil saturation

Figure 8-6. Synthetic seismic recordings with the receivers on the top of Block 1 computed with BISQ. a) porous Block 3 is saturated with oil; b) porous Block 3 is saturated with water; c) porous Block 3 is saturated with CO$_2$. And their difference d) and e). Labels on the reflections have the meaning, for instance, PS2 for P-down-S-up from the second interface.

The wavefield in time domain (e.g., Figure 8-5) produces the seismic recordings (Figure 8-6), where the seismometers are placed on the top of Block 1. And the differences of the seismograms are also displayed in the figure. Please note that there are also some multiples or the reflection from the boundary, which are not labelled in the figure. PML is not as good as the name ‘perfectly’ that can absorb the energy in the PML region entirely. There are still some reflections from the boundary but the intensity much weaker.

PS and SP reflection should have the same travel time, that is why they are labelled together in Figure 8-6. PP3 is almost superimposed with PS1-SP1 but becomes apparent in the recording differences as PS1-SP1 is cancelled. Similarly, SS1 is just slightly above PS2-SP2, which makes it hard to be discriminated from PS2-SP2 in the original recordings. And SS1 is clear in the recording differences. Figure 8-6 d) and e) contains some multiples or multiple conversions and they are hard to identify, as a result, those are not labelled.

The seismogram difference Figure 8-6 d) and e) shows the reflectivity difference, there is no visible travel time difference under different fluid saturation as has been discussed in Section 8.1. The difference between oil and water saturation is very similar to that between oil and CO_2 saturation. Only PP2 and PP3 events are recognizable on the difference of seismograms. And the amplitude of the difference is ranked moderate compared to the original seismograms.

However, what we have discussed above is the pre-processing seismic sections and they have not gone through true amplitude recovery. The difference caused by the fluid substitution can become stronger if the seismic sections are well processed. Taking into the consideration of noise in the real seismic exploration, the difference of PP2 and PP3 is probably hidden depending on the seismic acquisition and processing technology.

9. Conclusion

The analysis of fluid substitution in alternating solid and fluid layers provides an insight into the possibility of detecting fluid substitution during the water/gas treatment in a horizontally cracked reservoir. Both analytical and numerical methods are applied to our model.

For Model 1 and Model 3, the overall travel time of P/fast-P-wave for gas saturation case is delayed than that under oil/water saturation while it does not change visibly from oil to water saturation. The travel time of P/fast-P-wave for partially saturated oil-CO_2 case changes gradually to longer time as CO_2 displacing oil. And the travel time of SV/slow-P-wave is not very sensitive to fluid substitution. S-wave in cracked Block 3 can be only detected with a large offset, which poses it in the negative position for fluid substitution as normally large offset seismic data is not available. For Model 3 with less void, it is not feasible to detect fluid substitution through travel time analysis.

The P/fast-P reflectivity from Block 2 to Block 3 is studied. Block 2 with Model 1 and Model 3 have almost the same reflectivity features. The reflectivity change from oil saturation to water saturation for Block 2 with Model 1 and Model 3 is ranked moderate, which is still much less significant than that from oil to CO_2 saturation. For Block 2 with Model 2, the reflectivity has an intermediate alteration from oil to CO_2 saturation but this change is so tiny from oil to water.

A conclusion for the consequence of fluid substitution for cracked Block 3 (analytical method) is listed in Table 9-1.

The numerical simulation is only implemented for Model 2 as the result of Model 1/3 has a very low signal to noise ratio. The wavefield for Model 1/3 is much contaminated by the S-wave artefact from the VTI media. The result for Model 2 with overburden and underburden included is consistent with the analytical result. To get the noise-free wavefield, a uniform wave equation is required. And this wave equation should be capable to describe the waves in both VTI media and alternating solid and fluid layers. This wave equation can be obtained through extending the acoustic wave equation for alternating solid and fluid layers based on isotropic background by Schoenberg (1984) to that based on VTI background. And the author will keep on working on this in the future.

The porous Block 3 is also included in this article to see the difference between cracked Block 3 and porous Block 3. The analysis for porous Block 3 with overburden included by BISQ theory shows that there is no apparent travel time change for fluid substitution in Block 3 for such a media. Only the reflectivity on interface 2 and interface 3 alters from one fluid to another in Block 3. This reflectivity change is noticeable in our seismic modelling. And this is different from the model with cracked Block 3 (Model 1), which has some travel time difference with the substitution from oil to CO_2. In addition, horizontally cracked Block 3 is classified as polar anisotropy but porous Block 3 is still isotropic.

Table 9-1. Sign of fluid substitution. Travel time refers to that with overburden included and reflectivity is for the interface between Block 2 and cracked Block 3.

Model	Event	From oil to water	From oil to CO_2
1	P/fast-P travel time	No obvious change	Delay slightly
	SV/slow-P travel time	No obvious change	No obvious change
	P/fast-P reflectivity	Both R_0 and R_2 increase moderately	Both R_0 and R_2 decline dramatically
2	P/fast-P travel time	No obvious change	No obvious change
	SV/slow-P travel time	No obvious change	No obvious change
	P/fast-P reflectivity	No obvious change	Both R_0 and R_2 decline slightly
3	P/fast-P travel time	No obvious change	Delay slightly
	SV/slow-P travel time	No obvious change	No obvious change
	P/fast-P reflectivity	Both R_0 and R_2 increase moderately	Both R_0 and R_2 decline dramatically

10. References

Alkhalifah, T. (2000). An acoustic wave equation for anisotropic media. *Geophysics, 65*, 1239-1250.

Backus, G. E. (1962). Long-wave elastic anisotropy produced by horizontal layering. *Journal of Geophysical Research, 67*(11), 4427-4440.

Biot, M. A. (1956). Theory of propagation of elastic waves in a fluid-saturated porous solid: I. Low-frequency range. *The Journal of the Acoustical Society of America, 28*, 168-178.

Bos, L., Dalton, D. R., Slawinski, M. A., & Stanoev, T. (2016). On Backus average for generally anisotropic layers. *Journal of Elasticity*, 1-18.

Burnley, P. (2019, March 13, 2019). Tensors: Stress, strain and elasticity. Retrieved from https://serc.carleton.edu/NAGTWorkshops/mineralogy/mineral_physics/tensors.html

Cheng, A. H.-D. (2016). *Poroelasticity*. Switzerland: Springer Nature.

Collino, F., & Tsogka, C. (2001). Application of the PML absorbing layer model to the linear elastodynamic problem in anisotropic heterogeneous media. *Geophysics, 66*, 294-307.

Dvorkin, J., & Nur, A. (1993). Dynamic poroelasticity: A unified model with the squirt and the Biot mechanisms. *Geophysics, 58*.

Engquist, B., & Majda, A. (2010). Absorbing boundary conditions for the numerical simulation of waves. *Mathematics of Computation, 31*, 629-651.

Gao, Y., Zhang, J., & Yao, Z. (2015). Unsplit complex frequency shifted perfectly matched layer for second-order wave equation using auxiliary differential equations. *J Acoust Soc Am, 138*(6), EL551-557.

Gilbert, F., & Backus, G. E. (1966). Propagator matrices in elastic wave and vibration problems. *Geophysics, 2*, 326-332.

Hongjuan, Q., & Guangming, Z. (2012). *Numerical Simulation of Seismic Source Based on Staggered-Grid Finite Difference Method*. Paper presented at the 2012

International Conference on Computer Science and Electronics Engineering.

Jamali Hondori, E., Mikada, H., Goto, T. N., & Takekawa, J. (2013). *A MATLAB Package for Frequency Domain Modeling of Elastic Waves*. Paper presented at the London 2013, 75th eage conference en exhibition incorporating SPE Europec.

Kennett, B. (2009). *Seismic wave propagation in stratified media* (second ed.): ANU E Press.

Kim, D. (2019). A Modified PML Acoustic Wave Equation. *Symmetry, 11*(2).

Komatitsch, D., & Martin, R. (2007). An unsplit convolutional perfectly matched layer improved at grazing incidence for the seismic wave equation. *Geophysics, 72*(5), SM155-SM167.

Kumar, D. (2013). Applying Backus averaging for deriving seismic anisotropy of a long-wavelength equivalent medium from well-log data. *Journal of Geophysics and Engineering, 10*(5).

Masson, Y. J., Pride, S. R., & Nihei, K. T. (2006). Finite difference modeling of Biot's poroelastic equations at seismic frequencies. *Journal of Geophysical Research, 111*(B10).

Oh, G. L., & Brunskog, J. (2014). Investigation of model based beamforming and Bayesian inversion signal processing methods for seismic localization of underground sources. *The Journal of the Acoustical Society of America, 136*(2), 705-714.

Parra, J. O. (1997). The transversely isotropic poroelastic wave equation including the Biot and the squirt mechanisms: Theory and application. *Geophysics, 62*, 309-318.

Schoenberg, M. (1984). Wave propagation in alternating solid and fluid layers. *Wave Motion, 6*, 303-320.

Schoenberg, M., & Douma, J. (1988). Elastic wave propagation in media with parallel fractures and aligned cracks. *Geophysical Prospecting, 36*, 571-590.

Schoenberg, M., & Muirt, F. (1989). A calculus for finely layered anisotropic media.

Geophysics, 54, 581-589.

Schoenberg, M., & Sayers, C. M. (1995). Seismic anisotropy of fractured rock. *Geophysics, 60*, 204-211.

Sil, S., Sen, M. K., & Gurevich, B. (2011). Analysis of fluid substitution in a porous and fractured medium. *Geophysics, 76*, 157-166.

Simm, R., & Bacon, M. (2014). *Seismic amplitude: an interpreter's handbook*: Cambridge.

Souza, A. A. V. B., Bulcão, A., Dias, B. P., Filho, D. M. S., Farias, F. F., Alves, G. C., . . . Loureiro, F. P. (2013). *2D frequency domain finite-difference elastic-wave modeling*. Paper presented at the 13th International Congress of the Brazilian Geophysical Society & EXPOGEF, Rio de Janeiro, Brazil, 26–29 August 2013.

Stovas, A., & Landrø, M. (2004). Optimal use of PP and PS time-lapse stacks for fluid–pressure discrimination. *Geophysical Prospecting, 52*, 301-312.

Stovas, A., & Roganov, Y. (2017). Waves in periodically layered solid-fluid system. *4th International Workshop on Rock Physics*.

Thomsen, L. (1986). Weak elastic anisotropy. *Geophysics, 51*(10), 1954-1966.

Thomsen, L. (2002). *Understanding seismic anisotropy in exploration and exploitation* (2nd ed.): Society of Exploration Geophysicists.

Tsvankin, I. (2012). *Seismic signatures and analysis of reflection data in anisotropic media*. United States of America: Society of Exploration Geophysicists.

Yang, D., & Zhang, Z. (2002). Poroelastic wave equation including the Biot/squirt mechanism and the solid/fluid coupling anisotropy. *Wave Motion, 35*, 223-245.

Yang, Q., & Mao, W. (2017). Simulation of seismic wave propagation in 2-D poroelastic media using weighted-averaging finite difference stencils in the frequency–space domain. *Geophysical Journal International, 208*(1), 148-161.

Zhang, W., & Shen, Y. (2010). Unsplit complex frequency-shifted PML implementation using auxiliary differential equations for seismic wave modeling. *Geophysics, 75*(4), T141-T154.

Zhou, J. J., Wang, D. L., & Feng, F. (2014). *Elastic Constants Calculation Method and Propagation Properties for Cracked Shale Media*. Paper presented at the Proceedings 76th EAGE Conference and Exhibition 2014.

11. Appendices

11.1. Full expression of q for alternating layers

$$
\begin{aligned}
&\mathrm{q{=}acos(cosh((H}\,\omega\phi(p^2v_{pf}^2-1)^{(1/2)})/v_{pf})(exp(-(H\omega(pv_p-1)^{(1/2)}(pv_p+1)^{(1/2)}(\phi-1))/v_p)/2-\\
&exp((H\omega(pv_p-1)^{(1/2)}(pv_p+1)^{(1/2)}(\phi-1))/v_p)/2+exp((H\omega(pv_s-1)^{(1/2)}(pv_s+1)^{(1/2)}(\phi-\\
&1))/v_s)-p^2v_s^2exp(-(H\omega(pv_p-1)^{(1/2)}(pv_p+1)^{(1/2)}(\phi-1))/v_p)+p^2v_s^2exp(-(H\omega(pv_s-\\
&1)^{(1/2)}(pv_s+1)^{(1/2)}(\phi-1))/v_s)-(exp((H\omega(pv_p-1)^{(1/2)}(pv_p+1)^{(1/2)}(\phi-1))/v_p)-exp((H\omega(pv_s-\\
&1)^{(1/2)}(pv_s+1)^{(1/2)}(\phi-1))/v_s))(pv_s-1)(pv_s+1)+(\omega p\rho v_s^2exp(-(H\omega(v_p(p^2v_s^2-1)^{(1/2)}+\\
&v_s(p^2v_p^2-1)^{(1/2)})(\phi-1))/(v_pv_s))(2p^2v_s^2-1)(exp((H\omega(pv_p-1)^{(1/2)}(pv_p+1)^{(1/2)}(\phi-1))/v_p)-\\
&exp((H\omega(pv_s-1)^{(1/2)}(pv_s+1)^{(1/2)}(\phi-1))/v_s)-exp((H\omega(v_p(p^2v_s^2-1)^{(1/2)}+2v_s(p^2v_p^2-\\
&1)^{(1/2)})(\phi-1))/(v_pv_s))+exp((H\omega(2v_p(p^2v_s^2-1)^{(1/2)}+v_s(p^2v_p^2-1)^{(1/2)})(\phi-1))/(v_pv_s)))(2p^3v_s^4exp((H\omega(pv_p\text{-}\\
&1)^{(1/2)}(pv_p+1)^{(1/2)}(\phi-1))/v_p)(pv_p-1)^{(1/2)}(pv_p+1)^{(1/2)}-2p^3v_s^4exp(-(H\omega(pv_p-1)^{(1/2)}(pv_p+\\
&1)^{(1/2)}(\phi-1))/v_p)(pv_p-1)^{(1/2)}(pv_p+1)^{(1/2)}-2pv_s^2exp((H\omega(pv_p-1)^{(1/2)}(pv_p+1)^{(1/2)}(\phi-\\
&1))/v_p)(pv_p-1)^{(1/2)}(pv_p+1)^{(1/2)}+2pv_s^2exp(-(H\omega(pv_p-1)^{(1/2)}(pv_p+1)^{(1/2)}(\phi-1))/v_p)(pv_p-\\
&1)^{(1/2)}(pv_p+1)^{(1/2)}-pv_pv_sexp((H\omega(pv_s-1)^{(1/2)}(pv_s+1)^{(1/2)}(\phi-1))/v_s)(pv_s-1)^{(1/2)}(pv_s+\\
&1)^{(1/2)}+pv_pv_sexp(-(H\omega(pv_s-1)^{(1/2)}(pv_s+1)^{(1/2)}(\phi-1))/v_s)(pv_s-1)^{(1/2)}(pv_s+1)^{(1/2)}-\\
&2pv_pv_sexp((H\omega(pv_s-1)^{(1/2)}(pv_s+1)^{(1/2)}(\phi-1))/v_s)(pv_s-1)^{(3/2)}(pv_s+1)^{(3/2)}+2pv_pv_sexp(-(H\omega(pv_s-\\
&1)^{(1/2)}(pv_s+1)^{(1/2)}(\phi-1))/v_s)(pv_s-1)^{(3/2)}(pv_s+1)^{(3/2)}))/(4\omega p^2\rho v_s^4exp((H\omega(pv_p-1)^{(1/2)}(pv_p+\\
&1)^{(1/2)}(\phi-1))/v_p)(pv_p-1)^{(1/2)}(pv_p+1)^{(1/2)}-4\omega p^2\rho v_s^4exp(-(H\omega(pv_p-1)^{(1/2)}(pv_p+1)^{(1/2)}(\phi-\\
&1))/v_p)(pv_p-1)^{(1/2)}(pv_p+1)^{(1/2)}-4\omega p^4\rho v_s^6exp((H\omega(pv_p-1)^{(1/2)}(pv_p+1)^{(1/2)}(\phi-1))/v_p)(pv_p-\\
&1)^{(1/2)}(pv_p+1)^{(1/2)}+4\omega p^4\rho v_s^6exp(-(H\omega(pv_p-1)^{(1/2)}(pv_p+1)^{(1/2)}(\phi-1))/v_p)(pv_p-1)^{(1/2)}(pv_p+\\
&1)^{(1/2)}+\omega\rho v_pv_sexp((H\omega(pv_s-1)^{(1/2)}(pv_s+1)^{(1/2)}(\phi-1))/v_s)(pv_s-1)^{(1/2)}(pv_s+1)^{(1/2)}-\\
&\omega\rho v_pv_sexp(-(H\omega(pv_s-1)^{(1/2)}(pv_s+1)^{(1/2)}(\phi-1))/v_s)(pv_s-1)^{(1/2)}(pv_s+1)^{(1/2)}+4\omega\rho v_pv_sexp((H\omega(pv_s-\\
&1)^{(1/2)}(pv_s+1)^{(1/2)}(\phi-1))/v_s)(pv_s-1)^{(3/2)}(pv_s+1)^{(3/2)}-4\omega\rho v_pv_sexp(-(H\omega(pv_s-1)^{(1/2)}(pv_s+\\
&1)^{(1/2)}(\phi-1))/v_s)(pv_s-1)^{(3/2)}(pv_s+1)^{(3/2)}+4\omega\rho v_pv_sexp((H\omega(pv_s-1)^{(1/2)}(pv_s+1)^{(1/2)}(\phi-\\
&1))/v_s)(pv_s-1)^{(5/2)}(pv_s+1)^{(5/2)}-4\omega\rho v_pv_sexp(-(H\omega(pv_s-1)^{(1/2)}(pv_s+1)^{(1/2)}(\phi-1))/v_s)(pv_s-\\
&1)^{(5/2)}(pv_s+1)^{(5/2)}))-(sinh((H\omega\phi(p^2v_{pf}^2-1)^{(1/2)})/v_{pf})(p^2v_{pf}^2-1)^{(1/2)}((\omega\rho v_pexp((H\omega(pv_p-\\
&1)^{(1/2)}(pv_p+1)^{(1/2)}(\phi-1))/v_p)(pv_s-1)^{(1/2)}(pv_s+1)^{(1/2)}-\omega\rho v_pexp(-(H\omega(pv_p-1)^{(1/2)}(pv_p+\\
&1)^{(1/2)}(\phi-1))/v_p)(pv_s-1)^{(1/2)}(pv_s+1)^{(1/2)}+4\omega\rho v_pexp((H\omega(pv_p-1)^{(1/2)}(pv_p+1)^{(1/2)}(\phi-\\
&1))/v_p)(pv_s-1)^{(3/2)}(pv_s+1)^{(3/2)}-4\omega\rho v_pexp(-(H\omega(pv_p-1)^{(1/2)}(pv_p+1)^{(1/2)}(\phi-1))/v_p)(pv_s-\\
&1)^{(3/2)}(pv_s+1)^{(3/2)}+4\omega\rho v_pexp((H\omega(pv_p-1)^{(1/2)}(pv_p+1)^{(1/2)}(\phi-1))/v_p)(pv_s-1)^{(5/2)}(pv_s+\\
&1)^{(5/2)}-4\omega\rho v_pexp(-(H\omega(pv_p-1)^{(1/2)}(pv_p+1)^{(1/2)}(\phi-1))/v_p)(pv_s-1)^{(5/2)}(pv_s+1)^{(5/2)}+\\
&4\omega p^2\rho v_s^3exp((H\omega(pv_s-1)^{(1/2)}(pv_s+1)^{(1/2)}(\phi-1))/v_s)(pv_p-1)^{(1/2)}(pv_p+1)^{(1/2)}-4\omega p^2\rho v_s^3exp(-(H\omega(pv_s-\\
&1)^{(1/2)}(pv_s+1)^{(1/2)}(\phi-1))/v_s)(pv_p-1)^{(1/2)}(pv_p+1)^{(1/2)}-4\omega p^4\rho v_s^5exp((H\omega(pv_s-1)^{(1/2)}(pv_s+\\
&1)^{(1/2)}(\phi-1))/v_s)(pv_p-1)^{(1/2)}(pv_p+1)^{(1/2)}+4\omega p^4\rho v_s^5exp(-(H\omega(pv_s-1)^{(1/2)}(pv_s+1)^{(1/2)}(\phi-\\
&1))/v_s)(pv_p-1)^{(1/2)}(pv_p+1)^{(1/2)})/(2(pv_p-1)^{(1/2)}(pv_p+1)^{(1/2)}(pv_s-1)^{(1/2)}(pv_s+1)^{(1/2)})+\\
&(2\omega^2p^2\rho^2v_pv_s^4exp(-(2H\omega(v_p(p^2v_s^2-1)^{(1/2)}+v_s(p^2v_p^2-1)^{(1/2)})(\phi-1))/(v_pv_s))(p^2v_s^2-1)(2p^2v_s^2-\\
&1)^2(exp((H\omega(pv_p-1)^{(1/2)}(pv_p+1)^{(1/2)}(\phi-1))/v_p)-exp((H\omega(pv_s-1)^{(1/2)}(pv_s+1)^{(1/2)}(\phi-\\
&1))/v_s)-exp((H\omega(v_p(p^2v_s^2-1)^{(1/2)}+2v_s(p^2v_p^2-1)^{(1/2)})(\phi-1))/(v_pv_s))+exp((H\omega(2v_p(p^2v_s^2-\\
&1)^{(1/2)}+v_s(p^2v_p^2-1)^{(1/2)})(\phi-1))/(v_pv_s)))^2)/(4\omega p^2\rho v_s^4exp((H\omega(pv_p-1)^{(1/2)}(pv_p+1)^{(1/2)}(\phi-\\
&1))/v_p)(pv_p-1)^{(1/2)}(pv_p+1)^{(1/2)}-4\omega p^2\rho v_s^4exp(-(H\omega(pv_p-1)^{(1/2)}(pv_p+1)^{(1/2)}(\phi-1))/v_p)(pv_p-\\
&1)^{(1/2)}(pv_p+1)^{(1/2)}-4\omega p^4\rho v_s^6exp((H\omega(pv_p-1)^{(1/2)}(pv_p+1)^{(1/2)}(\phi-1))/v_p)(pv_p-1)^{(1/2)}(pv_p+\\
&1)^{(1/2)}+4\omega p^4\rho v_s^6exp(-(H\omega(pv_p-1)^{(1/2)}(pv_p+1)^{(1/2)}(\phi-1))/v_p)(pv_p-1)^{(1/2)}(pv_p+1)^{(1/2)}+\\
&\omega\rho v_pv_sexp((H\omega(pv_s-1)^{(1/2)}(pv_s+1)^{(1/2)}(\phi-1))/v_s)(pv_s-1)^{(1/2)}(pv_s+1)^{(1/2)}-\omega\rho v_pv_sexp(-(H\omega(pv_s-\\
&1)^{(1/2)}(pv_s+1)^{(1/2)}(\phi-1))/v_s)(pv_s-1)^{(1/2)}(pv_s+1)^{(1/2)}+4\omega\rho v_pv_sexp((H\omega(pv_s-1)^{(1/2)}(pv_s+\\
&1)^{(1/2)}(\phi-1))/v_s)(pv_s-1)^{(3/2)}(pv_s+1)^{(3/2)}-4\omega\rho v_pv_sexp(-(H\omega(pv_s-1)^{(1/2)}(pv_s+1)^{(1/2)}(\phi-\\
&1))/v_s)(pv_s-1)^{(3/2)}(pv_s+1)^{(3/2)}+4\omega\rho v_pv_sexp((H\omega(pv_s-1)^{(1/2)}(pv_s+1)^{(1/2)}(\phi-1))/v_s)(pv_s-\\
&1)^{(5/2)}(pv_s+1)^{(5/2)}-4\omega\rho v_pv_sexp(-(H\omega(pv_s-1)^{(1/2)}(pv_s+1)^{(1/2)}(\phi-1))/v_s)(pv_s-1)^{(5/2)}(pv_s+\\
&1)^{(5/2)})))/(2\omega\rho fv_{pf})+(\rho fv_{pf}sinh((H\omega\phi(p^2v_{pf}^2-1)^{(1/2)})/v_{pf})(exp((2H\omega(pv_p-1)^{(1/2)}(pv_p+\\
&1)^{(1/2)}(\phi-1))/v_p)-1)(exp((2H\omega(pv_s-1)^{(1/2)}(pv_s+1)^{(1/2)}(\phi-1))/v_s)-1)(pv_p-1)^{(1/2)}(pv_p+\\
&1)^{(1/2)}(pv_s-1)^{(1/2)}(pv_s+1)^{(1/2)})/(4\rho(pv_{pf}-1)^{(1/2)}(pv_{pf}+1)^{(1/2)}(v_pexp((H\omega(pv_p-1)^{(1/2)}(pv_p+\\
&1)^{(1/2)}(\phi-1))/v_p)(pv_s-1)^{(1/2)}(pv_s+1)^{(1/2)}+4v_pexp((H\omega(pv_p-1)^{(1/2)}(pv_p+1)^{(1/2)}(\phi-\\
&1))/v_p)(pv_s-1)^{(3/2)}(pv_s+1)^{(3/2)}+4v_pexp((H\omega(pv_p-1)^{(1/2)}(pv_p+1)^{(1/2)}(\phi-1))/v_p)(pv_s-\\
&1)^{(5/2)}(pv_s+1)^{(5/2)}-v_pexp((H\omega(2v_p(p^2v_s^2-1)^{(1/2)}+v_s(p^2v_p^2-1)^{(1/2)})(\phi-1))/(v_pv_s))(pv_s-\\
&1)^{(1/2)}(pv_s+1)^{(1/2)}-4v_pexp((H\omega(2v_p(p^2v_s^2-1)^{(1/2)}+v_s(p^2v_p^2-1)^{(1/2)})(\phi-1))/(v_pv_s))(pv_s-\\
&1)^{(3/2)}(pv_s+1)^{(3/2)}-4v_pexp((H\omega(2v_p(p^2v_s^2-1)^{(1/2)}+v_s(p^2v_p^2-1)^{(1/2)})(\phi-1))/(v_pv_s))(pv_s-\\
&1)^{(5/2)}(pv_s+1)^{(5/2)}+4p^2v_s^3exp((H\omega(pv_s-1)^{(1/2)}(pv_s+1)^{(1/2)}(\phi-1))/v_s)(pv_p-1)^{(1/2)}(pv_p+\\
&1)^{(1/2)}-4p^4v_s^5exp((H\omega(pv_s-1)^{(1/2)}(pv_s+1)^{(1/2)}(\phi-1))/v_s)(pv_p-1)^{(1/2)}(pv_p+1)^{(1/2)}-\\
&4p^2v_s^3exp((H\omega(v_p(p^2v_s^2-1)^{(1/2)}+2v_s(p^2v_p^2-1)^{(1/2)})(\phi-1))/(v_pv_s))(pv_p-1)^{(1/2)}(pv_p+\\
&1)^{(1/2)}+4p^4v_s^5exp((H\omega(v_p(p^2v_s^2-1)^{(1/2)}+2v_s(p^2v_p^2-1)^{(1/2)})(\phi-1))/(v_pv_s))(pv_p-1)^{(1/2)}(pv_p+\\
&1)^{(1/2)})))/(H\omega)
\end{aligned}
\tag{11.1}
$$

11.2.Information on the 4 blocks

Table 11-1. Information on the 4 blocks from well log data. ‘a’ of ‘3’ means the original Block 3 and ‘b’ stands for the isotropic Block 3.

Block	1	2	3		4
			a	b	
Start depth $[m]$	452.8	1000.0	1300.0	1300.0	1600.0
End depth $[m]$	1000.0	1300.0	1600.0	1600.0	2199.3
$\rho\,[kg/m^3]$	2173.5	2408.5	2248.6	2248.6	2379.7
$C_{11}*10^{10}\,[Pa]$	1.1873	2.1749	2.2826	2.4381	3.3636
$C_{13}*10^{10}\,[Pa]$	0.6674	1.0960	0.8849	0.9316	1.2257
$C_{33}*10^{10}\,[Pa]$	1.1676	1.7532	2.4381	2.4318	2.9456
$C_{44}*10^{10}\,[Pa]$	0.2410	0.3517	0.7532	0.7532	0.8909
$C_{66}*10^{10}\,[Pa]$	0.2554	0.4899	0.6886	0.7532	1.0629
$v_{p0}*10^3\,[m/s]$	2317.7	2698.0	3292.8	3292.8	3518.2
$v_{s0}*10^3\,[m/s]$	1053.1	1208.4	1830.2	1830.2	1934.9
ϵ	0.0084	0.1202	-0.0319	0	0.071
δ	-0.0154	0.0268	-0.0189	0	0.0214
γ	0.0298	0.1965	-0.0429	0	0.0965

11.3.Numerical simulation for cracked reservoir with overburden included

11.3.1. Perfectly matched layer

The conventional fixed boundary is simple to execute. However, to avoid the reflection coming to the effective model region, there is a demand to increase the computation region, which is costly in computation.

PML is a method to introduce complex part into the wave equation to attenuate the energy gradually layer by layer closing to the boundaries (Gao, Zhang, & Yao, 2015; Kim, 2019; Zhang & Shen, 2010). It was originally used for Maxwell’s equations. But the idea can be easily applied to any other wave equations.

It is true that ABC can help to absorb the energy going to the boundary but it only works well for isotropic media. There is still a lot of reflection from boundaries if only ABC is applied without PML (e.g., Figure 11-1 a)). With the introducing of PML, not only the reflection from the boundaries can be suppressed, but the noise in the field can be also reduced (Figure 11-1 b)).

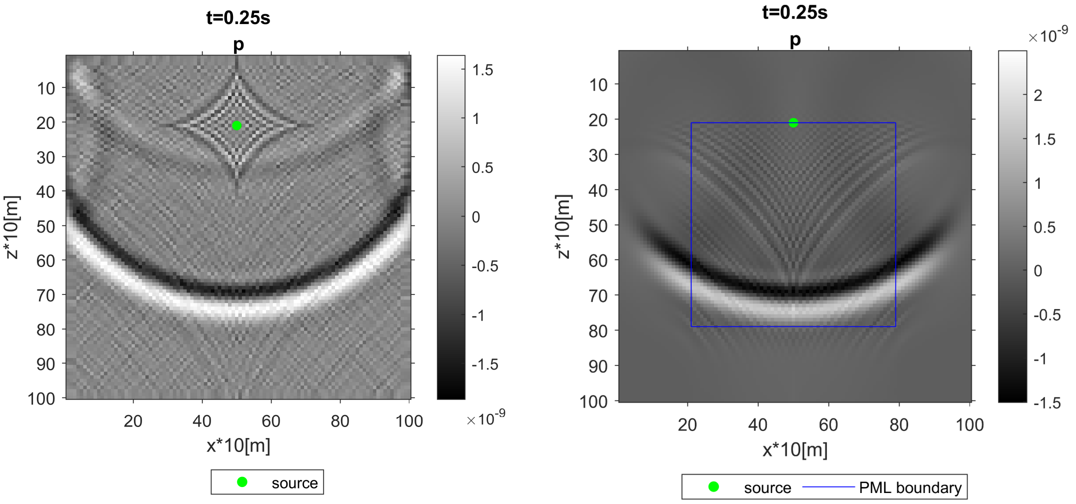

a) without PML

b) with PML

Figure 11-1. Acoustic wavefield in time domain converted from the frequency domain finite-difference method. The snapshots in time domain were taken at 0.25 s for a source located in homogenous Block 2 a) without PML and b) with PML. The boundary condition is ABC. S-wave artefact emerges here. Apparent reflection can be seen from the top boundaries in a).

Following the work by Komatitsch and Martin (2007), PML transform is given by

$$
\begin{gathered}
\partial x \to g_x \partial x \\
\partial z \to g_z \partial z \\
g_x = 1 + \frac{d_x}{i\omega} \\
g_z = 1 + \frac{d_z}{i\omega} \\
d_x = \begin{cases} d_0 (\frac{x}{L})^2 & x \ in \ PML \ region \\ 0 & else \end{cases} \\
d_z = \begin{cases} d_0 (\frac{z}{L})^2 & z \ in \ PML \ region \\ 0 & else \end{cases} \\
d_0 = -3 v_p \log(R_c) / (2L)
\end{gathered}
\tag{11.2}
$$

where x and z is the distance to the inner boundary of PML; L is the thickness of the PML layer; v_p is the estimated P-wave velocity; R_c is the theoretical reflection coefficient proposed by Collino and Tsogka (2001).

To make PML applied in inhomogeneous media v_p is given in grid form for different

v_p at different locations.

An illustration for distributions of d_x and d_z are given in Figure 11-2.

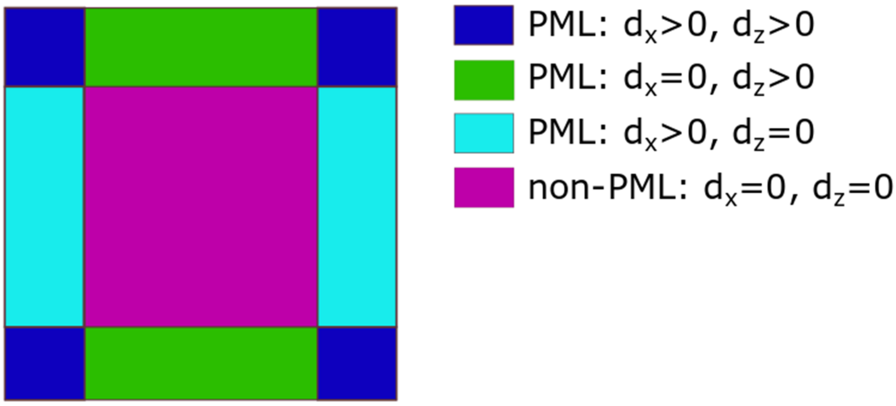

Figure 11-2. A sketch of PML layers explaining the value distribution of d_x and d_z.

And now we apply PML transform to (7.2) and (7.5) according to (11.2),

$$\begin{aligned} -\omega^2 P &= \frac{(1+2\eta)v^2}{g_x^2}\frac{\partial^2 P}{\partial x^2}+\frac{v_v^2}{g_z^2}\frac{\partial^2 P}{\partial z^2}+\frac{2\eta v^2 v_v^2}{\omega^2 g_x^2 g_z^2}\frac{\partial^4 P}{\partial x^2}\partial z^2 \\ &(-\omega^2 v_{pl}^{-2}-\frac{\partial^2}{g_x^2\partial x^2})\left(\frac{1}{\langle\rho\rangle}\frac{\partial^2 P}{g_z^2\partial z^2}+\frac{1}{\langle\rho\rangle}\frac{\partial^2 P}{g_x^2\partial x^2}+\langle\frac{1}{\rho v_p^2}\rangle\omega^2 P\right) \\ &=\frac{\phi}{\rho}(-\frac{\omega^2}{{v_p}^2}-\frac{\partial^2}{g_x^2\partial x^2})\frac{\partial^2 P}{g_x^2\partial x^2} \end{aligned} \tag{11.3}$$

In order to simplify computation, (11.3) is formulated under weak variation approximation, e.g.,

$$\frac{\partial^2}{\partial x^2}\to\frac{1}{g_x}\frac{\partial}{\partial x}(\frac{1}{g_x}\frac{\partial}{\partial x})\approx\frac{1}{g_x^2}\frac{\partial^2}{\partial x^2} \tag{11.4}$$

and same for z-dimension. Otherwise, the 4th order differentiation makes the equations too complex to discretize later. (11.4) is tested and the difference between the 2nd term and the 3rd term in our problem is no bigger than 0.1% when there are 40 layers of PML.

11.3.2. Discretization

To utilize the finite-difference method, we need to discretize (11.3). Firstly let us recall finite-difference stencil for first, second, fourth order for a function $f(x,z)$

$$\begin{gathered}
first\ order: \frac{\partial f}{\partial x} \approx \frac{f(x+h,z)-f(x-h,z)}{2h} \\
second\ order: \frac{\partial^2 f}{\partial x^2} \approx \frac{f(x+h,z)-2f(x,z)+f(x-h,z)}{h^2} \\
second\ order: \frac{\partial^2 f}{\partial x \partial z} \\
\approx \begin{pmatrix} f(x+h,z+h)-f(x+h,z-h) \\ -f(x-h,z+h)+f(x-h,z-h) \end{pmatrix} / (4h^2) \\
fourth\ order: \frac{\partial^4 f}{\partial x^2 \partial z^2} \\
\approx \begin{bmatrix} 4f(x,z)-2(f(x-h,z)+f(x,z-h) \\ +f(x+h,z)+f(x,z+h)+f(x-h,z-h) \\ +f(x+h,z-h)+f(x+h,z+h)+f(x-h,z+h)) \end{bmatrix} / h^4 \\
fourth\ order: \frac{\partial^4 f}{\partial x^4} \\
\approx \begin{pmatrix} f(x+2h,z)-4f(x+h,z) \\ +6f(x,z)-4f(x-h,z) \\ +f(x-2h,z) \end{pmatrix} / h^4
\end{gathered} \tag{11.5}$$

where h is the step length in the spatial domain.

If we consider x is the j-th column grid and z is the i-th row, then the grid in x- and z-directions can be expressed as

$$\begin{gathered} x+h \to j+1 \\ z+h \to i+1 \end{gathered} \tag{11.6}$$

and so on for $x-h$, $x+2h$, $x-2h$, $z-h$...

where h is the spatial step length.

Firstly, we apply the transform of (11.5) with weak variation approximation to wave equations after PML transform (11.3),

$$
\begin{aligned}
&E_1(P(x+h,z,\omega)-2P(x,z,\omega)+P(x-h,z,\omega))/h^2\\
&+E_2(P(x,z+h,\omega)-2P(x,z,\omega)+P(x,z-h,\omega))/h^2\\
&+E_3(4P(x,z,\omega)-2(P(x-h,z,\omega)+P(x,z-h,\omega)\\
&+P(x+h,z,\omega)+P(x,z+h,\omega)+P(x-h,z-h,\omega)\\
&+P(x+h,z-h,\omega)+P(x+h,z+h,\omega)+P(x-h,z+h,\omega))/h^4\\
&+\omega^2P(x,z)=-S(x,z,\omega)
\end{aligned}
$$

$$E_1=\frac{(1+2\eta_v^2)}{g_x^2}$$

$$E_2=\frac{v_v^2}{g_z^2}$$

$$E_3=\frac{2\eta v^2 v_v^2}{\omega^2 g_x^2 g_z^2}$$

$$
\begin{aligned}
&F_1P(x,z,\omega)\\
&+F_2(P(x+h,z,\omega)-2P(x,z,\omega)+P(x-h,z,\omega))\\
&+F_3(P(x,z+h,\omega)-2P(x,z,\omega)+P(x,z-h,\omega))\\
&+F_4(P(x+2h,z,\omega)-4P(x+h,z,\omega)+6P(x,z,\omega)-\\
&4P(x,z,\omega)-4P(x-h,z,\omega)+P(x-2h,z,\omega))/(h^4)\\
&+F_5(4P(x,z,\omega)-2(P(x-h,z,\omega)+P(x,z-h,\omega)\\
&+P(x+h,z,\omega)+P(x,z+h,\omega))+P(x-h,z-h,\omega)\\
&+P(x+h,z-h,\omega)+P(x+h,z+h,\omega)+P(x-h,z+h,\omega))/(h^4)=0
\end{aligned}
\tag{11.7}
$$

$$F_1=\frac{\omega^4}{v_{pl}^2}\langle\frac{1}{\rho v_p^2}\rangle$$

$$F_2=\frac{\omega^2}{v_{pl}^2}\langle\frac{1}{\rho}\rangle+\omega^2\langle\frac{1}{\rho v_p^2}\rangle-\frac{\omega^2\phi}{v_p^2\rho}$$

$$F_3=\frac{\omega^2}{v_p^2\langle\rho\rangle g_z^2}$$

$$F_4=(\langle\frac{1}{\rho}\rangle-\frac{\phi}{\rho})\frac{1}{g_x^4}$$

$$F_5=\frac{1}{\langle\rho\rangle g_x^2 g_z^2}$$

where $S(x,z,\omega)$ is the source signal in the frequency domain, and the source can be only placed in the VTI layer.

After the arrangement of (11.7), the coefficient of P for the first equation in (11.7) can be given

$$
\begin{aligned}
&P_{i,j}:-\frac{E_{1,i,j}}{h^2}-\frac{2E_{2,i,j}}{h^2}+\frac{4E_{3,i,j}}{h^4}+\omega^2\\
&P_{i,j+1}:\frac{E_{1,i,j}}{h^2}-\frac{E_{3,i,j}}{h^4}\\
&P_{i,j-1}:\frac{E_{1,i,j}}{h^2}-\frac{2E_{3,i,j}}{h^4}\\
&P_{i+1,j}:\frac{E_{2,i,j}}{h^2}-\frac{2E_{3,i,j}}{h^4}\\
&P_{i-1,j}:\frac{E_{2,i,j}}{h^2}-\frac{2E_{3,i,j}}{h^4}\\
&P_{i+1,j+1}:\frac{E_{3,i,j}}{h^4}\\
&P_{i-1,j+1}:\frac{E_{3,i,j}}{h^4}\\
&P_{i-1,j-1}:\frac{E_{3,i,j}}{h^4}
\end{aligned}
\tag{11.8}
$$

the coefficient of P for the second equation in (11.7) is given

$$\begin{gathered}
P_{i,j}: F_{1,i,j} - \frac{2F_{2,i,j}}{h^2} - \frac{2F_{3,i,j}}{h^2} + \frac{6F_{4,i,j}}{h^4} + \frac{4F_{5,i,j}}{h^4} \\
P_{i,j+1}: \frac{F_{2,i,j}}{h^2} - \frac{4F_{4,i,j}}{h^2} - \frac{2F_{5,i,j}}{h^4} \\
P_{i,j+2}: \frac{F_{4,i,j}}{h^4} \\
P_{i+1,j+1}: \frac{F_{5,i,j}}{h^4} \\
P_{i+1,j}: \frac{F_{3,i,j}}{h^2} - \frac{2F_{5,i,j}}{h^4} \\
P_{i,j-1}: \frac{F_{2,i,j}}{h^2} - \frac{4F_{4,i,j}}{h^4} - \frac{2F_{5,i,j}}{h^4} \\
P_{i,j-2}: \frac{F_{4,i,j}}{h^4} \\
P_{i-1,j}: \frac{F_{3,i,j}}{h^2} - \frac{2F_{5,i,j}}{h^4} \\
P_{i-1,j-1}: \frac{F_{5,i,j}}{h^4} \\
P_{i-1,j+1}: \frac{F_{5,i,j}}{h^4} \\
P_{i+1,j-1}: \frac{F_{5,i,j}}{h^4}
\end{gathered} \tag{11.9}$$

where the sum of them with the corresponding P is the left part of (11.7).

11.3.3. Absorbing boundary conditionPML

It has been pointed out that PML is not a boundary condition, but a method to attenuate the energy when it approaches the boundary. So, it is still essential to define the boundary condition to have full ranked matrices in the finite-difference method. Proposed by (Engquist & Majda, 2010), absorbing boundary condition (ABC) is adopted here, given by

$$\frac{\partial P}{\partial n} - \frac{i\omega P}{v} = 0 \tag{11.10}$$

where v is the velocity of the wave that you want to absorb at the boundary, and n is the direction perpendicular to the boundary line. Normally, we select the fastest wave velocity as v.

Let us assume a model with m grids on x-direction and n grids on z-direction. For instance, the top boundary ($i=1,\ j=2:m-1$) ABC can be formed as

$$\frac{P_{i+1,j}-P_{i,j}}{h}-\frac{i\omega P_{i,j}}{v}=0 \tag{11.11}$$

As for the top left corner ($i=1,\ j=1$), n is 45° away from x and z, (11.10) becomes

$$\sqrt{2}\frac{\partial P}{\partial x}+\sqrt{2}\frac{\partial P}{\partial z}-\frac{2i\omega P}{v}=0 \tag{11.12}$$

And the ABC of the other boundaries can be easily formed based on the above procedure.

Then we apply discretization to (11.12) to form

$$\sqrt{2}\frac{P_{i,j+1}-P_{i,j}}{h}+\sqrt{2}\frac{P_{i+1,j}-P_{i,j}}{h}-\frac{2i\omega P_{i,j}}{v}=0 \tag{11.13}$$

11.3.4. Source

The minimum-phase Ricker wavelet function used in this study is given by

$$s(x_s,z_s,t)=(1-(t-\frac{1}{f_s})^2(f_s\pi)^2)\exp(-(t-\frac{1}{f_s})^2(f_s\pi)^2) \tag{11.14}$$

where s is the source signal in the time domain; x_s and z_s are the coordinate of the source; f_s is the dominant frequency of the source.

A source wavelet with a dominant frequency of 20 Hz is shown in Figure 11-3.

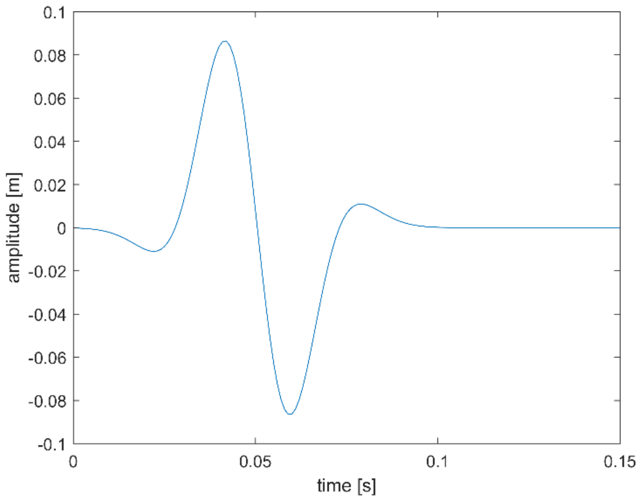

Figure 11-3. Source signals with a dominant frequency of 20 Hz.

As we are going to utilize the finite-difference method in the frequency domain, the source signal is supposed to be converted into the frequency domain using the Fourier transform. In fact, there is a fast Fourier transform function in Matlab. By simply calling it, the source signal in the frequency domain of Figure 11-3 can be obtained in Figure 11-4.

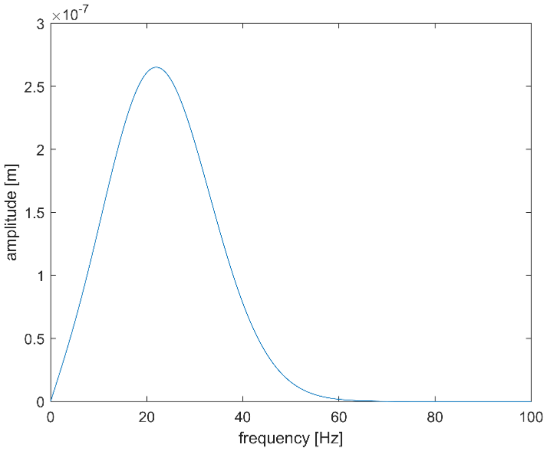

Figure 11-4. Absolute value of 20 Hz dominant source in the frequency domain.

Now the source signal can be inserted to the wave equation solver directly. The wave equation is solved at each frequency sample and then the wavefield $P(x,z,\omega)$ is obtained. Then with the inverse Fourier transform, the understandable wavefield $P(x,z,t)$ is constructed.

Now for each grid, at each one frequency, there is an equation for P to be solved.

Write those equations in a matrix form to formulate

$$\mathbf{GP}=\mathbf{S} \tag{11.15}$$

where $\mathbf{G}$ is the matrix of the coefficients of the equations; $\mathbf{P}$ and $\mathbf{S}$ are vectors consisting of the pressure field and the source signal.

11.4.Christoffel wave equation of BISQ wave equation

$$\begin{aligned}
J_1 &= C_{33}C_{44}s_1\theta_3 cos^6\theta + C_{11}C_{44}s_3\theta_1 sin^6\theta \\
&-C_{13}^2 s_1\theta_3 cos^4 sin^2\theta - C_{13}^2 s_3\theta_1 cos^2\theta sin^4\theta \\
&+C_{11}C_{33}s_1\theta_3 cos^4\theta sin^2\theta + C_{11}C_{33}s_3\theta_1 cos^2\theta sin^4\theta \\
&+C_{11}C_{44}s_1\theta_3 \cos^2\theta sin^4\theta - 2C_{13}C_{44}s_1\theta_3 cos^4\theta sin^2\theta \\
&-2C_{13}C_{44}s_3\theta_1 cos^2\theta sin^4\theta + C_{33}C_{44}s_3\theta_1 cos^4\theta sin^2\theta \\
J_2 &= C_{44}\hat{\alpha}_3^{\,2} s_1 cos^4\theta + C_{44}\hat{\alpha}_1^{\,2} s_3 sin^4\theta \\
&+C_{33}C_{44}\beta cos^4\theta + C_{11}C_{44}\beta sin^4\theta \\
&-C_{13}^2\beta cos^2\theta sin^2\theta + C_{11}\hat{\alpha}_3^{\,2} s_1 cos^2\theta sin^2\theta \\
&+C_{33}\hat{\alpha}_1^{\,2} s_3 cos^2\theta sin^2\theta + C_{13}C_{33}\beta cos^2\theta sin^2\theta \\
&-2C_{13}C_{44}\beta cos^2\theta sin^2\theta - C_{11}\hat{\rho}_3\omega^2 s_3\theta_1 sin^4\theta \\
&-C_{44}\hat{\rho}_1\omega^2 s_3\theta_1 sin^4\theta - C_{13}\hat{\alpha}_1\hat{\alpha}_3 s_1 cos^2\theta sin^2\theta \\
&-C_{13}\hat{\alpha}_1\hat{\alpha}_3 s_3 cos^2\theta sin^2\theta - C_{44}\hat{\alpha}_1\hat{\alpha}_3 s_1 cos^2\theta sin^2\theta \\
&-C_{44}\hat{\alpha}_1\alpha_3 s_3 cos^2\theta sin^2\theta - C_{33}\hat{\rho}_1\omega^2 s_1\theta_3 cos^4\theta \\
&-C_{44}\hat{\rho}_3\omega^2 s_1\theta_3 cos^4\theta - C_{11}\hat{\rho}_3\omega^2 s_1\theta_3 cos^2\theta sin^2\theta \\
&-C_{33}\hat{\rho}_1\omega^2 s_3\theta_1 cos^2\theta sin^2\theta - C_{44}\hat{\rho}_1\omega^2 s_1\theta_3 cos^2\theta sin^2\theta \\
&-C_{44}\hat{\rho}_3\omega^2 s_3\theta_1 cos^2\theta sin^2\theta \\
J_3 &= \hat{\rho}_1\hat{\rho}_3\omega^2 s_1\theta_3 cos^2\theta - C_{33}\hat{\rho}_1\beta\omega^2 \cos^2\theta \\
&-C_{44}\hat{\rho}_3\beta\omega^2 cos^2\theta - C_{11}\hat{\rho}_3\beta\omega^2 sin^2\theta \\
&-C_{44}\hat{\rho}_1\beta\omega^2 sin^2\theta - \hat{\alpha}_3^{\,2}\hat{\rho}_1\omega^2 s_1 cos^2\theta \\
&-\hat{\alpha}_1^{\,2}\hat{\rho}_3\omega^2 s_3 sin^2\theta + \hat{\rho}_1\hat{\rho}_3\omega^4 s_3\theta_1 sin^2\theta \\
J_4 &= \hat{\rho}_1\hat{\rho}_3\beta\omega^4
\end{aligned} \tag{11.16}$$

11.5.PML transform and discretization of BISQ wave equation

Similar to Section 11.3, the PML transform to BISQ wave equation (8.1) is given by

$$
\begin{aligned}
&\frac{C_{11}}{g_x}\frac{\partial}{\partial x}(\frac{1}{g_x}\frac{\partial u_x}{\partial x})+\frac{C_{44}}{g_z}\frac{\partial}{\partial z}(\frac{1}{g_z}\frac{\partial u_x}{\partial z})\\
&+\omega^2\widehat{\rho}_1 u_x+\frac{C_{13}+C_{44}}{g_x}\frac{\partial}{\partial x}(\frac{1}{g_z}\frac{\partial u_z}{\partial z})-\frac{\widehat{\alpha}_1}{g_x}\frac{\partial p}{\partial x}=S_x\\
&\frac{C_{13}+C_{44}}{g_x}\frac{\partial}{\partial x}(\frac{1}{g_z}\frac{\partial u_x}{\partial z})+\frac{C_{44}}{g_x}\frac{\partial}{\partial x}(\frac{1}{g_x}\frac{\partial u_z}{\partial x})\\
&+\frac{C_{33}}{g_z}\frac{\partial}{\partial z}(\frac{1}{g_z}\frac{\partial u_z}{\partial z})+\omega^2\widehat{\rho}_3 u_{xz}-\frac{\widehat{\alpha}_3}{g_z}\frac{\partial p}{\partial x}=S_z\\
&-\frac{s_3\widehat{\alpha}_1}{g_x}\frac{\partial u_x}{\partial x}-\frac{s_1\widehat{\alpha}_3}{g_z}\frac{\partial u_z}{\partial z}+\frac{s_3\theta_1}{g_x}\frac{\partial}{\partial x}(\frac{1}{g_x}\frac{\partial p}{\partial x})\\
&+\frac{s_1\theta_3}{g_z}\frac{\partial}{\partial z}(\frac{1}{g_z}\frac{\partial p}{\partial z})-\beta p=0
\end{aligned}
\tag{11.17}
$$

Following the similar procedure of Section 11.3.2, the discretization of (11.17) produces the coefficient of the field at each grid (under weak variation approximation). And the coefficient for the 3 equations in (11.17) is given,

the first equation:

$$
\begin{aligned}
&u_{x,i,j}:\omega^2\hat{\rho}_{1,i,j}-\frac{2C_{11,i,j}}{g^2_{x,i,j}h^2}-\frac{2C_{44,i,j}}{g^2_{z,i,j}h^2}\\
&u_{x,i,j+1}:-\frac{C_{11,i,j}}{2g^3_{x,i,j}h}(\frac{\partial g_x}{\partial x})_{i,j}+\frac{C_{11,i,j}}{g^2_{x,i,j}h^2}\\
&u_{x,i,j-1}:\frac{C_{11,i,j}}{2g^3_{x,i,j}h}(\frac{\partial g_x}{\partial x})_{i,j}+\frac{C_{11,i,j}}{g^2_{x,i,j}h^2}\\
&u_{x,i+1,j}:-\frac{C_{44,i,j}}{2g^3_{z,i,j}h}(\frac{\partial g_z}{\partial z})_{i,j}+\frac{C_{44,i,j}}{g^2_{z,i,j}h^2}\\
&u_{x,i-1,j}:\frac{C_{44,i,j}}{2g^3_{z,i,j}h}(\frac{\partial g_z}{\partial z})_{i,j}+\frac{C_{44,i,j}}{g^2_{z,i,j}h^2}\\
&u_{z,i+1,j+1}:\frac{C_{13,i,j}+C_{44,i,j}}{4g_{x,i,j}g_{z,i,j}h^2}\qquad u_{z,i-1,j+1}:-\frac{C_{13,i,j}+C_{44,i,j}}{4g_{x,i,j}g_{z,i,j}h^2}\\
&u_{z,i+1,j-1}:-\frac{C_{13,i,j}+C_{44,i,j}}{4g_{x,i,j}g_{z,i,j}h^2}\qquad u_{z,i-1,j-1}:\frac{C_{13,i,j}+C_{44,i,j}}{4g_{x,i,j}g_{z,i,j}h^2}\\
&p_{i,j+1}:-\frac{\hat{\alpha}_{1,i,j}}{2g_{x,i,j}h}\qquad p_{i,j-1}:\frac{\hat{\alpha}_{1,i,j}}{2g_{x,i,j}h}
\end{aligned}
\tag{11.18}
$$

the second equation:

$$\begin{gathered}
u_{x,i+1,j+1} : \frac{C_{13,i,j} + C_{44,i,j}}{4 g_{x,i,j} g_{z,i,j} h^2} \\
u_{x,i-1,j+1} : -\frac{C_{13,i,j} + C_{44,i,j}}{4 g_{x,i,j} g_{z,i,j} h^2} \\
u_{x,i+1,j-1} : -\frac{C_{13,i,j} + C_{44,i,j}}{4 g_{x,i,j} g_{z,i,j} h^2} \\
u_{x,i-1,j-1} : \frac{C_{13,i,j} + C_{44,i,j}}{4 g_{x,i,j} g_{z,i,j} h^2} \\
u_{z,i,j} : \omega^2 \hat{\rho}_{3,i,j} - \frac{2C_{44,i,j}}{g^2_{x,i,j} h^2} - \frac{2C_{33,i,j}}{g^2_{z,i,j} h^2} \\
u_{xz,i,j+1} : -\frac{C_{44}}{2 g^3_{x,i,j} h} \left(\frac{\partial g_x}{\partial x}\right)_{i,j} + \frac{C_{44,i,j}}{g^2_{x,i,j} h^2} \\
u_{x,i,j-1} : \frac{C_{44,i,j}}{2 g^3_{x,i,j} h} \left(\frac{\partial g_x}{\partial x}\right)_{i,j} + \frac{C_{44,i,j}}{g^2_{x,i,j} h^2} \\
u_{z,i+1,j} : -\frac{C_{33,i,j}}{2 g^3_{z,i,j} h} \left(\frac{\partial g_z}{\partial z}\right)_{i,j} + \frac{C_{33,i,j}}{g^2_{z,i,j} h^2} \\
u_{x,i-1,j} : \frac{C_{33,i,j}}{2 g^3_{z,i,j} h} \left(\frac{\partial g_z}{\partial z}\right)_{i,j} + \frac{C_{33,i,j}}{g^2_{z,i,j} h^2} \\
p_{i+1,j} : -\frac{\widehat{\alpha}_{3,i,j}}{2 g_{z,i,j} h} \\
p_{i-1,j} : \frac{\widehat{\alpha}_{3,i,j}}{2 g_{z,i,j} h}
\end{gathered} \tag{11.19}$$

the third equation:

$$u_{x,i,j+1}:-\frac{s_{3,i,j}\widehat{\alpha}_{1,i,j}}{2g_{x,i,j}h}$$

$$u_{x,i,j-1}:\frac{s_{3,i,j}\widehat{\alpha}_{1,i,j}}{2g_{x,i,j}h}$$

$$u_{z,i+1,j}:-\frac{s_{1,i,j}\widehat{\alpha}_{3,i,j}}{2g_{z,i,j}h}$$

$$u_{z,i-1,j}:\frac{s_{1,i,j}\widehat{\alpha}_{3,i,j}}{2g_{z,i,j}h}$$

$$p_{i,j}:-\beta_{i,j}-\frac{2s_{3,i,j}\theta_{1,i,j}}{g_{x,i,j}^{2}h^{2}}-\frac{2s_{1,i,j}\theta_{3,i,j}}{g_{z,i,j}^{2}h^{2}} \tag{11.20}$$

$$p_{i,j+1}:-\frac{s_{3,i,j}\theta_{1,i,j}}{2g_{x,i,j}^{3}h}\left(\frac{\partial g_{x}}{\partial x}\right)_{i,j}+\frac{s_{3,i,j}\theta_{1,i,j}}{g_{x,i,j}^{2}h^{2}}$$

$$p_{i,j-1}:\frac{s_{3,i,j}\theta_{1,i,j}}{2g_{x,i,j}^{3}h}\left(\frac{\partial g_{x}}{\partial x}\right)_{i,j}+\frac{s_{3,i,j}\theta_{1,i,j}}{g_{x,i,j}^{2}h^{2}}$$

$$p_{i+1,j}:-\frac{s_{1,i,j}\theta_{3,i,j}}{2g_{z,i,j}^{3}h}\left(\frac{\partial g_{z}}{\partial z}\right)_{i,j}+\frac{s_{1,i,j}\theta_{3,i,j}}{g_{z,i,j}^{2}h^{2}}$$

$$p_{i-1,j}:\frac{s_{1,i,j}\theta_{3,i,j}}{2g_{z,i,j}^{3}h}\left(\frac{\partial g_{z}}{\partial z}\right)_{i,j}+\frac{s_{1,i,j}\theta_{3,i,j}}{g_{z,i,j}^{2}h^{2}}$$

the sum of the coefficients times the corresponding field (u_x, u_z or p) forms the left part of (11.17). The boundary condition is still ABC, as introduced in Section 11.3.3.

11.6.Matlab code

The Matlab code used in this article is available at my personal Github webpage: https://github.com/deconvolution. The acoustic wavefield simulation for VTI media and horizontally cracked layers is filed under the repository ‘Fractured-media’ and the BISQ poroelastic wavefield simulation can be found under ‘BISQ’. In addition, the derivation of the propagator matrix and slowness for alternating solid and fluid layers is given under ‘propagator-matrix’.